STUDIES ON BUOYANCY-INDUCED OPEN FLOWS: PLANE THERMAL PLUME

A Thesis

Submitted for the Degree of

MASTER OF SCIENCE (ENGINEERING)

by

RAJARAM LAKKARAJU

ENGINEERING MECHANICS UNIT
JAWAHARLAL NEHRU CENTRE FOR ADVANCED SCIENTIFIC RESEARCH
(A Deemed University)
Bangalore – 560 064

SEPTEMBER 2007

To my parents and the God

DECLARATION

I declare that the matter embodied in the thesis entitled "**Studies on Buoyancy-Induced Open Flows: Plane Thermal Plume**" is the result of investigations carried out by me at the Engineering Mechanics Unit, Jawaharlal Nehru Centre for Advanced Scientific Research, Bangalore, India under the supervision of Dr. Meheboob Alam and that it has not been submitted elsewhere for the award of any degree or diploma.

In keeping with the general practice in reporting scientific observations, due acknowledgment has been made whenever the work described is based on the findings of other investigators.

Rajaram Lakkaraju

CERTIFICATE

I certify that the matter embodied in this thesis entitled "**Studies on Buoyancy-Induced Open Flows: Plane Thermal Plume**" has been carried out by Mr. Rajaram Lakkaraju at the Engineering Mechanics Unit, Jawaharlal Nehru Centre for Advanced Scientific Research, Bangalore, India under my supervision and that it has not been submitted elsewhere for the award of any degree or diploma.

Dr. Meheboob Alam
(Research Supervisor)

Abstract

In the present thesis, the natural convection flow over a line heat source is studied for the mean flow and the linear stability characteristics at different Prandtl numbers. This flow is purely driven by buoyancy and called a thermal plume. The temperature of the fluid is more at the line heat source than the surrounding fluid - the resulting density difference generates buoyancy force which drives the plume through the ambient fluid. The stability and the transition behaviour of a thermal plume are not well understood at high Prandtl numbers which is the focus of the present thesis. Understanding natural convection is very important for environmental problems, like atmospheric and oceanic circulations, as well as for a vast number of engineering and industrial applications.

The mean flow of a plane thermal plume is analysed for the leading-order and the higher-order terms by using boundary-layer approximations. The leading-order mean flow equations are solved by using the Runge-Kutta method with the Newton-Raphson correction. The computed results have been validated by comparing them with known analytical results. With increasing Prandtl number (P), the thermal boundary layer becomes thinner and the velocity levels are decreased in the plume. Since the viscous diffusion is more for high Prandtl number fluids, the velocity profile becomes flatter with increasing P. For a given Prandtl number, the maximum temperature in the plume decreases as minus three-fifth power of the height. The first-order correction for the mean flow equations are also solved by the Runge-Kutta method with the Newton-Raphson correction. The mean flow results after adding higher-order correction terms suggest that the center-line temperature decreases and the flow velocity increases near edge of the boundary layer. The magnitudes of first-order correction terms for both velocity and temperature become progressively smaller with increasing Prandtl number.

Small amplitude disturbances are added to the mean flow, and their amplification rates are computed by using parallel flow approximations. Both the temporal and spatial stability analyses are carried out for Prandtl numbers ranging 0.7-1000. The linear stability equations are solved by using the finite difference and the spectral methods with different grid sizes. Both the QZ- algorithm and the Arnoldi algorithm are used to compute eigenvalues of the linear stability operator. It is shown that the Arnoldi algorithm takes less time compared to the standard QZ algorithm. At high Prandtl numbers, the neutral curve shows an additional unstable loop, the origin of which is tied to the interaction between hydrodynamic and thermal disturbances. The critical modified Grashof number is found to vary inversely with Prandtl number (i.e. $G^* \sim \frac{1}{P}$). For spatial stability analysis, the companion matrix method is used to compute non-linear eigenvalues. Non-parallel correction terms are computed by using the adjoint functions and the computational results are shown for a limited range of Prandtl numbers.

The present work uncovered a new instability mode at high Prandtl numbers which remains relatively unaffected with the inclusion of non-parallel effects. The origin of this new instability mode suggests that the hydrodynamic and thermal disturbances cannot be decoupled for a high Prandtl number thermal plume.

Publications

Lakkaraju, Rajaram and Alam, Meheboob,
"Effects of Prandtl number and a new instability mode in a plane thermal plume",
Journal of Fluid Mechanics, (In press 2007).

Acknowledgments

I am indebted to Dr. Meheboob Alam for his guidance and patience at every stage of this work, and indeed for teaching me what research is all about. I am fortunate to have him as my advisor.

I am thankfull to all the faculty of Engineering Mechanics Unit (EMU) in JNCASR.

I am extremely gratefull to my good friend Pinaki in EMU for his help in teaching me Fluid Mechanics and LATEX.

I am gratefull to Kaushik, Vijaykumar, Vinod in EMU, Pavan kumar in CPMU and Sairam in TSU for their constant help and suggestions during my research work.

My thanks to Ashish Malik, Bishakh, Priyanka and Kirti Sahu in EMU for allowing me to use their computers for through out the work.

I thank Prof. Jayawant Arakeri (IISc), Prof. J. Dey (IISc) and Dr. Umesh Waghmare (JNCASR) for teaching me courses which are the basis for my research work carried out in JNCASR.

I am thankfull to Defence Research Development Organisation (DRDO) for providing me financial assistance in the last six months.

Contents

Nomenclature

Roman Letters

c	:	Wavespeed of disturbance
c_p	:	Specific heat
f, h	:	Normalized streamfunction and temperature (similarity solution)
g	:	Accelaration due to gravity
k	:	Thermal conductivity
u, v, w	:	Velocity components
x, y, z	:	Co-ordinate directions
Gr	:	Local Grashof number
G^*	:	Modified-Grashof number
P	:	Prandtl number

Greek Letters

α	:	Streamwise wave number
β	:	Volumetric coefficient of thermal expansion
γ	:	Spanwise wavenumber
δ	:	Boundary layer thickness
ω	:	Wave frequency
κ	:	Thermal diffusivity
ν	:	Kinematic viscosity
ρ	:	Density of the fluid
θ	:	Temperature difference
ϕ, s	:	Generalized stream function and temperature of disturbance
$\mathbf{\Phi^*_{VD}}$	:	Viscous dissipation

List of Figures

List of Tables

CHAPTER 1

INTRODUCTION

1.1 Natural Convection

Themal convection is a mechanism of transporting heat due to the bulk motion of the fluid. There are two types of convection:
1) *Forced convection*: The bulk fluid motion is generated by some external force via pumps, fans, compressors etc.
2) *Natural convection*: The bulk fluid motion is generated not by any external source but only by density differences in the fluid occuring due to the temperature or concentration gradients or both. The presence of gravity is essential for natural convection.

Natural convection attracted a great deal of attention of researchers because of its vast presence in nature like the rising plume of hot air from fire, oceanic currents, sea-wind formation, fog formation, the Earth's mantle (magma chambers) and also in engineering applications like the cooling of molten metals (e.g. in steel industry), the cooling of electronic components, solar ponds, etc.

Two non-dimensional numbers involved in the natural convection phenomena are the Grashof number (Gr) which is the ratio of buoyancy force and viscous force, and the Prandtl number (P) which is the ratio of kinematic viscosity and thermal diffusivity. In terms of P, there are two limiting cases: zero Prandtl number (molten metals, $P \sim 10^{-8}$) and infinite Prandtl number (mantle plumes, $P \sim 10^{21}$). Geological flows involve fluids with very large Prandtl numbers and are studied in the limit of infinite Prandtl number (Kaminski & Jaupert 2003). It must, however, be noted that the geological fluids are non-Newtonian which is an added complexity of geological flows.

Natural convection in the atmospheric boundary layers corresponds to low

Prandtl number (e.g. $P = 0.7$ for air). Many researchers have carefully studied the mean flow and the stability characteristics of air for various flow configurations. These studies involve forced, natural and mixed convection on flat plates, cylinders, etc. Almost all the studies matched their results with each other in forced convection but not in natural convection. Even though the research on natural convection started in early 1950 (Batchelor 1954), the results on stability characteristics at different Prandtl numbers are controversial in terms of the minimum critical Grashof number and the lower branch for the neutral curve (Gebhart *et al.* 1988).

1.2 Plumes

When a horizontal line heat source is placed in a quiescent fluid, the fluid near the heat-source ascends due to the resulting density difference. This is called a thermal plume or natural convection plume, see figure 1.1. This thermal plume starts as a laminar flow at the source and because of the presence of disturbances, the flow goes through a series of transitions and eventually becomes turbulent (Gebhart & Mahajan 1982, Grossmann & Lohse 2000, Puthenveettil & Arakeri 2005, Niemela & Sreenivasan 2006). The role of linear stability is to predict whether the flow is stable/unstable to infinitesimal disturbances. The stability analysis is commonly done by perturbing a given steady state solution of the equations of motion with small periodic velocity and temperature disturbances. If the disturbance grows or remains at some magnitude different from zero, the flow is said to be, respectively, unstable or neutrally stable. Squire (1933) showed that, in a boundary layer flow, the two dimensional disturbances amplify at a lower Reynlods number than the three dimensional ones, and are, therefore, the least stable modes. Knowles & Gebhart (1971) extended Squire's Theorem to natural convection flow for which the velocity and temperature disturbances are coupled.

The stability of a thermal plume over a line heat source is investigated at different Prandtl numbers in the present work. Related previous works involve understanding the mean flow and the stability at low Prandtl numbers for various flow configurations. Most of the earlier researchers published their results for mean flow upto a Prandtl number of 100 (Fujii 1963; Brand & Lahey 1967; Gebhart *et*

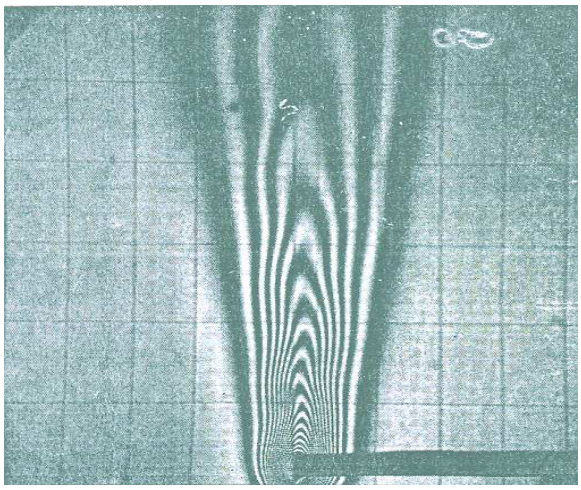

Figure 1.1: This picture shows stability of a plane thermal plume which is disturbed by a sinusoidal excitation at a frequency 7Hz (Pera & Gebhart 1971).

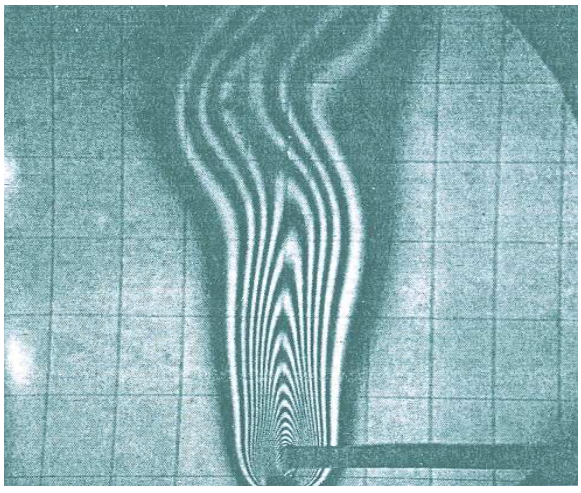

Figure 1.2: This picture shows instability of a plane thermal plume which is disturbed by a sinusoidal excitation at a frequency 2.4Hz (Pera & Gebhart 1971).

al. 1970; Fujii *et al.* 1973), and an asymptotic analysis for large Prandtl numbers was carried out by Spalding & Cruddace (1961). Similar analyses for natural convection phenomenon on plates (Gill & Davey 1969, Hieber 1974; Afzal 1980) and on thin wires with higher-order effects (Riley 1974) are available. The stability of a thermal plume above a line heat source and the natural convection on plates have attracted the attention of many researchers (Szewczyk 1962; Natchtsheim 1963; Knowles & Gebhart 1968; Pera & Gebhart 1971; Hieber & Nash 1975; Wakitani 1985). The effect of adding viscous dissipation terms in the energy equation has also been studied (Gebhart 1962; Mollendorf & Gebhart 1969). Figures 1.1 and 1.2 show the experimental pictures of a plane thermal plume taken from Pera & Gebhart (1971). Here a line plume is disturbed by a mechanical disturbance with different frequencies. For a range of frequencies the flow is stable and have a smooth laminar flow (i.e. the disturbances decay out); for other range of frequencies, the disturbances will grow and transition starts far downstream. We can clearly see that the flow is stable at a frequency 7Hz and is unstable at 2.4Hz with a sinuous mode of instability.

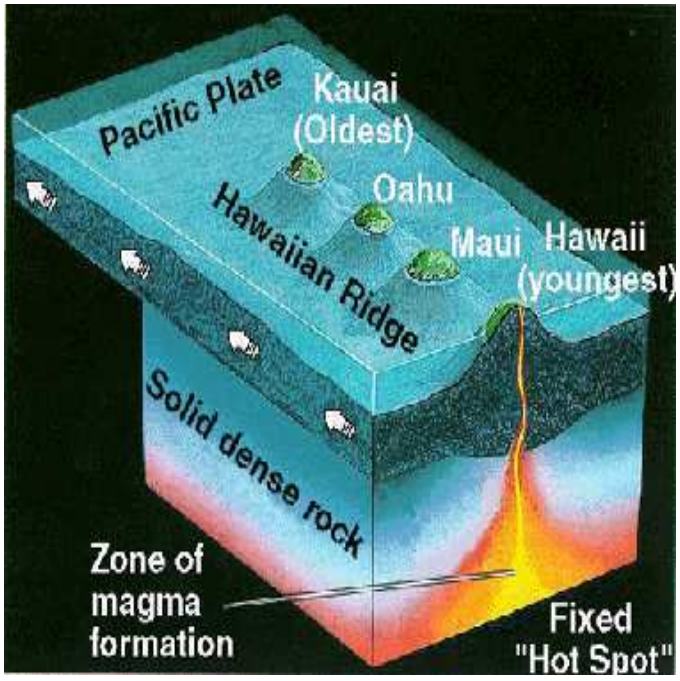

Figure 1.3: Schematic of mantle plumes when volcanic eruption is taking place (taken from http://volcano.und.edu)

Figure 1.3 shows a schematic view of mantle plumes. At earth's core (see figure 1.4), the molten metal starts rising against the direction of gravity. This is a purely buoyancy driven flow. This picture depicts the plume configuration. The theory of instability is useful to predict whether the laminar magma flow is going through transition stage or not. As mentioned before, such geological fluids are non-Newtonian which we would not discuss in this thesis.

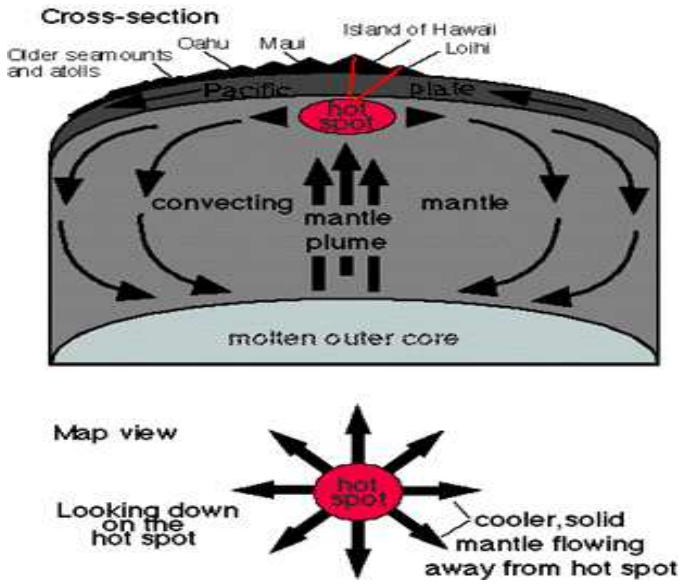

Figure 1.4: Schematic of thermal convection phenomenon in mantle plumes (taken from urlhttp://volcano.und.edu)

An analogy between a high Schmidt number (the ratio between kinematic viscosity and diffusivity) plume and a bubble plume has recently been postulated for buoyancy driven bubble plumes (Alam & Arakeri 1993). Therefore, understanding the related thermal convection phenomena at high Prandtl number is important. Pictures of transitional bubble plumes are shown in figure 1.5. Here, the plane bubble plume was generated from a line source via electrolysis in a large water-tank. It is observed that the bubble plume rises straight from the source and is subjected to a sinuous-mode instability at some downstream location, before breaking into alternating vortices. The point to note is that in the laminar region the bubble plume hardly diffuses across the lateral direction which suggests that the concentration boundary-layer thickness is much smaller that the velocity boundary-layer

thickness and the related Schmidt number is very large. It is anticipated that understanding the dynamics of large Prandtl number thermal plumes will shed some light on the transition characteristics of a bubble plume.

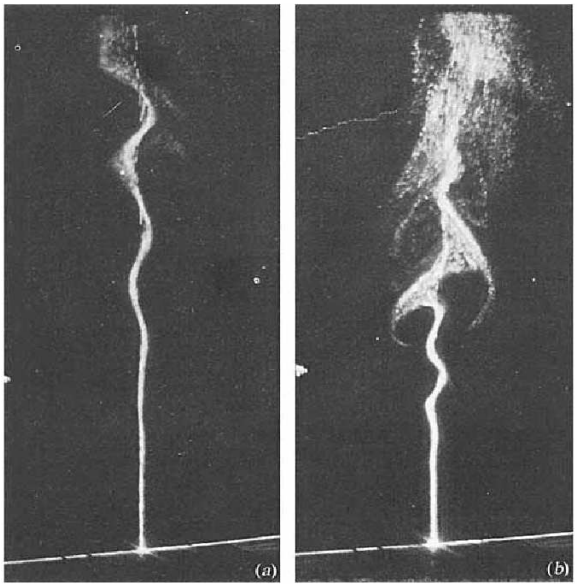

Figure 1.5: Transition in plane bubble plumes (Alam & Arakeri 1993)

There is very little work involved on the high Prandtl number convective flows in terms of mean flow and also in terms of their stability characteristics. The goal of the present work is to understand the dynamics of high Prandtl number thermal plumes.

1.3 Present Work

In the present thesis, the mean flow of a thermal plume rising from a line heat source is analysed, and the corresponding linear stability analysis is also done for a range of Prandtl numbers ($P = 0.7$ to 1000). Both temporal and spatial stability analyses are carried out with parallel and non-parallel theory. Finite difference and

spectral collocation methods are used for solving the linear stability equations. At high Prandtl numbers ($P > 100$), the neutral stability curve shows an additional unstable loop. At any P, the thermal plume is unstable for very small Grashof numbers and the critical Grashof number varies with the Prandtl number as inverse square root. Adding the viscous dissipation terms in the energy equation has a stabilizing effect at moderate dissipation parameters. The solutions for the uncoupled momentum and energy stability equations are also computed at high Prandtl numbers, and a power-law relation between the critical Grashof number and the wave number has been obtained. The present results clearly suggest that the additional unstable loop (at high Prandtl number) originates due to the coupling of momentum and energy equations.

1.3.1 Organisation of Thesis

Chapter 2: Here we compute the mean flow of a thermal plume (by using similarity technique) with leading-order and first-order boundary-layer approximations. The Runge-Kutta method with Newton-Raphson correction is employed to carry out the integration of ordinary differential equations with appropriate boundary conditions.

Chapter 3: Here we formulate the linear stability equations and solve these equations under the parallel flow approximation for the temporal stability. Both the finite difference and spectral collocation methods are employed to discretize the stability equations. The stability characteristics and the energy distribution plots are analysed.

Chapter 4: The spatial stability is carried out by using the companion matrix method and the stability characteristic curves for different Prandtl numbers are shown. These results are compared with those of temporal stability analysis. The non-parallel stability analysis is carried out, following the earlier work of Wakitani (1985). The effects of non-parallel disturbed flow are analysed for a few cases.

CHAPTER 2

PLANE THERMAL PLUME

2.1 Background

The classic problem of laminar, natural-convection flow above a horizontal line heat source has received considerable attention in the last few decades (Spalding & Cruddace 1961, Fujii 1963, Pera & Gebhart 1971, Wakitani 1985). Similarity solutions of the laminar boundary layer equations have been published by many researchers for different Prandtl numbers; experimental studies of laminar plane plumes, that include those of Brodowicz & Kierkus (1966) in air and of Gebhart *et al.* (1970) in silicone oil, are in good agreement with the laminar theory. Many observations of laminar plume flow have indicated that they sway in a plane perpendicular to the axis of the source. Pera & Gebhart (1971) have shown that the initial instability of plane plumes to two dimensional disturbances may be analyzed by the linear stability theory and developed the coupled Orr-Sommerfeld type equations using a parallel flow approximation. Weakly non-parallel corrections were subsequently considered by Halland & Sparrow (1973), Hieber & Nash (1975) and Wakitani (1985).

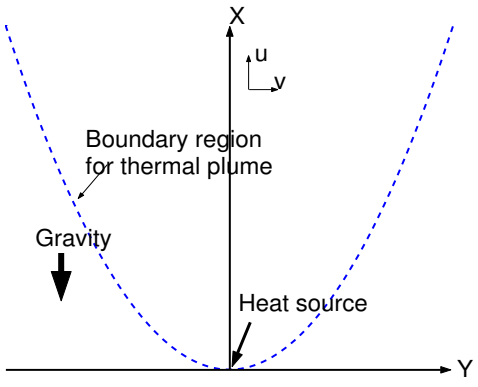

Figure 2.1: Schematic of a plane thermal plume

For the two dimensional convection above a line heat source, located horizontally in a large fluid space, the primary variables describing the flow and temperature are indicated in figure 2.1, where x and y are the vertical and horizontal coordinates, respectively, with the origin being located at the heat source; u and v are the velocity components in the x- and y-directions, respectively.

2.2 Governing equations for thermal plumes with Boussinesq approximation

We consider the convective flow generated above a line heat source in an otherwise stagnant fluid which is maintained at a constant temperature T_∞. A plume is generated from the heat source whose temperature T_s is larger than that of the ambient fluid, and hence the plume rises up against the gravity due to the resultant buoyant force. The two-dimensional governing equations with Boussinesq approximation[1] are

$$\frac{\partial u}{\partial x} + \frac{\partial v}{\partial y} = 0 \tag{2.1}$$

$$\frac{\partial u}{\partial \tilde{\tau}} + u\frac{\partial u}{\partial x} + v\frac{\partial u}{\partial y} = \nu\nabla^2 u - \frac{1}{\rho}\frac{\partial p}{\partial x} + g\beta(T - T_\infty) \tag{2.2}$$

$$\frac{\partial v}{\partial \tilde{\tau}} + u\frac{\partial v}{\partial x} + v\frac{\partial v}{\partial y} = \nu\nabla^2 v - \frac{1}{\rho}\frac{\partial p}{\partial y} \tag{2.3}$$

$$\frac{\partial T}{\partial \tilde{\tau}} + u\frac{\partial T}{\partial x} + v\frac{\partial T}{\partial y} = \kappa\nabla^2 T + \mathbf{\Phi_{VD}} \tag{2.4}$$

$$\mathbf{\Phi_{VD}} = \frac{2\nu}{3c_p}\left[2\left(\frac{\partial u}{\partial x}\right)^2 + 2\left(\frac{\partial v}{\partial y}\right)^2 - 2\frac{\partial u}{\partial x}\frac{\partial v}{\partial y} + \left(\frac{\partial u}{\partial y} + \frac{\partial v}{\partial x}\right)^2\right]. \tag{2.5}$$

Here $\mathbf{\Phi_{VD}}$ is the viscous dissipation term, p is the pressure difference (from the ambient pressure), T is the temperature, T_∞ is the ambient fluid temperature and g is the accelaration due to gravity. The thermophysical properties of the fluid are density ρ, thermal expansion coefficient β, kinematic viscosity ν, thermal conductivity k, specific heat c_p and thermal diffusivity $\kappa = \frac{k}{\rho c_p}$.

[1] Pressure effects on fluid density are neglected and temperature effects are taken to be linear over the range from T to T_∞. Then $g(\rho - \rho_\infty)$ is taken as $g\beta(T - T_\infty)$.

The boundary conditions are:

$$u = v = 0,\ T = T_s \ \text{ at } x = y = 0 \ \text{ and}$$
$$u = v = T = 0 \text{ at } x^2 + y^2 \to \infty. \tag{2.6}$$

2.2.1 Governing Equations in Non-Dimensional Form

The Navier-Stokes equations with Boussinesq approximation are non-dimensionalised using following scales:

$$x = x^* x_0,\ y = y^* x_0,\ \tilde{\tau} = \tilde{\tau}^*(x_0/U_0),\ u = U_0 u^*,\ v = U_0 v^*,$$
$$p - p_\infty = p^* \rho {U_0}^2,\ T - T_\infty = (T_0(x_0) - T_\infty)\theta^*.$$

Here the characteristic length (x_0) is a local distance measured from the heat source in the x-direction, $T_0(x_0) \equiv T(x_0, y = 0)$ and $U_0 = \sqrt{g\beta(T_0(x_0) - T_\infty)x_0}$ is the characteristic velocity. The governing equations in non-dimensional form are:

$$\frac{\partial u^*}{\partial x^*} + \frac{\partial v^*}{\partial y^*} = 0 \tag{2.7}$$
$$\frac{\partial u^*}{\partial \tilde{\tau}^*} + u^*\frac{\partial u^*}{\partial x^*} + v^*\frac{\partial u^*}{\partial y^*} = \frac{1}{\sqrt{Gr}}\nabla^2 u^* - \frac{\partial p^*}{\partial x^*} + \theta^* \tag{2.8}$$
$$\frac{\partial v^*}{\partial \tilde{\tau}^*} + u^*\frac{\partial v^*}{\partial x^*} + v^*\frac{\partial v^*}{\partial y^*} = \frac{1}{\sqrt{Gr}}\nabla^2 v^* - \frac{\partial p^*}{\partial y^*} \tag{2.9}$$
$$\frac{\partial \theta^*}{\partial \tilde{\tau}^*} + u^*\frac{\partial \theta^*}{\partial x^*} + v^*\frac{\partial \theta^*}{\partial y^*} = \frac{1}{P\sqrt{Gr}}\nabla^2 \theta^* + D_p P\sqrt{Gr}\,\mathbf{\Phi^*_{VD}} \tag{2.10}$$

$$\mathbf{\Phi^*_{VD}} = \frac{2}{3}\left[2\left(\frac{\partial u^*}{\partial x^*}\right)^2 + 2\left(\frac{\partial v^*}{\partial y^*}\right)^2 - 2\frac{\partial u^*}{\partial x^*}\frac{\partial v^*}{\partial y^*} + \left(\frac{\partial u^*}{\partial y^*} + \frac{\partial v^*}{\partial x^*}\right)^2\right]. \tag{2.11}$$

The boundary conditions in non-dimensional form are:

$$u^* = v^* = 0, \theta^* = 1 \quad \text{at} \quad x^* = y^* = 0 \quad \text{and}$$
$$u^* = v^* = \theta^* = 0 \quad \text{at} \quad {x^*}^2 + {y^*}^2 \to \infty \tag{2.12}$$

Here,
$Gr = Gr_{x_0} = \frac{g\beta(T_0(x_0) - T_\infty)x_0^3}{\nu^2}$ is the local Grashof number, $P = \frac{\nu}{\kappa}$ is the Prandtl

number, $D_p = \frac{g\beta x_0}{c_p}$ is the non-dimensional dissipation parameter.

2.3 Base State Equations

The base state is assumed to be time independent (steady) and it's governing equations, neglecting the viscous dissipation term in the energy equation, are:

$$\frac{\partial u^*}{\partial x^*} + \frac{\partial v^*}{\partial y^*} = 0 \tag{2.13}$$

$$u^*\frac{\partial u^*}{\partial x^*} + v^*\frac{\partial u^*}{\partial y^*} = \frac{1}{\sqrt{Gr}}\nabla^2 u^* - \frac{\partial p^*}{\partial x^*} + \theta^* \tag{2.14}$$

$$u^*\frac{\partial v^*}{\partial x^*} + v^*\frac{\partial v^*}{\partial y^*} = \frac{1}{\sqrt{Gr}}\nabla^2 v^* - \frac{\partial p^*}{\partial y^*} \tag{2.15}$$

$$u^*\frac{\partial \theta^*}{\partial x^*} + v^*\frac{\partial \theta^*}{\partial y^*} = \frac{1}{P\sqrt{Gr}}\nabla^2 \theta^*. \tag{2.16}$$

After dropping $*$ notation and writing these equations in terms of stream function (Ψ) and temperature (Θ), we obtain

$$\left(\Psi_y\frac{\partial}{\partial x} - \Psi_x\frac{\partial}{\partial y}\right)\nabla^2\Psi - Gr^{-1/2}\nabla^4\Psi - \frac{\partial \theta}{\partial y} = 0, \tag{2.17}$$

$$\left(\Psi_y\frac{\partial}{\partial x} - \Psi_x\frac{\partial}{\partial y}\right)\theta - Gr^{-1/2}P^{-1}\nabla^2\theta = 0. \tag{2.18}$$

Here $u = \Psi_y$, $v = -\Psi_x$ and the corresponding boundary conditions are:

$$u = v = 0, \Theta = 1 \quad \text{at} \quad x = y = 0 \implies \Psi = \Psi_y = 0, \theta = 1, \tag{2.19}$$

$$u \to 0, v \to 0, \theta \to 0 \quad \text{at} \quad x^2 + y^2 \to \infty \implies \Psi \to 0, \Psi_y \to 0, \theta \to 0. \tag{2.20}$$

2.4 Asymptotic Analysis

The asymptotic solution of the base state is studied for large values of Grashoff numbers (Gr) by the method of matched asymptotic expansions (Riley 1974, Afzal 1980, Kuiken 1971, Kurdyumov 2005). We seek two limits and two corresponding asymptotic expansions which describe the flow regime close to the center line (inner limit) and away (outer limit) from it. Here we follow the procedure given by Riley (1974) to formulate the leading-order and the related higher-order boundary-layer

equations.

The outer limit is defined as x, y are fixed with $Gr \to \infty$. The outer layer, which is essentially inviscid, can be studied in the form of expansions,

$$\Psi = \Psi_0(x,y) + \epsilon_1 \Psi_1(x,y) + O(\epsilon_2), \tag{2.21}$$

$$\theta = \Theta_0(x,y) + \epsilon_1 \Theta_1(x,y) + O(\epsilon_2). \tag{2.22}$$

The inner region close to the center line, where the diffusive effects are important, is characterized by buoyancy forces. An order of magnitude analysis [2] leads to the following inner variable, $Y = y\, Gr^{1/4}$, and the inner limit is defined as x, Y are fixed with $Gr \to \infty$. The expansions for the inner layer are,

$$\Psi = Gr^{-1/4} \left[\psi_0(x,Y) + \Delta_1 \psi_1(x,Y) + O(\Delta_2)\right], \tag{2.23}$$

$$\theta = \theta_0(x,Y) + \Delta_1 \theta_1(x,Y) + O(\Delta_2). \tag{2.24}$$

Matching of the outer and inner expansions in the overlap region leads to

$$\epsilon = \epsilon_1 = \Delta_1 = Gr^{-1/4}. \tag{2.25}$$

2.4.1 Leading-order Boundary-Layer Problem: Similarity Solution

The solutions to the leading terms in outer expansions (2.21-2.22) satisfying outer boundary conditions are $\Psi_0(x,y) = \Theta_0(x,y) = 0$. This suggests that there is no flow or temperature in the outer layer when Grashof number (Gr) is large. This trivial solution fails to explain the convection of heat released by the source. The non-uniformity near the heat source can be analysed by the inner expansion.

[2] From the x- momentum equation (2.14), we can estimate the boundary-layer thickness.

$$u\frac{\partial u}{\partial x} + v\frac{\partial u}{\partial y} = \frac{1}{\sqrt{Gr}}\nabla^2 u - \frac{\partial p}{\partial x} + \theta.$$

The inertia terms ($O(1)$) on the left side of the above equation should be balanced by the viscous and the buoyancy terms. This balance is not possible unless $\frac{\partial^2 u}{\partial y^2} \sim O(Gr^{1/2})$; the highest-order terms should be retained in the above equation when $Gr \to \infty$. $\Rightarrow \frac{1}{\sqrt{Gr}}\frac{\partial^2 u}{\partial y^2} = O(1)$. It means $y \sim \frac{1}{Gr^{1/4}}$, so that the new scaling $Y = yGr^{1/4}$ is appropriate to get the boundary-layer approximation.

Substituting inner expansions (2.23 and 2.24) in governing equations (2.17) and (2.18), we obtain:

$$\begin{aligned} &\epsilon^0\left(\psi_{0Y}\psi_{0xYY}-\psi_{0x}\psi_{0YYY}-\psi_{0YYYY}-\theta_{0Y}\right)+ \\ &\epsilon^1\left(\psi_{0Y}\psi_{1xYY}+\psi_{1Y}\psi_{0xYY}-\psi_{0x}\psi_{1YYY}-\psi_{1x}\psi_{0YYY}-\psi_{1YYYY}-\theta_{1Y}\right)+O\left(\epsilon^2\right) &= 0, \end{aligned} \tag{2.26}$$

$$\begin{aligned} &\epsilon^0\left(\psi_{0Y}\theta_{0x}-\psi_{0x}\psi_{0Y}-P^{-1}\theta_{0YY}\right)+ \\ &\epsilon^1\left(\psi_{1Y}\theta_{0x}+\psi_{0Y}\theta_{1x}-\psi_{0x}\theta_{1Y}-\psi_{1x}\theta_{0Y}-P^{-1}\theta_{1YY}\right)+O\left(\epsilon^2\right) &= 0. \end{aligned} \tag{2.27}$$

Considering $O(\epsilon^0)$ terms in (2.26) and (2.27), we obtain classical boundary-layer equations:

$$\psi_{0Y}\psi_{0xYY}-\psi_{0x}\psi_{0YYY}-\psi_{0YYYY}-\theta_{0Y} = 0, \tag{2.28}$$

$$\psi_{0Y}\theta_{0x}-\psi_{0x}\psi_{0Y}-P^{-1}\theta_{0YY} = 0. \tag{2.29}$$

After integrating the momentum equation with respect to Y and setting the resulting arbitary function of x equal to zero, we obtain

$$\psi_{0Y}\psi_{0xY}-\psi_{0x}\psi_{0YY}-\psi_{0YYY}-\theta_{0} = 0, \tag{2.30}$$

$$\psi_{0Y}\theta_{0x}-\psi_{0x}\psi_{0Y}-P^{-1}\theta_{0YY} = 0. \tag{2.31}$$

The boundary conditions are (Riley 1974)

$$\psi_0=\psi_{0YY}=0,\ \theta_{0Y}=0 \qquad \text{at } Y=0 \tag{2.32}$$

$$\psi_{0Y}\to 0\ ,\ \theta_0\to 0 \qquad \text{as } Y\to\infty. \tag{2.33}$$

Equations (2.30) and (2.31) are partial differential equations which can be reduced to ordinary differential equations (Fujii 1963, Gebhart *et al.* 1970) by introducing similarity variables:

$$\eta = Yx^{\frac{n-1}{4}}, \tag{2.34}$$

$$\psi_0 = 4x^{\frac{n+3}{4}}f_0(\eta), \tag{2.35}$$

$$\theta_0 = 4x^n h_0(\eta). \tag{2.36}$$

Here $\eta = 0$ is the mid-plane of the plume [3] and $\eta \to \infty$ is the edge of the plume. The energy convected across any horizontal plane in the thermal plume is not a function of x:

$$Q = \rho C_p \int_{-\infty}^{\infty} (T - T_\infty) u \, dy \tag{2.37}$$

$$= A x^{(3+5n)/4} \int_{-\infty}^{\infty} f'(\eta) h(\eta) \, d\eta, \tag{2.38}$$

where $A = 4\nu\rho c_p N \left(\frac{g\beta N}{4\nu^2}\right)^{1/4}$. The x-independence of Q immediately results into $n = -3/5$. The similarity equations for f_0 and h_0 are obtained from (2.30-2.31)

$$f_0''' + \frac{12}{5} f_0 f_0'' - \frac{4}{5} f_0'^2 + h_0 = 0 \tag{2.39}$$

$$h_0'' + \frac{12}{5} P (f_0 h_0)' = 0. \tag{2.40}$$

The corresponding boundary conditions are [4]

$$f_0(0) = f_0''(0) = h_0' = 0, \, h_0(0) = 1; \quad f_0'(\infty) \to 0, \, h_0(\infty) \to 0. \tag{2.41}$$

It may be pointed out that the solution corresponding to these leading-order similarity equations (2.39-2.40) serves as the base-state for the linear stability analysis of the plume with parallel flow approximation. This will be further discussed in chapter 3.

2.4.2 Higher-order Boundary-Layer Problem

In the outer layer, the solution of the first-order correction term for temperature is $\Theta_1(x, y) = 0$, and the vorticity equation leads to an irrotational type flow governed

[3] The center line temperature is taken to be $T_0 - T_\infty = N x^n$, here N is a proportionality constant.

[4] Fujii (1963) had introduced an addtional condition $I = \int_{-\infty}^{\infty} f' h \, d\eta = 1$ to get the solution of Spalding & Cruddace (1961). This condition is equivalent to $h_0(0) = 1$ for the present case (Pera & Gebhart 1971).

by $\nabla^2\Psi_1(x,y)=0$, with boundary conditions [5]

$$\Psi_1(x,y)_{|_{y=0}} = 4x^{3/5}f_0(\infty), \quad x \geq 0 \tag{2.42}$$

$$= 0, \quad x<0. \tag{2.43}$$

At this order, the outer flow is irrotational with a constant temperature. The solution for the above problem is (Riley 1974)

$$\Psi_1(x,y) = \frac{4f_0(\infty)}{sin\left(\frac{2\pi}{5}\right)}(x^2+y^2)^{\frac{3}{10}}\ sin\left[\frac{3}{5}tan^{-1}\left(\frac{y}{x}\right)+\frac{2\pi}{5}\right]. \tag{2.44}$$

The matching between the inner and outer solutions requires that the correction terms in (2.21) and (2.23) satisfy the following condition:

$$\Psi_{1y}(x,y)_{|_{y=0}} = \psi_{1Y}(x,Y)_{|_{Y\to\infty}} = \frac{12}{5}f_0(\infty)\ cot\left(\frac{2\pi}{5}\right)x^{-2/5}. \tag{2.45}$$

Considering $O(\epsilon^1)$ terms in (2.26) and (2.27), after integrating with respect to Y and setting the resulting arbitary function of x to zero, gives the first-order boundary-layer equations:

$$\psi_{0Y}\psi_{1xY}+\psi_{1Y}\psi_{0xY}-\psi_{0x}\psi_{1YY}-\psi_{1x}\psi_{0YY}-\psi_{1YYY}-\theta_1 = 0, \tag{2.46}$$

$$\psi_{1Y}\theta_{0x}+\psi_{0Y}\theta_{1x}-\psi_{0x}\theta_{1Y}-\psi_{1x}\theta_{0Y}-P^{-1}\theta_{1YY} = 0. \tag{2.47}$$

The corresponding boundary conditions are,

$$\psi_1=\psi_{1YY}=\theta_{1Y}=0 \qquad \text{at} \quad Y=0, \tag{2.48}$$

$$\psi_{1Y} = \frac{12}{5}f_0(\infty)\ cot\left(\frac{2\pi}{5}\right)x^{-2/5},\ \theta_1=0 \qquad \text{as} \quad Y\to\infty. \tag{2.49}$$

Introducing similarity variables as

$$\eta = Yx^{-2/5}, \quad \psi_1=f_1(\eta), \quad \theta_1=x^{-6/5}h_1(\eta), \tag{2.50}$$

[5] Matching between the inner and outer expansions at the edge of boundary-layer ($Y\to\infty$) gives $\frac{\partial\Psi_0(x,y)}{\partial x}_{|_{y=0}} = \frac{\partial\psi_0(x,Y)}{\partial x}_{|_{Y\to\infty}} = \frac{12}{5}x^{-2/5}f_0(\infty), \Rightarrow \psi_0(x,\infty)=4x^{3/5}f_0(\infty)$.

and substituting these terms in the boundary-layer equations (2.46) and (2.47), we obtain similarity equations for first-order correction terms:

$$f_1''' + \frac{12}{5} f_0 f_1'' + \frac{4}{5} f_0' f_1' + h_1 = 0, \tag{2.51}$$

$$h_1'' + \frac{12}{5} P \left(f_0 h_1' + f_1' h_0 + 2 f_0' h_1 \right) = 0. \tag{2.52}$$

The boundary conditions are

$$f_1(0) = f_1''(0) = h_1'(0) = h_1(\infty) = 0,\ f_1'(\infty) = \frac{12}{5} f_0(\infty)\ cot\left(\frac{2\pi}{5}\right). \tag{2.53}$$

It may be recalled that the first-order correction terms, $f_1(\eta)$ and $h_1(\eta)$, take into account streamwise-variations of the flow, and they correspond to non-parallel corrections to the leading-order base flow solution. The composite base flow solution with first-order corrections, $f = f_0 + \epsilon f_1$ and $h = h_0 + \epsilon h_1$, will be used for non-parallel stability analysis in chapter 4.

2.4.3 Analytical Solution of leading-order boundary-layer equations for P = 2

Following Fujii (1963), from the conservation of momentum, the following equation

$$\int_{-\infty}^{\infty} u^2 dy = g\beta \int_0^x \left[\int_{-\infty}^{\infty} (T - T_0) dy \right] dx \tag{2.54}$$

is transformed to

$$\int_{-\infty}^{\infty} \left(f_0'^2 \right) d\eta = \frac{5}{16} \int_{-\infty}^{\infty} h_0 d\eta.$$

$$\Rightarrow \int_{-\infty}^{\infty} \left(f_0'^2 - \frac{5}{16} h_0 \right) d\eta = 0. \tag{2.55}$$

Now we consider the case when the integrand in (2.55) is zero:

$$f_0'^2 = \frac{5}{16} h_0. \tag{2.56}$$

Substituting (2.56) into (2.39), we get:

$$f_0''' + \frac{12}{5} f_0 f_0'' + \frac{12}{5} f_0'^2 = 0, \tag{2.57}$$

which can be integrated twice to yield

$$f_0' + \frac{6}{5} f_0^2 = a, \tag{2.58}$$

where $a = f_0'(0)$.

$$\Rightarrow f_0 = \left(\frac{5a}{6}\right)^{1/2} tanh\left(\frac{6a}{5}\right)^{1/2} \eta, \tag{2.59}$$

Substituting (2.59) into (2.56), we obtain the closed-form solution for h_0:

$$h_0 = \frac{16a^2}{5}\, sech^4\left(\frac{6a}{5}\right)^{1/2} \eta. \tag{2.60}$$

This solution for f_0 and h_0 must satisfy the energy equation (2.40). This requirement leads to a unique value for the Prandtl number $P = 2$. Hence the closed-form solution (2.59) and (2.60) is valid only for $P = 2$.

2.5 Numerical Method for Base State

The similarity equations (2.39-2.40) and (2.51-2.52) are integrated from one end ($\eta = 0$ or ∞) with appropriate boundary conditions by the shooting method. The subsequent corrections to the initial guesses are obtained by matching the boundary conditions at the other end via the Newton-Raphson method. First we need to transform the coupled differential equations into a set of first-order differential equations.
Using the following notations,

$$y_{10} = f_0,\ y_{20} = f_0',\ y_{30} = f_0'',\ \ y_{40} = h_0,\ y_{50} = h_0',$$
$$y_{11} = f_1,\ y_{21} = f_1',\ y_{31} = f_1'',\ \ y_{41} = h_1,\ y_{51} = h_1',$$

the similarity equations are written as a set of first order ODE system.
The leading-order similarity equations are:

$$\left\{\begin{array}{c} f_0{}' \\ f_0{}'' \\ f_0{}''' \\ h_0{}' \\ h_0{}'' \end{array}\right\} = \left\{\begin{array}{c} y_{20} \\ y_{30} \\ -\frac{12}{5}y_{10}y_{30} + \frac{4}{5}y_{20}y_{20} - y_{40} \\ y_{50} \\ -\frac{12}{5}P\left[y_{20}y_{40} + y_1 y_{50}\right] \end{array}\right\}, \tag{2.61}$$

with boundary conditions:

$$f_0(0) = f_0^{''}(0) = h_0^{'}(0) = 0, \quad h_0(0) = 1 \qquad \text{and} \qquad f_0^{'}(\infty) = h_0(\infty) = 0. \tag{2.62}$$

The corresponding similarity equations for first-order corrections are

$$\left\{\begin{array}{c} f_1{}' \\ f_1{}'' \\ f_1{}''' \\ h_1{}' \\ h_1{}'' \end{array}\right\} = \left\{\begin{array}{c} y_{21} \\ y_{31} \\ -\frac{12}{5}y_{10}y_{31} - \frac{4}{5}y_{20}y_{21} - y_{41} \\ y_{51} \\ -\frac{12}{5}P\left[y_{10}y_{51} + y_{21}y_{40} + 2y_{20}y_{41}\right] \end{array}\right\}. \tag{2.63}$$

with boundary conditions:

$$f_1(0) = f_1^{''}(0) = h_1^{'}(0) = h_1(\infty) = 0 \qquad \text{and} \quad f_1^{'}(\infty) = \frac{12}{5}f_0(\infty)cot\left(\frac{2\pi}{5}\right). \tag{2.64}$$

Equations (2.61) and (2.63) are integrated by using the 4^{th}-order Runge-Kutta method whose algorithm is given below.

2.5.1 Algorithm (Runge-Kutta method)

1. Evaluate the functions

$$\begin{aligned} k_1 &= hf(x_n, y_n) \\ k_2 &= hf(x_n + \frac{1}{2}h, y_n + \frac{1}{2}k_1) \\ k_3 &= hf(x_n + \frac{1}{2}h, y_n + \frac{1}{2}k_2) \\ k_4 &= hf(x_n + h, y_n + k_3) \end{aligned}$$

2. Increment the function

$$y_{n+1} = y_n + \frac{1}{6}(k_1 + 2k_2 + 2k_3 + k_4)$$

3. Increment the independent variable

$$x_{n+1} = x_n + h$$

4. Repeat all the steps till the second boundary condition is satisfied to a prescribed accuracy. Newton-Raphson method is used to correct initial guesses as discussed below.

2.5.2 Newton-Raphson Correction

For the leading-order similarity equations (2.39-2.40), all initial values (at $\eta = 0$) are known except $f_0^{'}$. First, we assume some arbitrary value for this quantity $f_0^{'}(0)$ and integrate throughout the domain. Next we slightly perturb the assumed initial value and again repeat the integration. Applying Taylor series expansion for $f_0^{'}$, we have

$$f_0^{'}(a + \Delta a) = f_0^{'}(a) + \frac{df_0^{'}}{da}\Delta a + O(\Delta a^2).$$

But the end boundary condition (at $\eta \to \infty$) suggests that

$$f_0^{'}(a + \Delta a) \mid_{\eta \to \infty} \to 0.$$

This means that $\Delta(a) = -f_0^{'}(a)/(df_0^{'}/da)$ is the increment needed for the next guess value. Now we repeat the same procedure with the corrected guess value till

the end boundary condition is satisfied to a specified accuracy ($f_0^{'}(\eta_e)$; $h_0(\eta_e) \leq 10^{-6}$), where η_e is some large value, taken to be 8.

For the higher-order similarity equations (2.51-2.52), we do not know $f_1{}^{'}$ and h_1 at the initial point (at $\eta = 0$). We can guess some arbitary values for these conditions and can integrate the differential equations. The corrections to these guessed values can be obtained by applying Taylor series approximation for two variables,

$$f_1^{'}(a+\Delta a, b+\Delta b) = f_1^{'}(a,b) + \frac{df_1^{'}}{da}\Delta a + \frac{df_1^{'}}{db}\Delta b + O(\Delta a^2, \Delta b^2), \quad (2.65)$$

$$h_1(a+\Delta a, b+\Delta b) = h_1(a,b) + \frac{dh_1}{da}\Delta a + \frac{dh_1}{db}\Delta b + O(\Delta a^2, \Delta b^2). \quad (2.66)$$

From the end boundary conditions (at $\eta \to \infty$), we have

$$f_1^{'}(a+\Delta a, b+\Delta b)_{|_{\eta\to\infty}} \to \tfrac{12}{5} f_0(\infty)\, cot\left(\tfrac{2\pi}{5}\right) \text{ and}$$
$$h_1(a+\Delta a, b+\Delta b)_{|_{\eta\to\infty}} \to 0.$$

Hence the corrections to the guessed values (Δa, Δb) are computed from the linear system given below:

$$\begin{bmatrix} \frac{df_1^{'}}{da} & \frac{df_1^{'}}{db} \\ \\ \frac{dh_1}{da} & \frac{dh_1}{db} \end{bmatrix} \begin{bmatrix} \Delta a \\ \\ \Delta b \end{bmatrix} = \begin{bmatrix} \frac{12}{5} f_0(\infty) cot\left(\frac{2\pi}{5}\right) - f_1^{'}(a,b) \\ \\ -h_1(a,b) \end{bmatrix}. \quad (2.67)$$

These corrections are added to the guessed values and the integration is repeated. This procedure is carried out untill the end boundary conditions are satisfied to a specified accuracy $\left(\frac{12}{5} f_0(\eta_e) cot\left(\frac{2\pi}{5}\right) - f_1^{'}(\eta_e),\ h_1(\eta_e) \leq 10^{-6}\right)$.

2.6 Results

To ascertain the accuracy of the numerical method, the analytical solutions (2.59-2.60) are computed for $P = 2$. In figure 2.2, both the analytical and numerical solutions are plotted. The analytical solutions for the stream function (f_0) and the temperature (h_0) agree well with numerical computations.

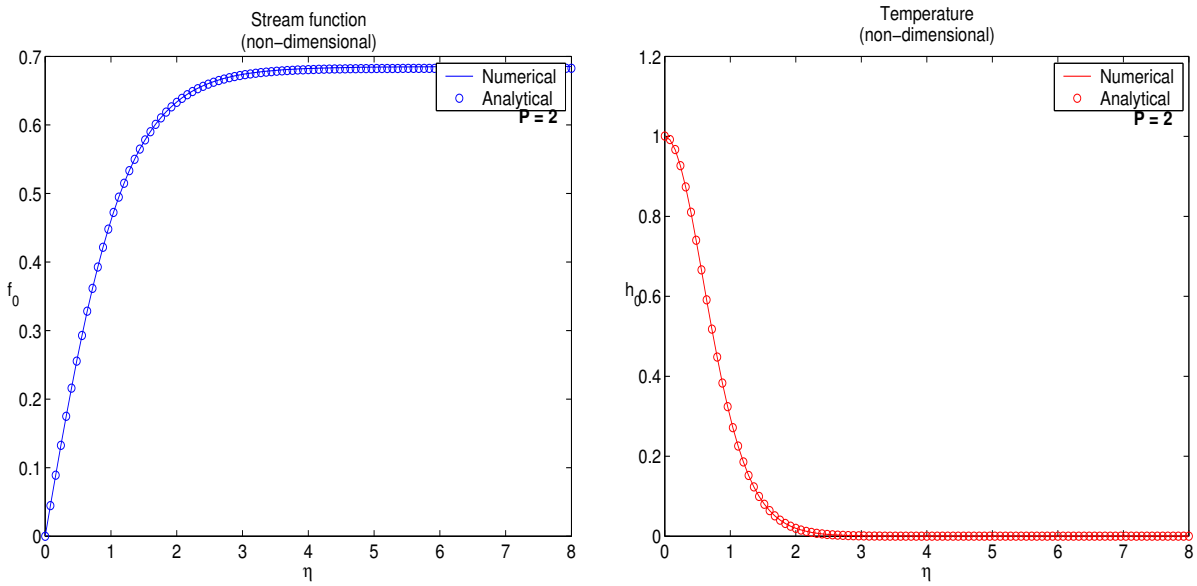

Figure 2.2: Validation of numerical method with analytical solution for P = 2

Numerical solutions are computed for different Prandtl numbers in the range $P = 0.7, 6.7, 100, 200, 1000$. Computations have been carried out for different grid sizes (101, 201, 301 points) with uniform and cosine grids. For the uniform grid, the distance between two successive grid points is same through out the computational domain. In case of cosine grid, the location of grid points is given by

$$\eta_j = cos\left(\frac{j\pi}{N}\right), \quad \text{where } j = 0,\ 1,\ 2,\ ...,\ N-1 \tag{2.68}$$

in the transformed plane ($\eta = -1$ to 1). The advantage of using cosine grids over uniform grid is the improved resolution of the computational domain near the center-line of the plume. No significant difference in velocity or temperature was found by increasing the grid resolution.

It is clear from figure 2.3 that with increasing Prandtl number, the thermal boundary-layer becomes thinner and the velocity levels are decreased in the plume. Because the thermal diffusion is smaller at larger P, the thermal boundary-layer becomes more confined near the verticle line at the source as the Prandtl number is increased. Since the viscous diffusion is more for high Prandtl number fluids, the velocity profile becomes flatter with increasing P. For a given Prandtl number P, the maximum temperature in the plume decreases (at constant η) as minus three-fifth power of the height.

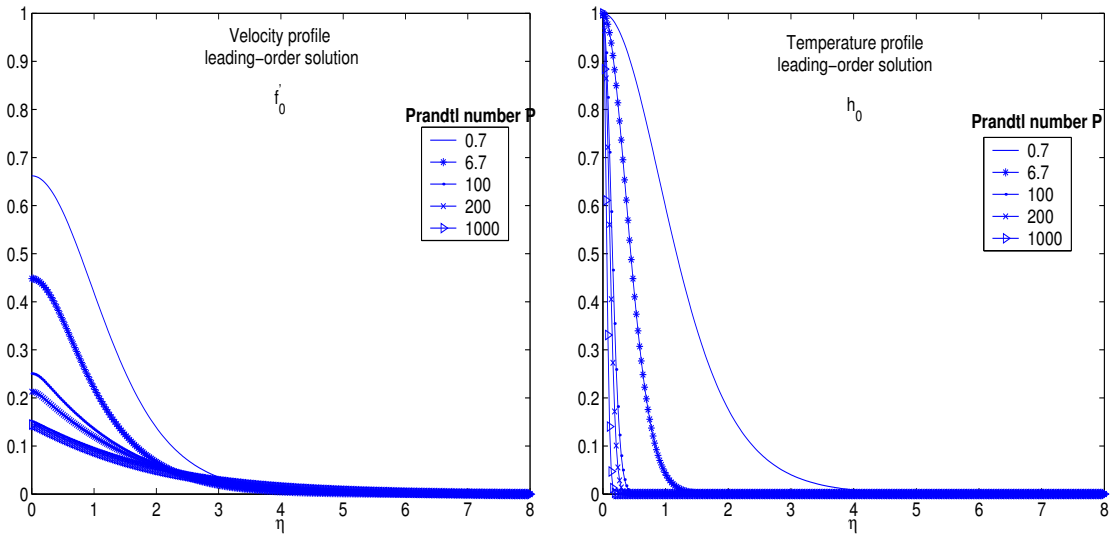

(a) (b)

Figure 2.3: Profiles of (a) velocity (leading-order solution), (b) temperature (leading-order solution).

Figure 2.4 shows the first-order correction terms for the velocity and temperature fields. Figures 2.5 and 2.6 show the velocity and temperature profiles with first-order corrections for $\epsilon = Gr^{-1/4} = 0.01$ and 0.05, respectively. The true nature of the base flow is revealed by including the higher-order effects to the classical (leading-order) boundary-layer solutions. Adding $O(\epsilon^1)$ terms lead to a decrease in the centerline temperature from unity and an increase of the flow velocity. These increase in velocity (see Figure 2.4) and decrease in temperature becomes smaller with increasing Prandtl number. This clearly suggests that a high Prandtl number thermal plume can be modelled by the leading-order boundary-layer equations.

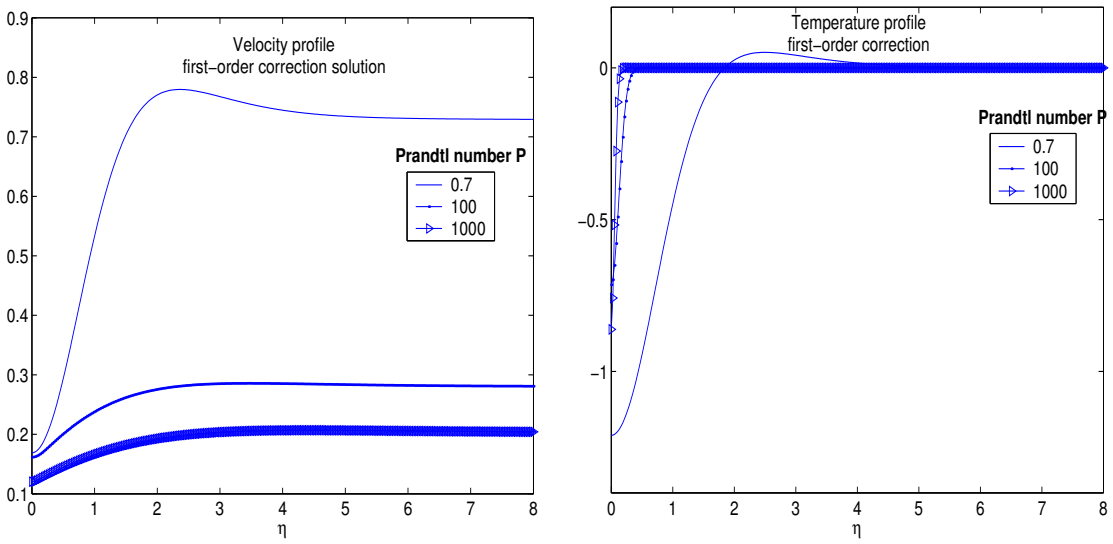

(a) (b)

Figure 2.4: Profiles of (a) velocity (first-order correction), (b) temperature (first-order correction).

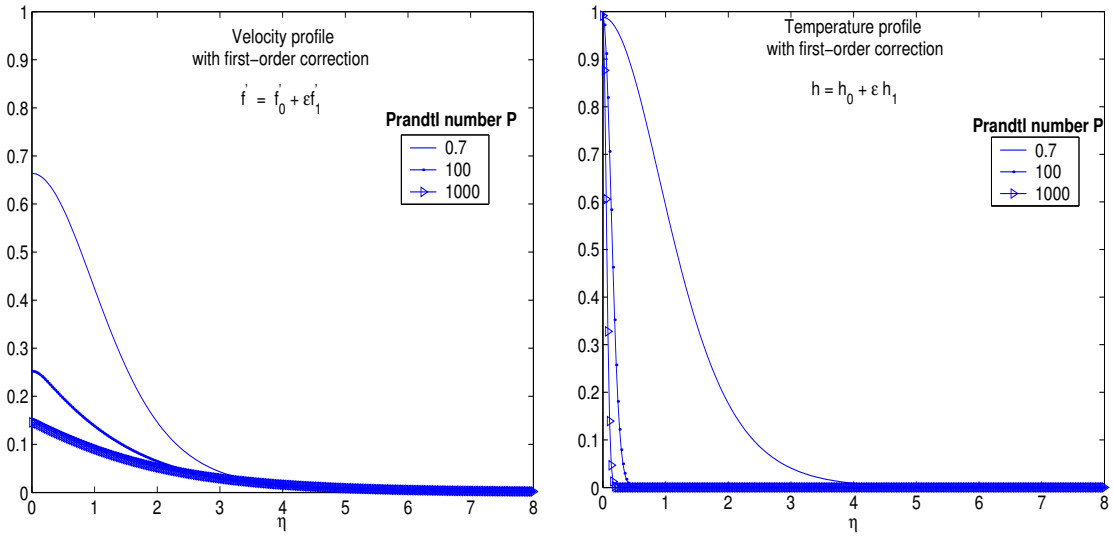

(a) (b)

Figure 2.5: Profiles of (a) velocity and (b) temperature with first-order corrections for $\epsilon = 0.01$.

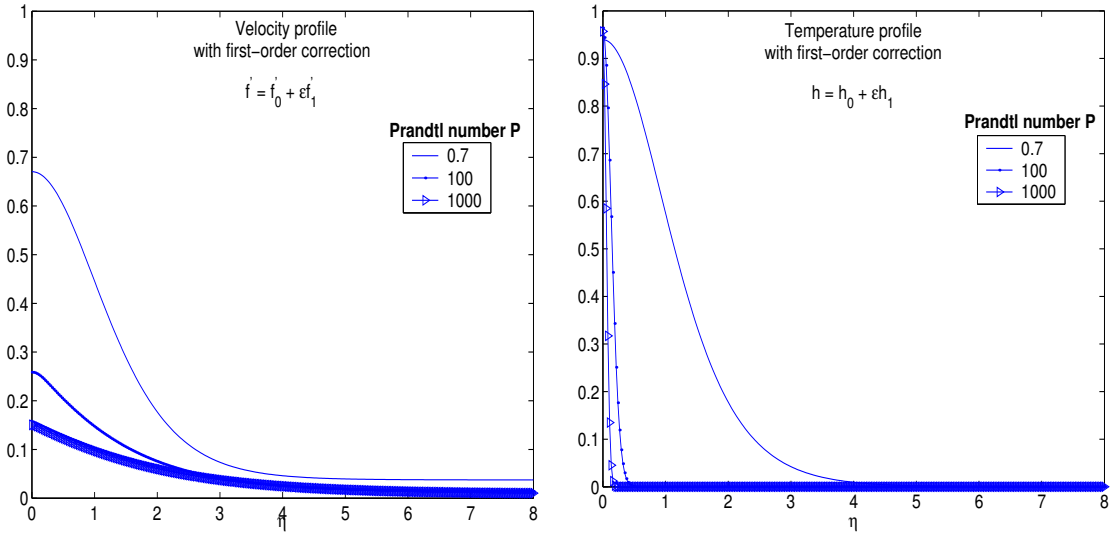

(a) (b)

Figure 2.6: Profiles of (a) velocity and (b) temperature with first-order corrections for $\epsilon = 0.05$.

2.7 Analogy with the mean flow characteristics of Bubble Plume

For two-phase bubbly flows (see Figure 1.5), the transport of buoyancy is achieved by the motion of the bubbles. At low Reynolds numbers with small volume fraction, a single bubble rises in a rectilinear trajectory and the hydrodynamic interactions lead to only weak lateral diffusion of the bubble plume. Such bubbly flows are likely to behave as high Prandtl number thermal plumes. This possible analogy between a bubble plume and a high-Prandtl number thermal plume was suggested by Alam & Arakeri (1993). The parameter representative of the collective effects induced by bubbles was shown to be a *Grashof number* based on source conditions.

This analogy has been further explored recently by Caballina *et al.* (2003) via Euler-Lagrange-type numerical simulation of a bubble plume. They showed that the vertical velocity profiles of a bubble plume collapse onto a single plot (see figure 2.7) irrespective of the source Grashof number or the fluid viscosity. They further showed that their computed velocity profile in the core region agrees perfectly with the similarity solution of an infinite Prandtl number thermal plume (Spalding &

Cruddace 1961); of course, there are some discrepancies far away from the source as seen in figure 2.7. It is clear, therefore, that in the laminar regime the liquid velocity field induced by the bubbles can be approximated by that of a high Prandtl number thermal plume.

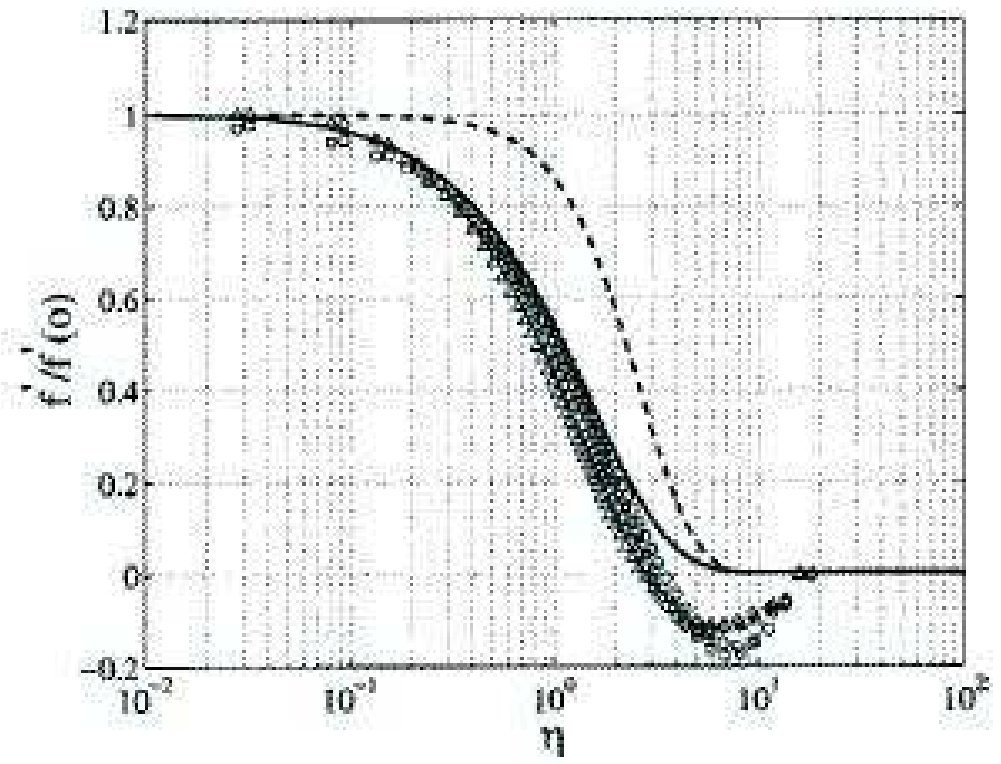

FIG. 3. Self-similar profile in the steady laminar region. Similar profiles have been obtained for $Y/L_0 = 24$. $Gr_0 = 21$: □, $\nu = 1 \times 10^{-5}$ m^2/s; △, $\nu = 1 \times 10^{-6}$ m^2/s. $Gr_0 = 43$: ○, $\nu = 1 \times 10^{-5}$ m^2/s; ◇, $\nu = 1 \times 10^{-6}$ m^2/s. A comparison with thermal plumes: -, Pr = ∞ [Spalding and Cruddace (Ref. 24)]; --, Pr = 0.7 [Fujii (Ref. 23)].

Figure 2.7: Velocity profiles for bubble and thermal plumes (taken from Caballina *et al.* 2003)

CHAPTER 3

LINEAR STABILITY ANALYSIS

The transition from laminar to turbulent flow in a thermal buoyant plume has drawn attention of many investigators (Pera & Gebhart 1971; Halland & Sparrow 1973; Hieber & Nash 1975; Wakitani 1985). The linear stability analysis is done by perturbing a steady-state solution of the equations of motion with infinitesimal velocity and temperature disturbances. If the disturbance decays, the flow is said to be stable. If the disturbance amplifies or remains at some level different from zero, the flow is said to be, respectively, unstable or neutrally stable. In many flows, the two-dimensional disturbances amplify at a lower Reynolds number than three-dimensional disturbances, and hence the $2D$-modes are least stable- this is Squire's theorem. Knowles & Gebhart (1971) showed that this theorem also holds for natural convection flows; so it is sufficient to consider only two-dimensional disturbances for the linear stability analysis of a thermal plume.

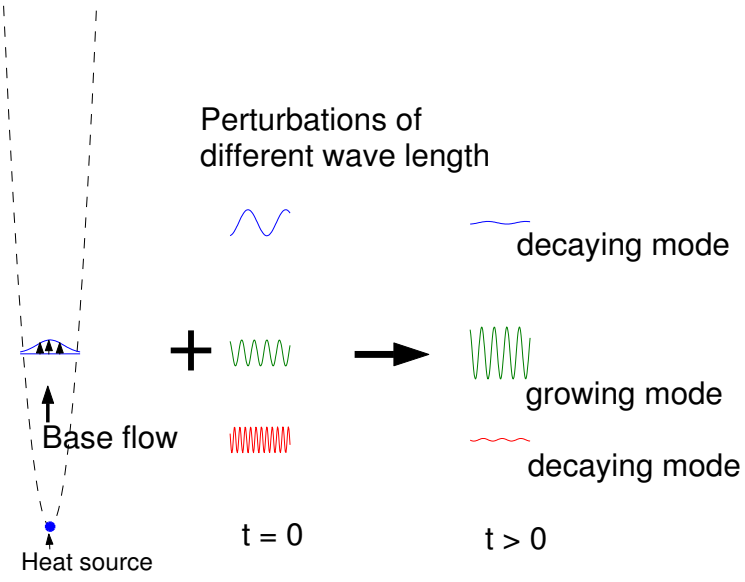

Figure 3.1: Schematic of growing or decaying perturbations in a plume.

In this chapter, we formulate the linear stability problem of a thermal plume,

following the earlier work of Wakitani (1985). The analysis considers both parallel and non-parallel effects. With parallel flow approximation, the temporal stability problem of a thermal plume is then studied in detail for a range of Prandtl number.

3.1 General Analysis with Non-parallel Effects

The stability of a two-dimensional plume above a horizontal line source of heat is examined by inquiring whether a small disturbance, superimposed on the base flow and satisfying the governing continuity, momentum and energy equations, is amplified or damped with time or space. The base flow is described by the stream function $\Psi(x, y)$ and the temperature $T(x, y)$. Now we rescale the problem in terms of new coordinates (ξ, η), following the method described in Gaster (1974) and Wakitani (1985):

$$\xi = \frac{x}{x_0}, \quad \eta = \frac{y}{x}\left(\frac{Gr_x}{4}\right)^{1/4} = \left(\frac{G}{4x_0}\right) y\xi^{-2/5}, \tag{3.1}$$

where

$$Gr_x = \frac{g\beta(T_0(x) - T_\infty)x^3}{\nu^2}, \tag{3.2a}$$

$$Gr_{x_0} = \frac{g\beta(T_0(x_0) - T_\infty)x_0^3}{\nu^2}, \tag{3.2b}$$

$$G = 2\sqrt{2}Gr_{x_0}^{1/4}, \tag{3.2c}$$

$$T_0(x) \equiv T(x, y = 0). \tag{3.2d}$$

As described in chapter 2, for the buoyant plume, the stream function and the temperature of the base flow (with first-order corrections) can be expressed as

$$\Psi = \nu\left\{G\xi^{3/5}f_0(\eta) + 4f_1(\eta)\right\}, \tag{3.3}$$

$$T - T_\infty = N{x_0}^{-3/5}\xi^{-3/5}\left\{h_0(\eta) + \frac{4}{G}\xi^{-3/5}h_1(\eta)\right\}. \tag{3.4}$$

The disturbances are superimposed on this base flow; the stream function and temperature of the disturbed flow are assumed to have the form:

$$\tilde{\psi}(x,y,\tilde{\tau}) = \Psi(x,y) + \psi(x,y,\tilde{\tau}), \tag{3.5}$$

$$\tilde{\theta}(x,y,\tilde{\tau}) = T(x,y) + \theta(x,y,\tilde{\tau}). \tag{3.6}$$

Substituting the above decomposition into the Navier-Stokes and energy equations, subtracting the equations for the base flow and neglecting the nonlinear terms in the disturbance quantities, we obtain governing equations for the disturbance variables

$$\begin{aligned} &\frac{\partial}{\partial\tilde{\tau}}(\nabla^2\psi) + \frac{\partial\Psi}{\partial y}\frac{\partial}{\partial x}(\nabla^2\psi) + \frac{\partial}{\partial x}(\nabla^2\Psi)\frac{\partial\psi}{\partial y} \\ &\qquad -\frac{\partial\Psi}{\partial x}\frac{\partial}{\partial y}(\nabla^2\psi) - \frac{\partial}{\partial y}(\nabla^2\Psi)\frac{\partial\psi}{\partial x} = g\beta\frac{\partial\theta}{\partial y} + \nu\nabla^4\psi, \end{aligned} \tag{3.7}$$

$$\frac{\partial\theta}{\partial\tilde{\tau}} + \frac{\partial\Psi}{\partial y}\frac{\partial\theta}{\partial x} + \frac{\partial T}{\partial x}\frac{\partial\psi}{\partial y} - \frac{\partial\Psi}{\partial x}\frac{\partial\theta}{\partial y} - \frac{\partial T}{\partial y}\frac{\partial\psi}{\partial x} = \kappa\nabla^2\theta. \tag{3.8}$$

The initial disturbance is assumed to exist at a location $x = x_0$, time $\tilde{\tau} = 0$ and the solutions are sought for $\tilde{\tau} > 0$ in the case of temporal stability problem and $x > x_0$ for spatial stability problem. In terms of the new coordinates ξ and η, the spatial derivatives transform into

$$\frac{\partial}{\partial x} = \frac{1}{x_0}\left(\frac{\partial}{\partial\xi} - \frac{2}{5}\eta\xi^{-1}\frac{\partial}{\partial\eta}\right), \quad \frac{\partial}{\partial y} = \left(\frac{G}{4x_0}\right)\xi^{-2/5}\frac{\partial}{\partial\eta} \quad . \tag{3.9}$$

The normal mode solutions for the disturbances are assumed (Wakitani 1985):

$$\psi = \frac{\nu G}{4}\xi^{3/5}\phi(\xi,\eta)e^{i\Omega}, \tag{3.10}$$

$$\theta = \frac{G^3}{4^3}N{x_0}^{-3/5}\xi^{-3/5}s(\xi,\eta)e^{i\Omega}, \tag{3.11}$$

$$\Omega = \frac{G}{4}\int_1^{\xi}\xi^{-2/5}\alpha(\xi)d\xi - \omega\tau, \tag{3.12}$$

$$\frac{\partial}{\partial\tilde{\tau}} = \left(\frac{\nu G^3}{4^2x_0^2}\right)\xi^{-1/5}\frac{\partial}{\partial\tau} \quad . \tag{3.13}$$

Here α is the dimensionless wavenumber, ω is the dimensionless frequency and τ is the dimensionless time. Substituting the equations (3.1-3.13) in the disturbance governing equations (3.7) and (3.8) yields

$$L_1\phi + (G\xi^{3/5})^{-1}\left[\frac{\partial s}{\partial \eta} - 4\left(2\alpha\omega - 3\alpha^2 {f_0}' - {f_0}'''\right)\left(\xi\frac{\partial \phi}{\partial \xi} - \frac{2}{5}\eta\frac{\partial \phi}{\partial \eta} + \frac{3}{5}\phi\right)\right.$$
$$-4\left\{\left(\omega - 3\alpha {f_0}'\right)\left(\xi\frac{\partial \alpha}{\partial \xi} - \frac{2}{5}\alpha\right)\right\}\phi - 4i\alpha\left\{{f_1}'\left(\frac{\partial^2\phi}{\partial\eta^2} - \alpha^2\phi\right) - {f_1}'''\phi\right\}$$
$$+\frac{4}{5}\left({f_0}'' + 2\eta {f_0}'''\right)\frac{\partial\phi}{\partial\eta} + \frac{4}{5}\left\{\left(3f_0 - 2\eta {f_0}'\right)\left(\frac{\partial^2}{\partial\eta^2} - \alpha^2\right)\frac{\partial\phi}{\partial\eta}\right\}$$
$$\left.-4{f_0}'\left\{\xi\frac{\partial^2}{\partial\eta^2}\left(\frac{\partial\phi}{\partial\xi}\right) - \frac{2}{5}\eta\frac{\partial^3\phi}{\partial\eta^3} - \frac{1}{5}\frac{\partial^2\phi}{\partial\eta^2}\right\}\right] + O\left(\epsilon^2\right) = 0, \tag{3.14}$$

$$L_2 s + i\alpha {h_0}' - \left(G\xi^{3/5}\right)^{-1}\left[4\xi\left({f_0}'\frac{\partial s}{\partial\xi} - {h_0}'\frac{\partial\phi}{\partial\xi}\right) + i\alpha\left(4{f_1}' s - {h_1}'\phi\right)\right.$$
$$\left.-\frac{3}{5}\left(4h_0\frac{\partial\phi}{\partial\eta} + 4{h_0}'\phi + f_0\frac{\partial s}{\partial\eta} + 4{f_0}' s\right)\right] + O\left(\epsilon^2\right) = 0, \tag{3.15}$$

where the primes ($'$) denote differentiation with respect to η and the linear operators L_1 and L_2 are

$$L_1 = \left(G\xi^{\frac{3}{5}}\right)^{-1}\left(\frac{\partial^4}{\partial\eta^4} - 2\alpha^2\frac{\partial^2}{\partial\eta^2} + \alpha^4\right) - i\alpha\left[\left({f_0}' - \frac{\omega}{\alpha}\right)\left(\frac{\partial^2}{\partial\eta^2} - \alpha^2\right) - {f_0}'''\right], \tag{3.16}$$

$$L_2 = \left(PG\xi^{\frac{3}{5}}\right)^{-1}\left(\frac{\partial^2}{\partial\eta^2} - \alpha^2\right) - i\alpha\left({f_0}' - \frac{\omega}{\alpha}\right). \tag{3.17}$$

The solutions for ϕ and s are assumed to be of the form (Gaster 1974; Wakitani 1985)

$$\phi(\xi,\eta) = A(\xi)\phi_0(\eta;\xi) + \epsilon\phi_1(\xi,\eta) + O(\epsilon^2), \tag{3.18}$$
$$s(\xi,\eta) = A(\xi)s_0(\eta;\xi) + \epsilon s_1(\xi,\eta) + O(\epsilon^2). \tag{3.19}$$

Here $A(\xi)$ is a weak function of ξ that takes account of the streamwise variations of the wavenumber and eigenfunctions- this essentially incorporates non-parallel effects as we shall see below. After substituting (3.18-3.19) in (3.14-3.15), and collecting the leading and first-order terms we get

$O(\epsilon^0)$:

$$\mathbf{L\Phi_0} = 0, \tag{3.20}$$

$O(\epsilon^1)$:

$$\mathbf{L\Phi_1} = \mathbf{M}. \tag{3.21}$$

Here the linear operators are

$$\mathbf{L} \equiv \begin{bmatrix} L_1 & \left(G\xi^{3/5}\right)^{-1} D \\ i\alpha h_0^{'} & L_2 \end{bmatrix}, \quad \mathbf{\Phi_j} \equiv \begin{pmatrix} \phi_j \\ s_j \end{pmatrix} \quad \text{with} \quad \text{j = 0,1} \quad \text{and}$$

$$\mathbf{M} \equiv \begin{pmatrix} F_1 + F_2\xi\frac{dA}{d\xi} \\ \\ F_3 + F_4\xi\frac{dA}{d\xi} \end{pmatrix},$$

with the expressions for F_i being,

$$\begin{aligned}
F_1 &= 4\Big(2\alpha\omega - 3\alpha^2 f_0^{'} - f_0^{'''}\Big)\left(\xi\frac{\partial\phi_0}{\partial\xi} - \frac{2}{5}\eta\frac{\partial\phi_0}{\partial\eta} + \frac{3}{5}\phi_0\right) + 4\Big(\omega - 3\alpha f_0^{'}\Big)\left(\xi\frac{\partial\alpha}{\partial\xi}\right)\phi_0 + \\
&\quad 4i\alpha\left[f_1^{'}\left(\frac{\partial^2}{\partial\eta^2} - \alpha^2 - f_1^{'''}\right)\phi_0 - \frac{4}{5}\left(f_0^{''} + 2\eta f_0^{'''}\right)\frac{\partial\phi_0}{\partial\eta}\right. \\
&\quad \left. -\frac{4}{5}\left(3f_0 - 2\eta f_0^{'}\right)\left(\frac{\partial^2}{\partial\eta^2} - \alpha^2\right)\frac{\partial\phi_0}{\partial\eta} + 4f_0^{'}\left[\xi\frac{\partial^2}{\partial\eta^2}\left(\frac{\partial\phi_0}{\partial\xi}\right) - \frac{2}{5}\eta\frac{\partial^3\phi_0}{\partial\eta^3} - \frac{1}{5}\frac{\partial^2\phi_0}{\partial\eta^2}\right], \\
F_2 &= 4\left(2\alpha\omega - 3\alpha^2 f_0^{'} - f_0^{'''}\right)\phi_0 + 4f_0^{'}\frac{\partial^2\phi_0}{\partial\eta^2}, \\
F_3 &= 4\xi\left(f_0^{'}\frac{\partial s_0}{\partial\xi} - h_0^{'}\frac{\partial\phi_0}{\partial\xi}\right) + i\alpha\left(4f_1^{'}s_0 - h_1^{'}\phi_0\right) - \frac{3}{5}\left(4h_0\frac{\partial\phi_0}{\partial\eta} + 4h_0^{'}\phi_0 + f_0\frac{\partial s_0}{\partial\eta} + 4f_0^{'}s_0\right), \\
F_4 &= 4\left(f_0^{'}s_0 - h_0^{'}\phi_0\right).
\end{aligned}$$

The boundary conditions are

$$\phi_j(\pm\infty) = \phi_j^{'}(\pm\infty) = s_j(\pm\infty) = 0 \tag{3.22}$$

for j=0 and 1. Defining a modified Grashof number as

$$G^* = G\xi^{\frac{3}{5}} \equiv 2\sqrt{2}Gr_x^{1/4}, \tag{3.23}$$

we can formulate the eigenvalue problem by specifying any two parameters out of three parameters G^*, α and ω. Note that the boundary conditions can be simplified if we focus on symmetric and asymmetric disturbances separately.

3.1.1 Symmetric disturbances

For this type of disturbances (Pera & Gebhart 1971), the disturbance stream function, $\phi(\eta)$, is an odd function of η, and the disturbance temperature, $s(\eta)$, is an even function of η. The boundary conditions at the mid-plane are

$$\phi(0) = \phi^{''}(0) = s^{'}(0) = 0. \tag{3.24}$$

There is no change in the horizontal disturbance velocity component from the center line, so that the derivative of that component is zero and there is no change in the gradient of temperature disturbance when it is a symmetric disturbance.

3.1.2 Asymmetric disturbances

For this type of disturbances, the disturbance stream function, $\phi(\eta)$, is an even function of η, and the disturbance temperature, $s(\eta)$, is an odd function of η. The boundary conditions at the mid-plane are

$$\phi^{'}(0) = \phi^{'''}(0) = s(0) = 0. \tag{3.25}$$

It is well known that thermal plumes are more unstable to asymmetric disturbances (Pera & Gebhart 1971), so further analysis is carried out only for this type of disturbances.

The linear stability equations with $O(\epsilon^0)$ terms, (3.20), represent the parallel flow approximation, and those with $O(\epsilon^1)$ terms, (3.21), represent non-parallel corrections.

3.2 Parallel Flow Approximation

At high Grashof numbers (Gr) we can assume that the flow is parallel, so that the streamwise variations can be neglected for the base flow as well as for the distur-

bance amplitudes. Under this parallel flow assumption, the first-order boundary-layer equations describe the mean flow and the Orr-Sommerfeld equations describe the disturbance propagation. The rest of this chapter deals with the stability of thermal plumes with parallel flow approximation:

a) The base flow is taken as that resulting from the leading-order similarity solution.
b) Only the leading-order terms in the disturbance quantities are retained.
c) After the approximations (a) and (b) are made, the base flow quantities in the transverse direction, and the ξ-derivatives of the streamwise velocity and temperature are taken as zero.
d) The postulated disturbances are assumed to be of the form such that the amplitude functions depend, as does the base flow, only on the similarity variable η but not on ξ.

With the above approximations, the governing disturbance equations (at $O(\epsilon^0)$) are,

$$\left(\phi^{''''} - 2\alpha^2\phi^{''} + \alpha^4\phi\right) + s^{'} = i\alpha G^* \left[\left(f^{'} - \frac{\omega}{\alpha}\right)\left(\phi^{''} - \alpha^2\phi\right) - f^{'''}\phi\right], \tag{3.26}$$

$$s^{''} - \alpha^2 s = i\alpha P G^* \left[\left(f^{'} - \frac{\omega}{\alpha}\right) s - h^{'}\phi\right]. \tag{3.27}$$

The equations (3.26) and (3.27) are the analogue of the Orr-Sommerfeld equation for convective flows and the corresponding boundary conditions (asymmetric disturbances) are

$$\phi^{'}(0) = \phi^{'''}(0) = s(0) = 0; \qquad \phi(\infty) \to 0,\ \phi^{'}(\infty) \to 0,\ s(\infty) \to 0. \tag{3.28}$$

3.3 Formulation of Temporal Stability Problem

For temporal stability analysis, the disturbances are allowed to grow or decay in time:

$$\Phi(x, y, \tilde{\tau}) = \Phi(y) e^{i(\alpha x - \omega\tilde{\tau})},$$

with the wavenumber α being real and the frequency $\omega = \omega_r + i\omega_i$ is complex. The disturbance grows or decays in time if $\omega_i > 0$ or $\omega_i < 0$, respectively. In the linear stability equations, ω appears linearly and can be computed from the associated generalized eigenvalue problem (3.26-3.27) for a given wavenumber (α) and modified Grashof number ($G^* = G\xi^{3/5}$).

3.4 Numerical Methods for Linear Stability Equations

To discretize stability equations (3.26) and (3.27) with the boundary conditions (3.28) for asymmetric disturbances we use two methods.
1) Finite difference technique with 2^{nd} order central difference scheme,
2) Spectral collocation method with Tchebychev polynomials.
The eigenvalues obtained from these two numerical methods will subsequently be compared to ascertain the accuracy of the reported stability results.

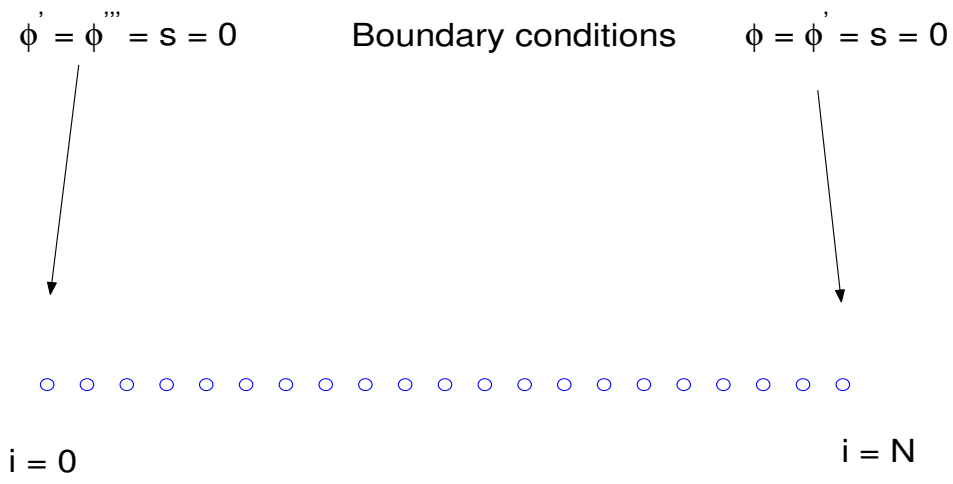

Figure 3.2: Domain discretization

3.4.1 Finite Difference Technique

In this method we use central difference scheme of 2^{nd} order accuracy. The entire domain is divided into (N+1) points, starting from 0 to N. Now we write the

linear stability equations (3.26) and (3.27) in discretized form (considering only leading-order terms)

$$\left(\phi_i^{''''} - 2\alpha^2\phi_i^{''} + \alpha^4\phi_i + s_i^{'}\right) = i\alpha G^* \left[(f_i^{'} - \frac{\omega}{\alpha})(\phi_i^{''} - \alpha^2\phi_i) - f_i^{'''}\phi_i\right] \tag{3.29}$$

$$s_i^{''} - \alpha^2 s_i = i\alpha PG^* \left[(f_i^{'} - \frac{\omega}{\alpha})s_i - h_i^{'}\phi_i\right] \tag{3.30}$$

and the discretized boundary conditions are

$$\phi^{'}(0) = \phi^{'''}(0) = s(0) = 0, \quad \phi(N) = \phi^{'}(N) = s(N) = 0. \tag{3.31}$$

Here Δx is the grid spacing between two nodes. In the above equations (3.29) and (3.30), $\phi_0, \phi_1, \phi_2, ..., \phi_{N-1}$ and $s_1, s_2, ..., s_{N-1}$ are unknown values. Writing the disturbance energy equation (3.27) at the zeroth node gives,

$$s_0^{''} = -i\alpha PG^* h_0^{'}\phi_0 \quad . \tag{3.32}$$

Since $s_0^{''} = (s_{-1} - 2s_0 + s_1)/\Delta x^2 = -i\alpha PG^* h_0^{'}\phi_0$,
where $s_{-1} = -s_1 - i\alpha PG^* h_0^{'}\Delta x^2\phi_0$, whenever s_{-1} appears in any equation we can replace it with this value. Now the term $s_i^{'}$ at the zeroth node gives

$$s_0^{'} = (s_1 - s_{-1})/(2\Delta x) \tag{3.33}$$

$$= \left(\frac{i\alpha PG^* h_0^{'}}{2}\right)\phi_0 + \frac{s_1}{\Delta x} \quad . \tag{3.34}$$

The differentiation matrices for ϕ and s are

$$\phi_i^{''''} = \frac{1}{\Delta x^4}(\phi_{i+1}^{''} - 2\phi_i^{''} + \phi_{i-1}^{''})$$

$$\phi_i^{''} = \frac{1}{\Delta x^2}(\phi_{i-1} - 2\phi_i + \phi_{i+1})$$

$$s_i^{''} = \frac{1}{\Delta x^2}(s_{i-1} - 2s_i + s_{i+1})$$

$$s_i^{'} = \frac{1}{2\Delta x}(s_{i+1} - s_{i-1})$$

Writing the differentiation matrices

$$\phi'''' = [A][\phi], \quad \phi'' = [B][\phi], \quad s'' = [D][s], \quad s' = [E][s],$$

where the matrices A, B, D, E are

$$A = \frac{1}{\Delta x^4}\left[\begin{array}{cccccc|cccccc} 6 & -8 & 2 & 0 & 0 & 0 & & & & & & \\ -4 & 7 & -4 & 1 & 0 & 0 & & & & & & \\ 1 & -4 & 6 & -4 & 1 & 0 & & & 0 & & & \\ 0 & 1 & -4 & 6 & -4 & 1 & & & & & & \\ \hline & & & & & & 1 & -4 & 6 & -4 & 1 & \\ & & & 0 & & & 0 & 1 & -4 & 6 & -4 & \\ & & & & & & 0 & 0 & 1 & -4 & 7 & \end{array}\right]_{N\times N} \tag{3.35}$$

$$B = \frac{1}{\Delta x^2}\left[\begin{array}{cccc|cccc} -2 & 2 & 0 & 0 & & & & \\ 1 & -2 & 1 & 0 & & & 0 & \\ 0 & 1 & -2 & 1 & & & & \\ \hline & & & & 0 & 1 & -2 & 1 \\ & & 0 & & 0 & 0 & 1 & -2 \end{array}\right]_{N\times N} \tag{3.36}$$

$$D = \frac{1}{\Delta x^2}\left[\begin{array}{ccc|ccc} -2 & 1 & 0 & & & \\ 1 & -2 & 1 & & 0 & \\ & & & & & \\ \hline & & & 1 & -2 & 1 \\ & 0 & & 0 & 1 & -2 \end{array}\right]_{(N-1)\times(N-1)} \tag{3.37}$$

$$E = \frac{1}{\Delta x}\left[\begin{array}{ccc|ccc} 1 & 0 & 0 & & & \\ 0 & 1/2 & 0 & & 0 & \\ & & & & & \\ \hline & & & -1/2 & 0 & 1/2 \\ & 0 & & 0 & -1/2 & 0 \end{array}\right]_{N\times(N-1)} \tag{3.38}$$

Finally, we write the discretized linear stability equations (3.29-3.30) as a generalized eigenvalue problem:

$$\mathbf{A\Phi} = \omega\mathbf{B\Phi}, \tag{3.39}$$

where

$$\mathbf{A} \equiv \left[\begin{array}{c|c} [a_{11}]_{N\times N} & [a_{12}]_{N\times(N-1)} \\ \hline [a_{21}]_{(N-1)\times N} & [a_{22}]_{(N-1)\times(N-1)} \end{array}\right], \quad \mathbf{B} \equiv \left[\begin{array}{c|c} b_{11} & b_{12} \\ \hline b_{21} & b_{22} \end{array}\right], \quad \mathbf{\Phi} \equiv \left[\begin{array}{c} \phi \\ s \end{array}\right]. \tag{3.40}$$

and

$$\begin{aligned}
[a_{11}]_{N\times N} &= \frac{i}{G^*}\big([A] - 2\alpha^2[B] + \alpha^4[I_1]\big) + \alpha[f^{'}]\big([B] - \alpha^2[I_1]\big) - \alpha[f^{'''}] \\
&\quad -\alpha\frac{Ph_0^{'}\Delta x}{2}\begin{bmatrix} 1 & 0 & 0 & 0 & . & . \\ 0 & 0 & 0 & 0 & . & . \\ . & . & . & . & . & . \\ 0 & 0 & 0 & . & . & . \end{bmatrix} \\
[a_{12}]_{N\times(N-1)} &= \frac{i}{G^*}[E]_{N\times(N-1)} \\
[a_{21}]_{(N-1)\times N} &= -\alpha\begin{bmatrix} 0 & h_1^{'} & 0 & 0 & . & . \\ 0 & 0 & h_2^{'} & 0 & . & . \\ . & . & . & . & . & . \\ 0 & 0 & 0 & . & . & h_{N-1}^{'} \end{bmatrix} \\
[a_{22}]_{(N-1)\times(N-1)} &= \frac{i}{PG^*}\big([D] - \alpha^2[I_2]\big) + \alpha[f^{'}] \\
[b_{11}]_{N\times N} &= [B] - \alpha^2[I] \\
[b_{22}]_{N\times N} &= [I_2]
\end{aligned}$$

and $[I_1]_{N\times N}$, $[I_2]_{(N-1)\times(N-1)}$ are the unit matrices.

3.4.2 Spectral-Collocation Method

In spectral-collocation method, the differential equations are discretized at (N+1)-number of collocation points and the computational domain is mapped to $(-1, 1)$. Here the collocation points y_j in the interval $(-1, 1)$ are not distributed uniformly, as in the finite difference method, but according to a cosine law. Their locations are given by

$$y_j = cos\left(\frac{j\pi}{N}\right), \qquad \text{j=0, 1, 2, ..., N;} \tag{3.41}$$

these are called Gauss-Lobatto points (Canuto *et al.* 1988).
In the spectral-collocation method, the derivative $\frac{d}{dy}$ is replaced by a matrix D whose elements are

$$\begin{aligned} D(k,j) &= \frac{\hat{c}_k(-1)^{k+j}}{\hat{c}_j(y_k - y_j)} \quad \text{with} \quad 0 \le k,\, j \le N,\, k \ne j \\ D(k,k) &= \frac{-y_k}{2(1-y_k^2)} \quad \text{with} \quad 1 \le k \le N-1 \\ D(0,0) &= \frac{2N^2+1}{6} \quad \text{where } \hat{c}_0 = \hat{c}_N = 2,\, \hat{c}_j = 1 \text{ with} \quad 1 \le j \le N-1 \\ &= -D(N,N). \end{aligned}$$

The dimension of matrix D is $(0:N, 0:N)$.
a) The vector obtained by multiplying u by the matrix D is the discrete approximation for the derivative $\frac{du}{dy} \equiv D_1 u$.
b) $D(Du) = D^2u$ is the discrete approximation for $\frac{d^2u}{dy^2} \equiv D_2 u$.
c) $D(D(Du)) = D^3u$ is the discrete approximation for $\frac{d^3u}{dy^3} \equiv D_3 u$.
d) $D\left[D(D(Du))\right] = D^4u$ is the discrete approximation for $\frac{d^4u}{dy^4} \equiv D_4 u$.
The discretized stability equations are transformed into a generalized eigenvalue problem:

$$\mathbf{A\Phi} = \omega \mathbf{B\Phi}. \tag{3.42}$$

where

$$\mathbf{A} = \begin{bmatrix} A_{11} & A_{12} \\ A_{21} & A_{22} \end{bmatrix}, \quad \mathbf{B} = \begin{bmatrix} B_{11} & 0 \\ 0 & B_{22} \end{bmatrix}, \quad \mathbf{\Phi} = \begin{bmatrix} \phi \\ s \end{bmatrix}.$$

and

$$A_{11} = \frac{i}{G^*}\left(\phi'''' - 2\alpha^2\phi'' + \alpha^4\phi\right) + \alpha\left[f'\left(\phi'' - \alpha^2\phi\right) - f'''\phi\right], \tag{3.43}$$

$$A_{12} = \frac{i}{G^*}s', \tag{3.44}$$

$$A_{21} = -\alpha h'\phi, \tag{3.45}$$

$$A_{22} = \frac{i}{PG^*}\left(s'' - \alpha^2 s\right) + \alpha f' s, \tag{3.46}$$

$$B_{11} = \phi'' - \alpha^2\phi, \tag{3.47}$$

$$B_{22} = s. \tag{3.48}$$

The boundary conditions (asymmetric) are [1]

$$\phi'(-1) = \phi'''(-1) = s(-1) = 0, \quad \phi(1) = \phi'(1) = s(1) = 0. \tag{3.49}$$

These boundary conditions are implemented in (3.42) as follows:
1) First row of the matrix A_{11} is replaced by the first row of the matrix D_1 and the first row of the matrices A_{12} and B_{11} are replaced by zeros.
2) Second row of the matrix A_{11} is replaced by the first row of the matrix D_3 and the second row of the matrices A_{12} and B_{11} are replaced by zeros.
3) $N-1^{th}$ row of the matrix A_{11} is replaced by the N^{th} row of the matrix D_1 and the $N-1^{th}$ row of the matrices A_{12} and B_{11} are replaced by zeros.
4) N^{th} row of the matrix A_{11} is replaced by the N^{th} row of the matrix D_0 and the N^{th} row of the matrices A_{12} and B_{11} are replaced by zeros.
5) First row of the matrix A_{22} is replaced by the first row of the matrix D_0 and the first row of the matrices A_{21} and B_{22} are replaced by zeros.
6) N^{th} row of the matrix A_{22} is replaced by the N^{th} row of the matrix D_0 and the N^{th} row of the matrices A_{21} and B_{22} are replaced by zeros.

3.4.3 *Arnoldi's* Algorithm

The generalized eigenvalue problem, (3.39) or (3.42), can be solved for ω by specifying α and G^*. If we increase the grid points, the number of eigenvalues also increases and hence the computation time increases. In that case we can use *Arnoldi's Algorithm* with less number of grid points to refine an approximate value of the least stable eigenmode. The generalized eigenvalue problem $A\mathbf{X} = \lambda B\mathbf{X}$ in modified form is given below (Saad 2000; Nayar & Ortega 1993),

$$C\mathbf{X} = \mu X, \tag{3.50}$$

[1] Here the domain is transformed from $[0, \eta_{max}]$ to $[-1, 1]$. Corresponding base flow quantities are computed for the new domain.

where $C = (A - \lambda_0 B)^{-1} B$ and $\mu = 1/(\lambda - \lambda_0)$. For a guess value λ_0, we get an accurate value λ.
The Arnoldi's algorithm starts with an initial vector v_1 with $\| \mathbf{v_1} \|_2 = 1$ and computes additional vectors $\mathbf{v_2}, \ldots, \mathbf{v_m}$ from the following steps:

$$\hat{\mathbf{v}}_{\mathbf{j+1}} = C\mathbf{v_j} - \sum_{i=1}^{j} h_{ij}\mathbf{v_i} \tag{3.51}$$

$$h_{j+1,j} = \| \mathbf{v_{j+1}} \|_2 \tag{3.52}$$

$$\mathbf{v_{j+1}} = \hat{\mathbf{v}}_{\mathbf{j+1}}/h_{j+1,j} \tag{3.53}$$

for $j = 1, \cdots, m-1$. The h_{ij} are the inner products $h_{ij} = (v_i, Cv_j)$ such that $\mathbf{v_{j+1}}$ is orthogonal to all previous $\mathbf{v_i}$. The h_{ij} define an $m \times m$ Hessenberg matrix $H = [h_{ij}]$ whose eigenvalues approximate those of C, especially those in the outer part of the spectra of C. Ideally, one chooses m sufficiently small so that the work in generating H and computing its eigenvalues by the QZ method is not excessive, but m needs to be sufficiently large so that the selected eigenvalues of C are approximated accurately.

3.5 Results on Temporal Stability

3.5.1 Code Validation

The QZ-algorithm of Matlab software is used to solve the eigenvalue problem. In table 3.1, the growth-rate (αc_i) and the phase speed ($c_r = \frac{\omega_r}{\alpha}$) are compared for a test case of $P = 0.7$, $\alpha = 0.5$, $G^* = 100$. This test case shows the effect of grid resolution ($N = 101$, 151, 201) for both finite difference and spectral methods. There is no significant difference; both the phase speed and the growth rate are matching to the third decimal place. Even though the spectral method (dense matrix computation) is more accurate, it's computational time is much higher compared to that for the finite difference method (sparse matrix computation). Figure 3.3 shows the neutral curves for $P = 0.7$ and 6.7, computed by spectral and finite difference methods with 151 grid points. The location of the neutral curve is same for both methods. The stability diagram for P=0.7 looks similar to that reported by Pera & Gebhart (1971). In figures 3.3(b) and 3.3(d) the zoomed regions at small G^* are

shown and the critical Grashof numbers are indicated.

The spectra in the (c_r, c_i)-plane are shown for $P = 0.7$ and 6.7, along with the effect of grid size, in figures 3.4 and 3.5. There is a three branch structure, and the unstable mode comes from the right branch as seen in figures 3.4 and 3.5.

	FD		Spectral		
	αc_i	c_r	αc_i	c_r	
$N = 101$	0.073136	0.243358	0.073236	0.243364	$N = 101$
$N = 151$	0.073196	0.243399	0.073239	0.243361	$N = 151$
$N = 201$	0.073217	0.243414	0.073242	0.243406	$N = 201$

Table 3.1: For $G^* = 100$, $\alpha = 0.5$ and $P = 0.7$, the least unstable mode computed by finite difference (FD) and spectral (Spectral) methods for different grid sizes (N), c_r is the phase speed and αc_i is the growth rate.

In table 3.2, the time taken for computing all eigenvalues by the QZ-algorithm and the Arnoldi algorithm are compared, and the corresponding least stable eigenmode is also shown. It is clear that the time taken by the Arnoldi algorithm is about half of that taken by the QZ-algorithm even with $N = 301$.

N	λ	t_{QZ}	λ	$t_{Arnoldi}$
51	0.121568+0.072806i	0.1119	0.1216+0.0728i	0.0592
101	0.121679+0.073136i	0.9255	0.1217+0.0731i	0.4598
301	0.121712+0.073233i	24.4826	0.1217+0.0732i	11.0341

Table 3.2: For $G^* = 100$, $\alpha = 0.5$, and $P = 0.7$: λ- least stable eigenvalue; t_{QZ}- time taken by the QZ algorithm in seconds; $t_{Arnoldi}$- time taken by the Arnoldi's algorithm in seconds; N is the number of grid points.

3.5.2 Results for various Prandtl Numbers

For a range of modified Grashof numbers G^* and wavenumbers α, the eigenvalues are calculated numerically for different Prandtl numbers $P = 0.7$, 6.7, 100, 200 and 500. The corresponding neutral curves with different amplification contours

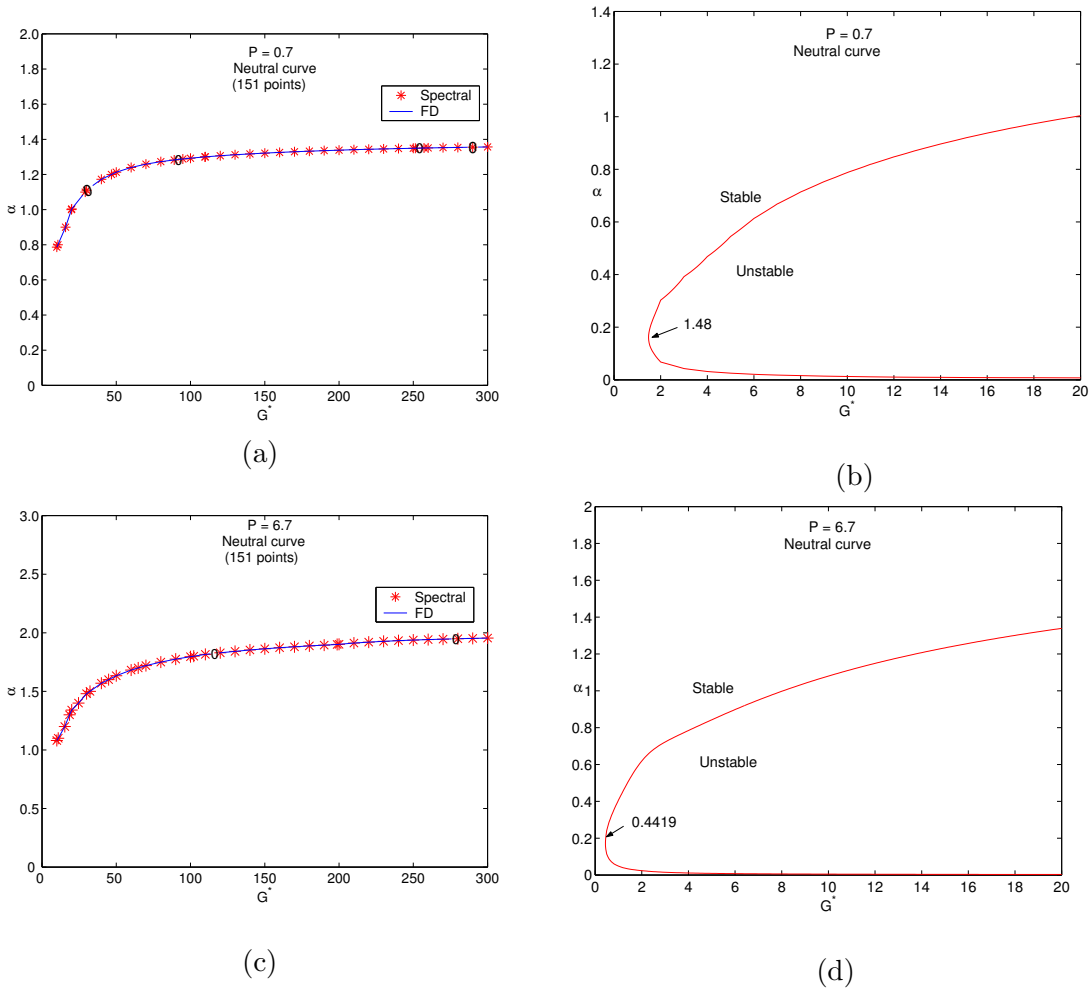

Figure 3.3: Neutral curves plotted in the $(\alpha - G^*)$-plane with parallel flow approximation, (a), (b) air $P = 0.7$; (c),(d) water $P = 6.7$. The solid line in each panel correspond to finite difference method (FD) and the star symbols correspond to spectral method. Critical Grashof numbers are indicated.

are shown in figures 3.6 - 3.10.

These stability plots are obtained by using both finite-diffence method and spectral collocation methods with 101 and 151 grid points. There is no significant difference in amplification rates obtained from these two methods using different grid sizes which shows the accuracy of the reported computations.

From the stability diagrams in figures 3.6(a)-3.10(a), it is clear that the upper branch of each neutral curve is well defined and has an asymptotic limit for α as

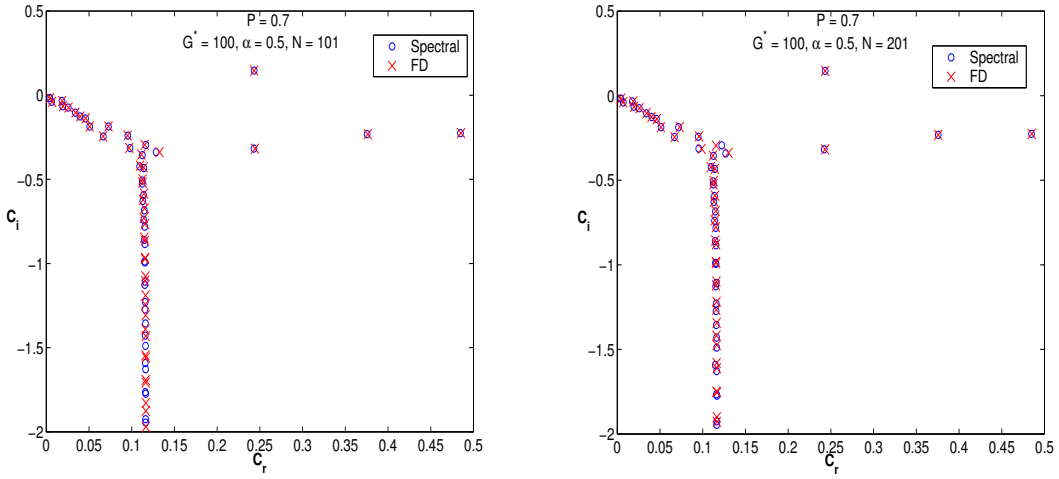

(a) (b)

Figure 3.4: Spectra for air: $P = 0.7$, $G^* = 100$, $\alpha = 0.5$; (a) $c_r - c_i$ with 101 grid points (b) $c_r - c_i$ with 201 grid points; here c_r is the phase speed and αc_i is the growth rate.

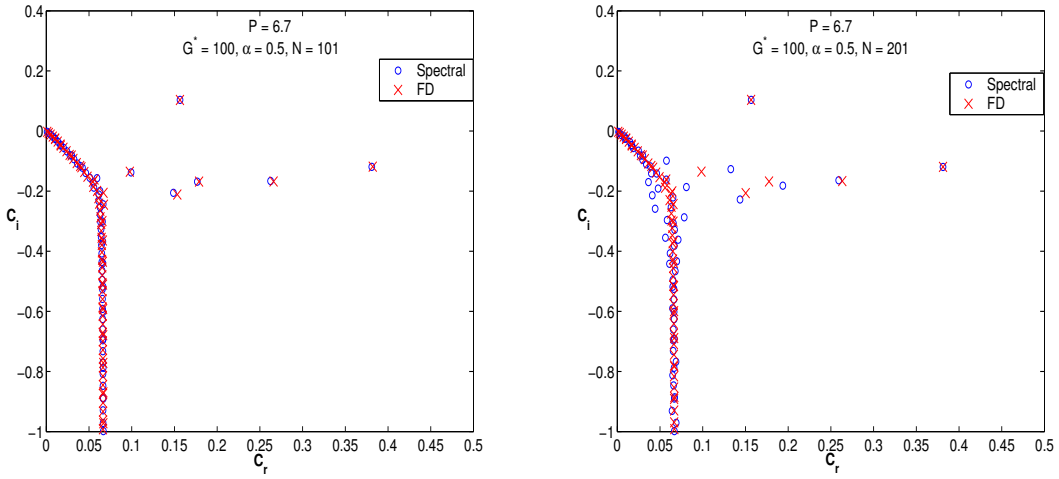

(a) (b)

Figure 3.5: Spectra for water: $P = 6.7$, $G^* = 100$, $\alpha = 0.5$; (a) $c_r - c_i$ with 101 grid points (b) $c_r - c_i$ with 201 grid points; here c_r is the phase speed and αc_i is the growth rate.

$G^* \to \infty$. This limit increases with increasing Prandtl number which suggests that the upper branch does not go to zero as G^* increases. Even in the limit $G^* \to \infty$, there exists a range of wavenumbers over which the flow is unstable.

At high Prandtl numbers $P \geq 100$ in figures 3.8-3.10, the neutral curve shows

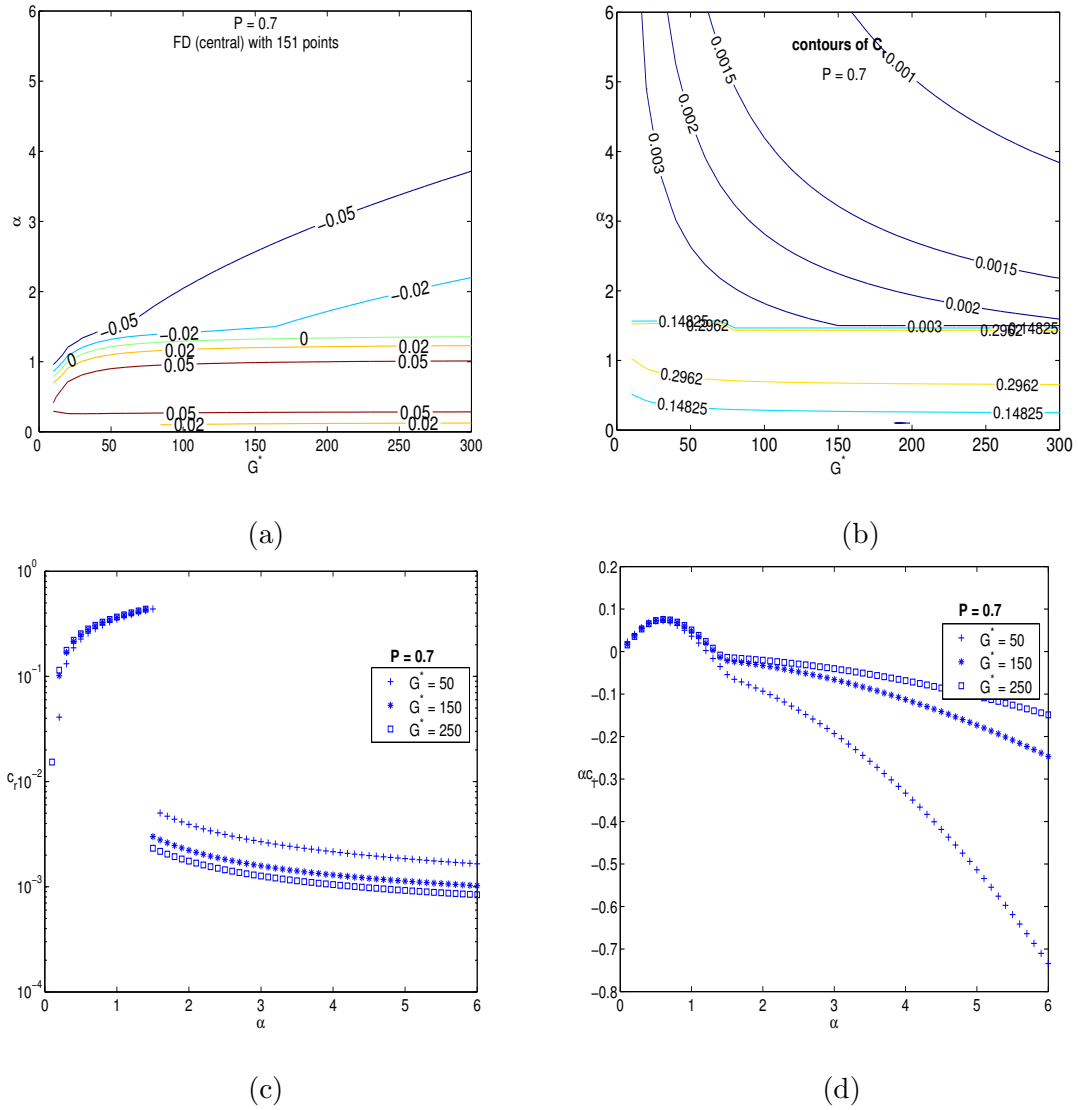

Figure 3.6: For air $P = 0.7$, (a) Amplification rates in the $(\alpha - G^*)$-plane with parallel flow approximation; (b) Contours of phase speed c_r; (c) Variation of phase speed, c_r, with α for three values of Grashof number $G^* = 50, 150, 250$; (d) Variation of growth rate, αc_i, with α for three values of Grashof number $G^* = 50, 150, 250$.

a kink and there is an additional unstable loop (see figure 3.9a for P=200) whose size increases with increasing Prandtl number. This additional loop is because of the mean temperature gradient $(h^{'})$ in the disturbance energy equation and the thermal energy term $(s^{'})$ in the disturbance momentum equation as we shall show below. The stability diagram at high Prandtl numbers shows the existence of multiple critical Grashof numbers (the point where the stable and unstable

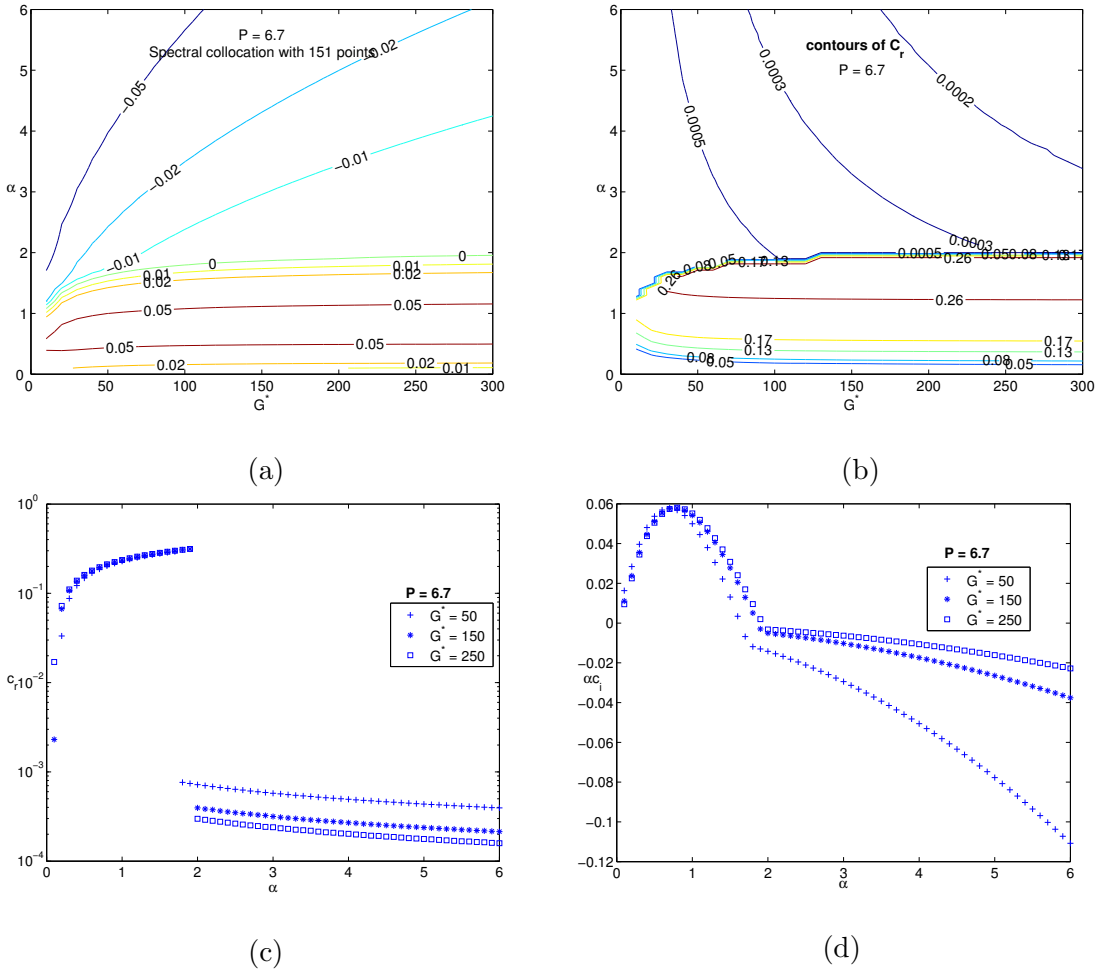

Figure 3.7: For water $P = 6.7$, (a) Amplification rates in the $(\alpha - G^*)$-plane with parallel flow approximation; (b) Contours of phase speed c_r; (c) Variation of phase speed, c_r, with α for three values of Grashof number $G^* = 50, 150, 250$; (d) Variation of growth rate, αc_i, with α for three values of Grashof number $G^* = 50, 150, 250$.

regions are seperated for a given wavenumber α and a Grashof number G^*) in the $(\alpha - G^*)$-plane. The upper branch is well defined, it has two limits: one limit for low Grashof numbers and another limit for high Grashof numbers. The existence of a lower branch has been found. Since the neutral curve is passing very close to the origin, the issues related to the minimum critical Grashof number may not be correct (the parallel flow assumption ceases to hold, see section 4.4 in chapter 4).

From c_r-α plots in figures 3.6(c)-3.10(c) at any Prandtl number, we can conclude that in the stable region the least stable mode has almost zero speed (but not a stationary wave) and in the unstable region it has a finite magnitude. This

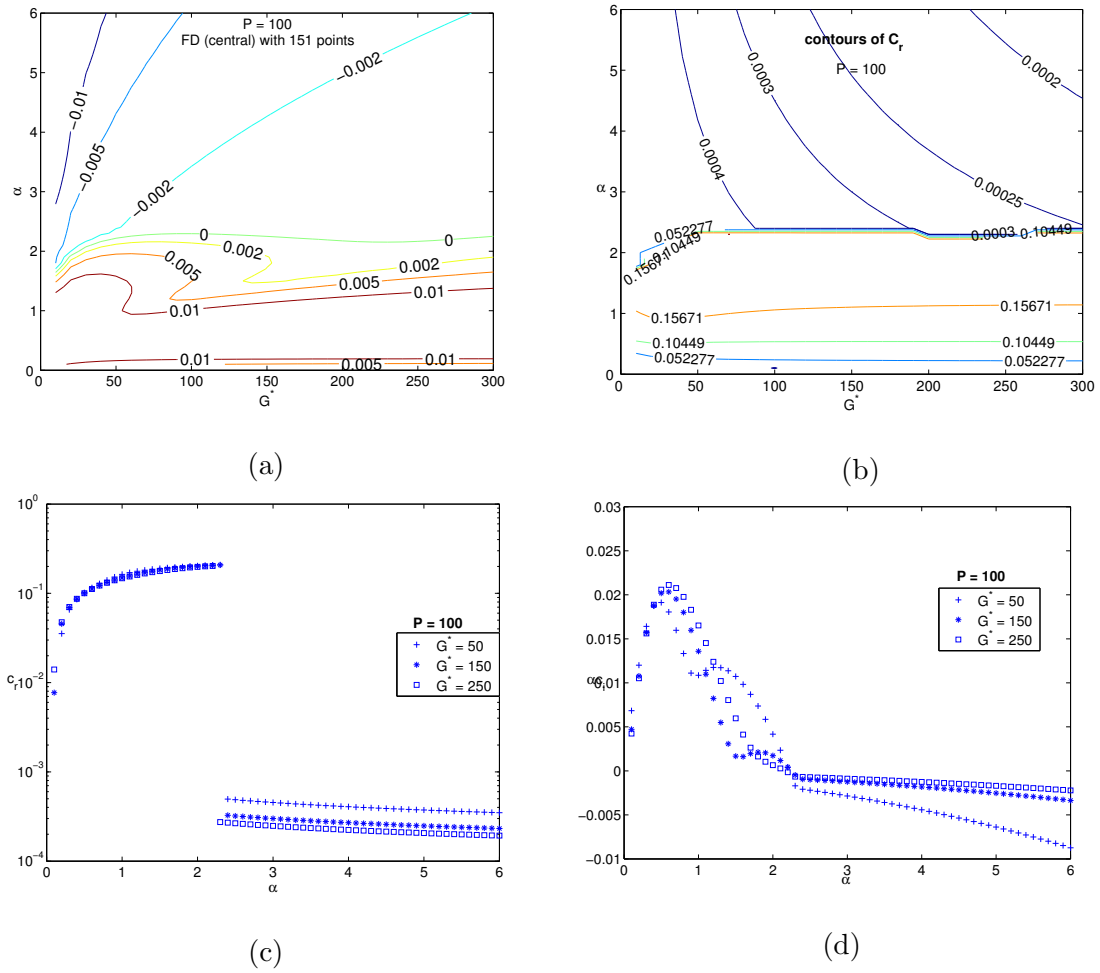

Figure 3.8: For $P = 100$, (a) Amplification rates in the $(\alpha - G^*)$-plane with parallel flow approximation; (b) Contours of phase speed c_r; (c) Variation of phase speed, c_r, with α for three values of Grashof number $G^* = 50, 150, 250$; (d) Variation of growth rate, αc_i, with α for three values of Grashof number $G^* = 50, 150, 250$.

finite phase speed is almost constant for any Grashof number G^* at a given Prandtl number P. Also, the maximum phase speed decreases as the Prandtl number is increasing which implies that the unstable mode is shifting towards the edge of the boundary-layer.

Comparing the growth-rate curves in figures 3.6(d)-3.10(d), we find that the growth rate of the least-stable mode decreases with increasing Prandtl number for a given G^*. Comparing the unstable zones in figures 3.6(a)-3.10(a), we find that the size of the unstable zone in the (α, G^*)- plane increases with increasing P.

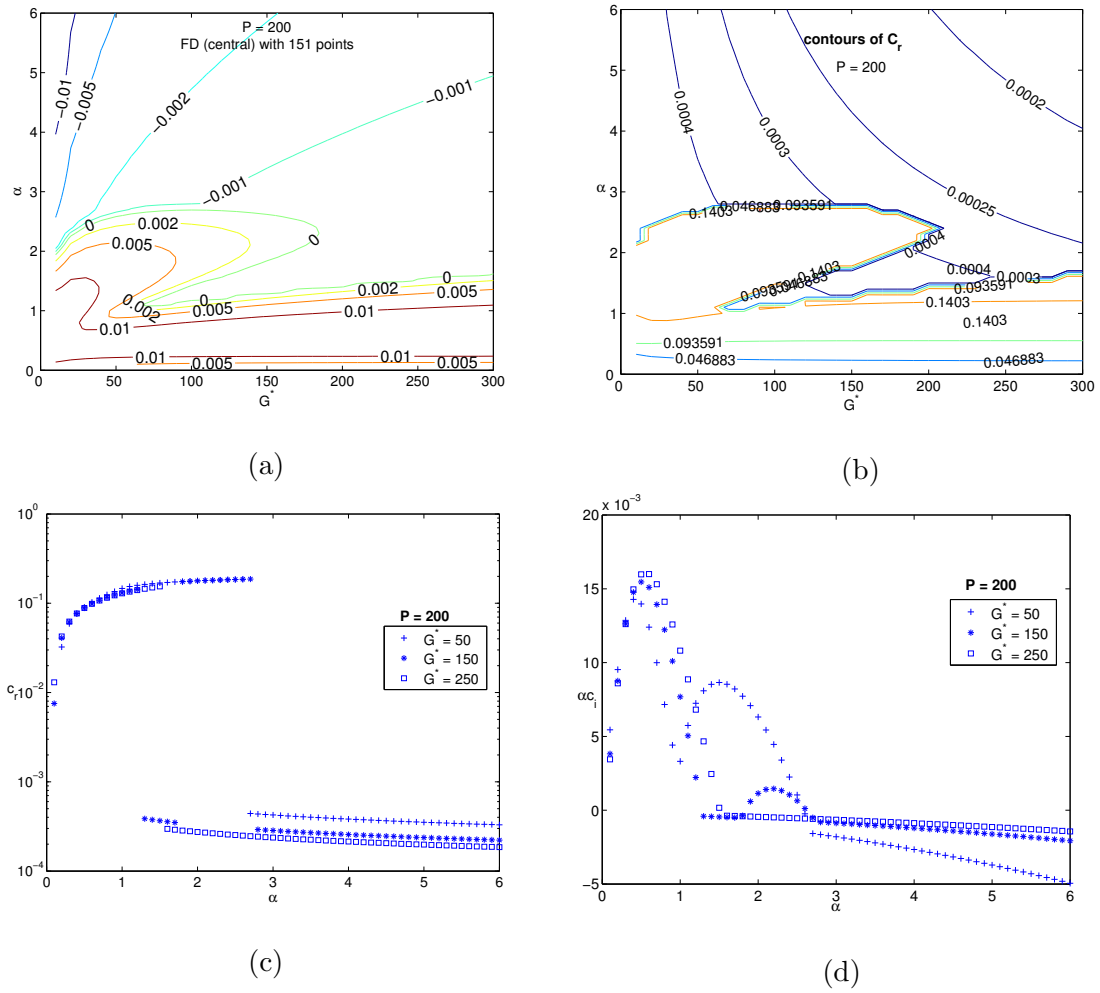

Figure 3.9: For $P = 200$, (a) Amplification rates in the $(\alpha - G^*)$-plane with parallel flow approximation; (b) Contours of phase speed c_r; (c) Variation of phase speed, c_r, with α for three values of Grashof number $G^* = 50, 150, 250$; (d) Variation of growth rate, αc_i, with α for three values of Grashof number $G^* = 50, 150, 250$.

3.5.3 Results for uncoupled disturbance equations

Here we present results for this stability problem by assuming that the velocity and the temperature perturbations are uncoupled from each other. The stability

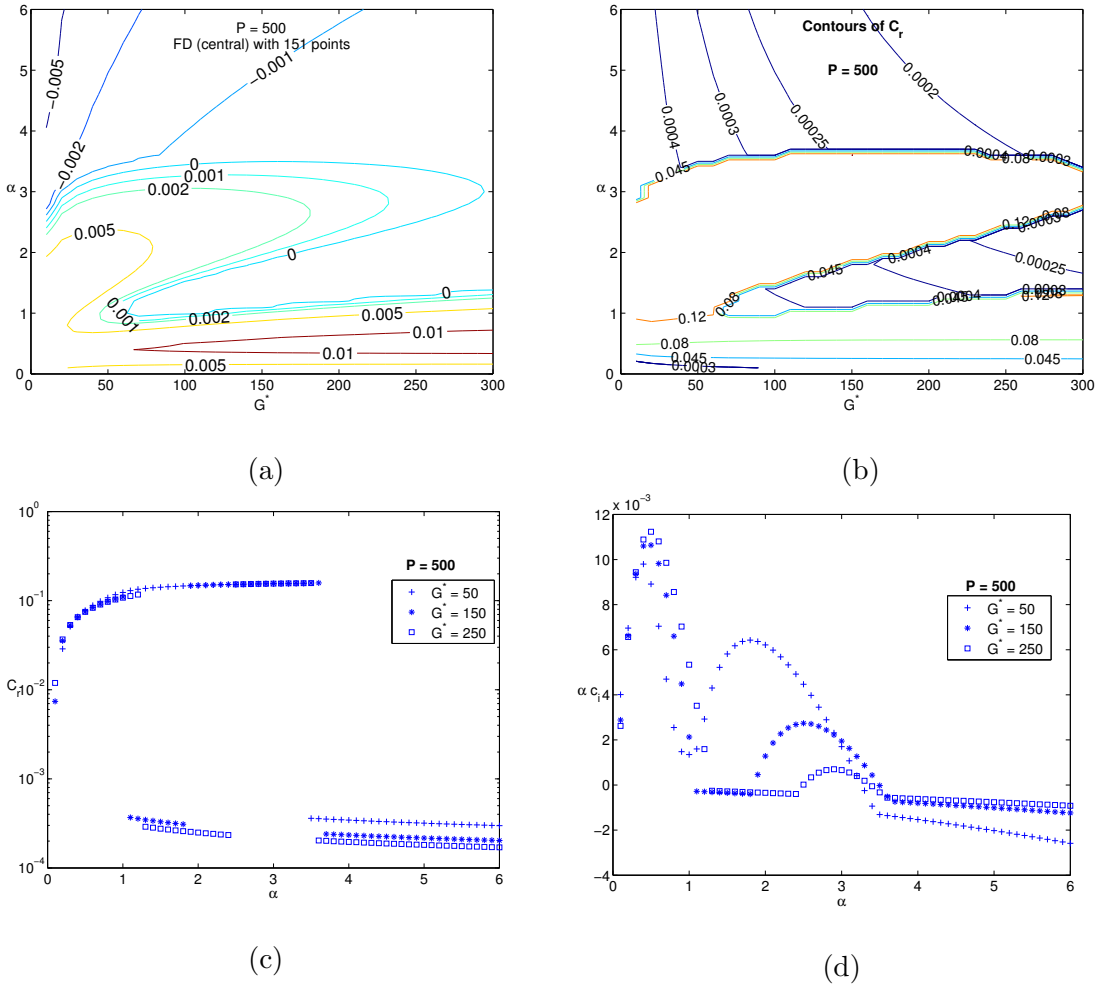

Figure 3.10: For $P = 500$, (a) Amplification rates in the $(\alpha - G^*)$-plane with parallel flow approximation; (b) Contours of phase speed c_r; (c) Variation of phase speed, c_r, with α for three values of Grashof number $G^* = 50, 150, 250$; (d) Variation of growth rate, αc_i, with α for three values of Grashof number $G^* = 50, 150, 250$.

equations,

$$\phi'''' - 2\alpha^2\phi'' + \alpha^4\phi + \overbrace{s'}^{dropping} = i\alpha G^* \left[\left(f' - \frac{\omega}{\alpha}\right)\left(\phi'' - \alpha^2\phi\right) - f'''\phi\right], \tag{3.54}$$

$$s'' - \alpha^2 s = i\alpha P G^* \left[\left(f' - \frac{\omega}{\alpha}\right) s - \underbrace{h'\phi}_{dropping}\right], \tag{3.55}$$

can be made independent (uncoupled) by dropping $s^{'}$ and $h^{'}\phi$ from (3.54) and (3.55) equations, respectively. For the uncoupled equations, the momentum and energy disturbance equations can be solved independently.

The neutral curves are computed for Prandtl numbers $P = 0.7$ to 10000 as shown in figure 3.11(a). For the uncoupled case, the least stable mode belongs to the momentum equation (purely hydrodynamic, (3.54)), and the energy equation (3.55) always results stable modes. Previous (Pera & Gebhart 1971) and present computations show the existance of a lower branch and a minimum critical Grashof number for any Prandtl number. It is observed that the critical Grashof number G^*_{cr} increases with increasing Prandtl number P, and the size of the unstable zone in the (G^*, α)- plane decreases in the same limit. The critical Grashof number (G^*_{cr}) varies with the Prandtl number P as a power-law,

$$G^*_{cr} \quad \sim \quad P^{0.2375}, \tag{3.56}$$

as it is evident from figure 3.11(b). The critical wavenumber (α_{cr}) varies between 0.32 - 0.36 at low Prandtl numbers $(P = 0.7 - 100)$ and reaches a constant value 0.3 at high Prandtl numbers $(P \geq 1000)$ as seen in figure 3.11(c).

These computations indicate that the solution of the uncoupled disturbance equations gives incorrect results at high Prandtl numbers (since $h^{'}$ in the energy disturbance equation increases with Prandtl number as $\sqrt{P}$ and hence cannot be neglected), and the region of instability is large in the case of coupled equations (see figure 3.12). It is clear from figure 3.12 that the coupling terms in the stability equations (3.54-3.55) are responsible for the additional unstable-loop at high Prandtl numbers, see figure 3.12(c) and 3.12(d).

3.5.4 Eigenfunctions for unstable modes

For the disturbance equations (3.26-3.27) with the boundary conditions (3.28), the eigenfunctions are computed at various Prandtl numbers (figures 3.14-3.17). These eigenfunctions are in complex form,

$$\phi = \mathcal{R}(\phi) + i\mathcal{I}(\phi), \quad s = \mathcal{R}(s) + i\mathcal{I}(s), \tag{3.57}$$

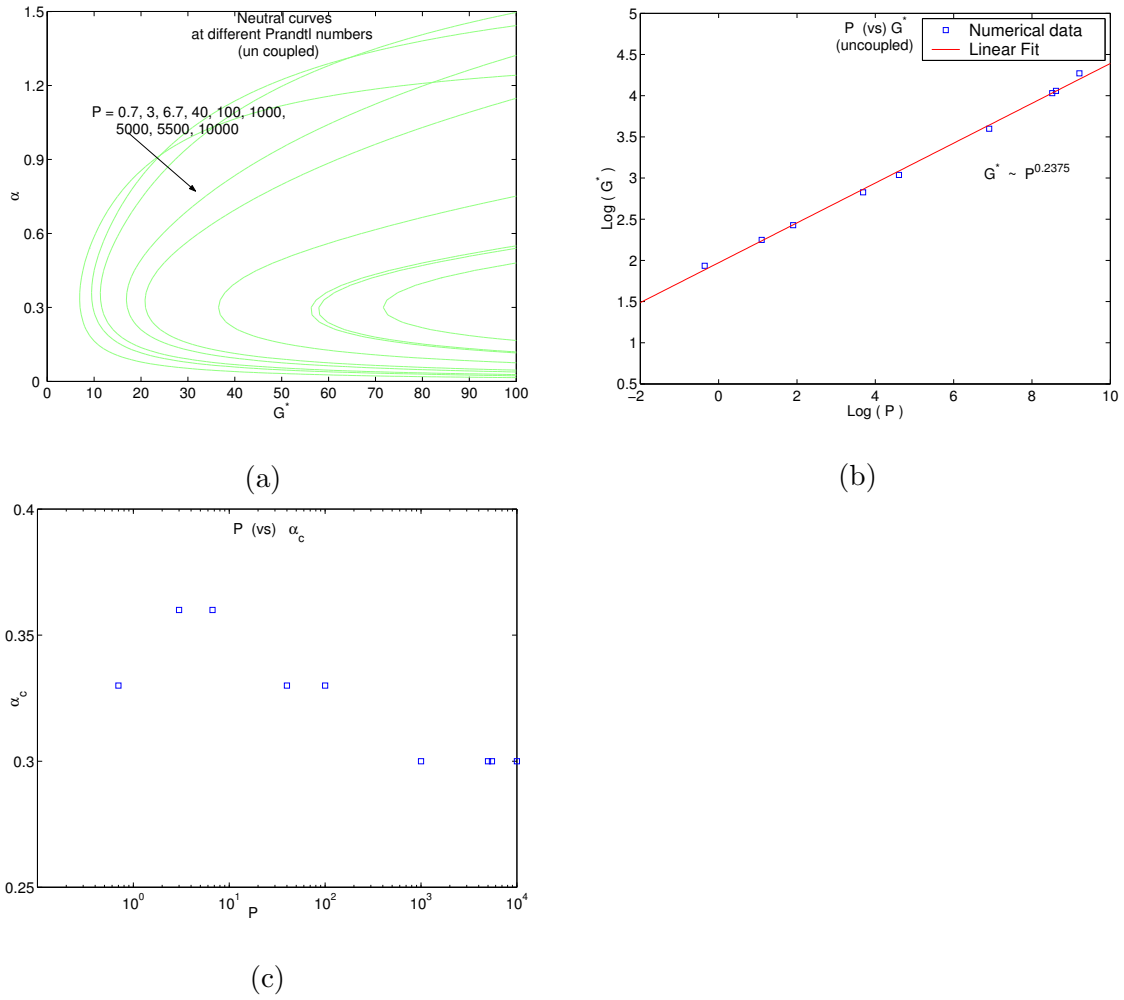

Figure 3.11: For uncoupled equations: (a) neutral curves at different Prandtl numbers; (b) log-log plot for critical Grashof number G^*_{cr} and Prandtl number P; (c) semi-log plot of $\alpha_{cr} - P$.

where $\mathcal{R}$ represents the real part and $\mathcal{I}$ represents the imaginary part. Figures 3.13-3.14 show the eigenfunctions for $P = 0.7$ and 6.7 at $G^* = 100$, $\alpha = 0.5$. In these figures, the solid line represents the real part and the dashed line represents the imaginary part of eigenfunctions. Figures 3.15-3.16 show the eigenfunctions for $P = 200$. At high P, the thermal disturbance is localized within the thermal boundary layer. The overall structure of both velocity and temperature eigenfunctions looks similar at different Prandtl numbers.

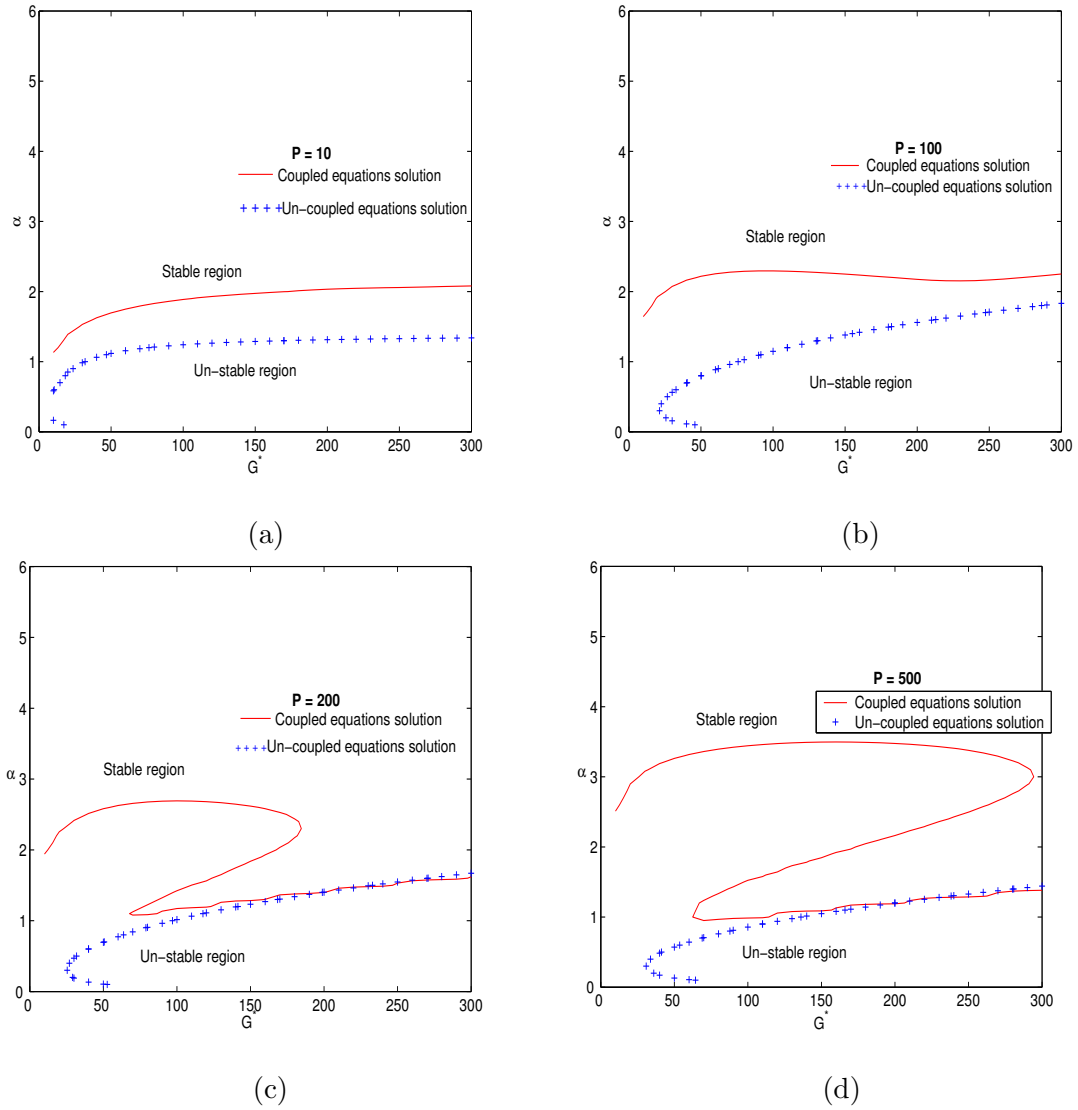

Figure 3.12: Comparison between neutral curves for coupled and uncoupled disturbance equations for (a)$P = 10$; (b)$P = 100$; (c)$P = 200$; (d)$P = 500$.

3.5.5 Energy Balance of Disturbance Motion

Here we derive the evolution equations for the disturbance kinetic energy and thermal energy (Natchtsheim 1963; Gill & Davey 1969). The energy integral is obtained from (3.26-3.27) by multiplying the complex conjugates ϕ^* and s^* and integrating from $\eta = 0$ to $\eta = \infty$. The resulting equations (by taking the real part)

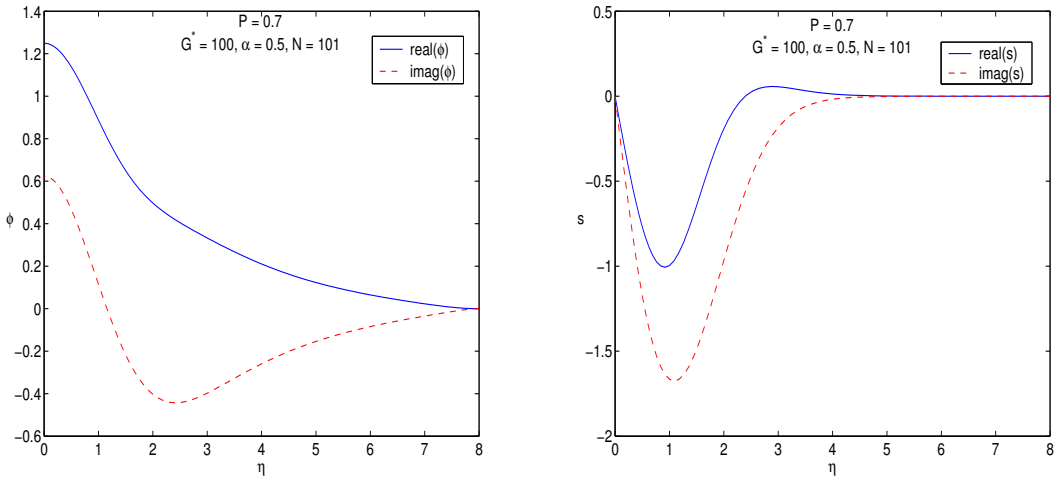

(a) (b)

Figure 3.13: Eigenfunctions for $P = 0.7$ (air), $G^* = 100$. (a) Stream function; (b) temperature.

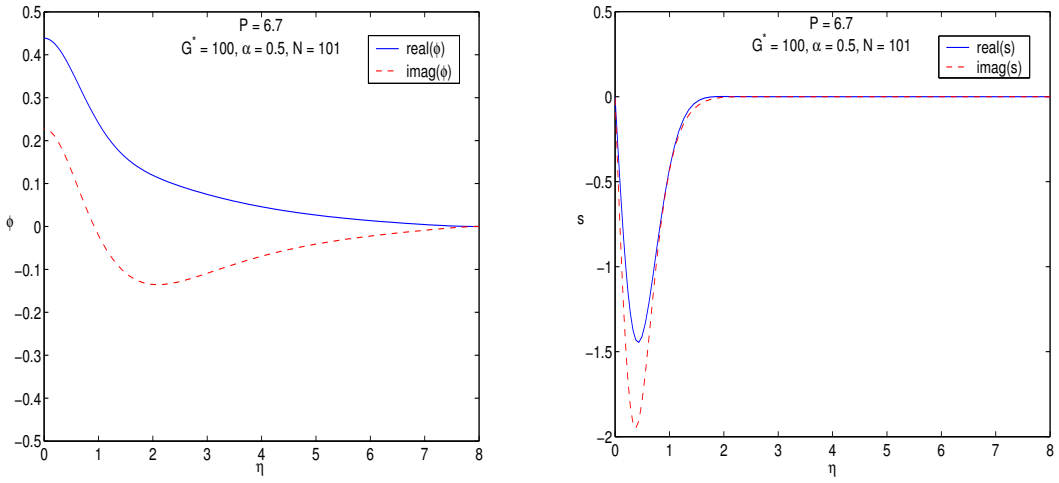

(a) (b)

Figure 3.14: Eigenfunctions for $P = 6.7$ (water), $G^* = 100$. (a) Stream function; (b) temperature.

are

$$KE = VD + M_{dist} + buoy, \tag{3.58}$$

$$E_T = TD + T_{dist}, \tag{3.59}$$

where

$$KE = \alpha G^* c_i \int_0^\infty \left(\mid \phi \mid^2 + \alpha^2 \mid \phi \mid^2 \right) d\eta, \tag{3.60}$$

$$VD = \int_0^\infty \mid \phi'' - \alpha^2 \phi \mid^2 d\eta, \tag{3.61}$$

$$M_{dist} = \alpha G^* \int_0^\infty f'' \left(\phi_r \phi_i' - \phi_r' \phi_i \right) d\eta, \tag{3.62}$$

$$buoy = \int_0^\infty \left(s_r \phi_r' + s_i \phi_i' \right) d\eta, \tag{3.63}$$

$$E_T = \alpha P G^* c_i \int_0^\infty \mid s \mid^2 d\eta, \tag{3.64}$$

$$TD = -\int_0^\infty \left(\mid s' \mid^2 + \alpha^2 \mid s \mid^2 \right) d\eta, \tag{3.65}$$

$$T_{dist} = \alpha P G^* \int_0^\infty h' \left(\phi_r s_i - \phi_i s_r \right) d\eta. \tag{3.66}$$

and the suffixes r and i denote the real and imaginary parts respectively. KE is interpreted as the rate of change of disturbance kinitic energy, VD as the rate of viscous dissipation, M_{dist} as the rate of kinetic energy transfer from mean flow to the disturbance and *buoy* as the rate of kinetic energy gained through the buoyancy force. For thermal energy fluctuations, E_T is the rate of disturbance potential energy, TD is the rate of thermal energy dissipation, T_{dist} is the rate of disturbance potential energy gained from mean temperature field. Adding (3.58) and (3.59) equations gives the total disturbance energy equation

$$KE + E_T = (VD + TD) + M_{dist} + buoy + T_{dist}. \tag{3.67}$$

The energy distributions are shown in figures 3.17-3.22, where the locations of the critical layers are also shown.

For $P = 0.7$, at high wavenumbers (see figure 3.17) the energy gained by the disturbance mainly comes from the Reynold's stress term (M_{dist}) and a small amount is contributed from the disturbance buoyancy force term (*buoy*). The maximum amount of disturbance energy is dissipated at the center line ($\eta = 0$) by viscous forces (VD). At $\eta \simeq 1$, the rate of disturbance potential energy gained from

the mean temperature (T_{dist}) is maximum; thermal dissipation (TD) is maximum around the critical layer. There is no change in the rate of gain of the disturbance kinetic energy (KE) since the disturbance is neutral ($c_i = 0$). The amount of energy produced by the Reynolds stress and the buoynacy forces is balanced by viscous forces.

From $P = 6.7$ onwards we clearly see that at high wavenumbers (see figures 3.18-3.22) the rate of gain of kinetic energy by Reynolds stress becomes smaller. With increasing P, the kinetic energy gained by disturbances is due to the buoyancy forces, and the shear production (Reynold's stress) term is small. The maximum value of this energy is located far away from the critical layer, and it's location is shifting towards the center line ($\eta = 0$) as the Prandtl number is increased. At high Prandtl numbers, the contribution from the Reynold's stress terms is almost zero compared to the gain in energy by the buoyancy force. The viscous dissipation and thermal energy curves have similar shapes at high Prandtl numbers.

The above energy analysis suggests that the buoyancy force is the main source of disturbance energy at high Prandtl numbers. Therefore, the additional instability loop at high P can aptly be termed as the "buoyancy-driven" instability mode.

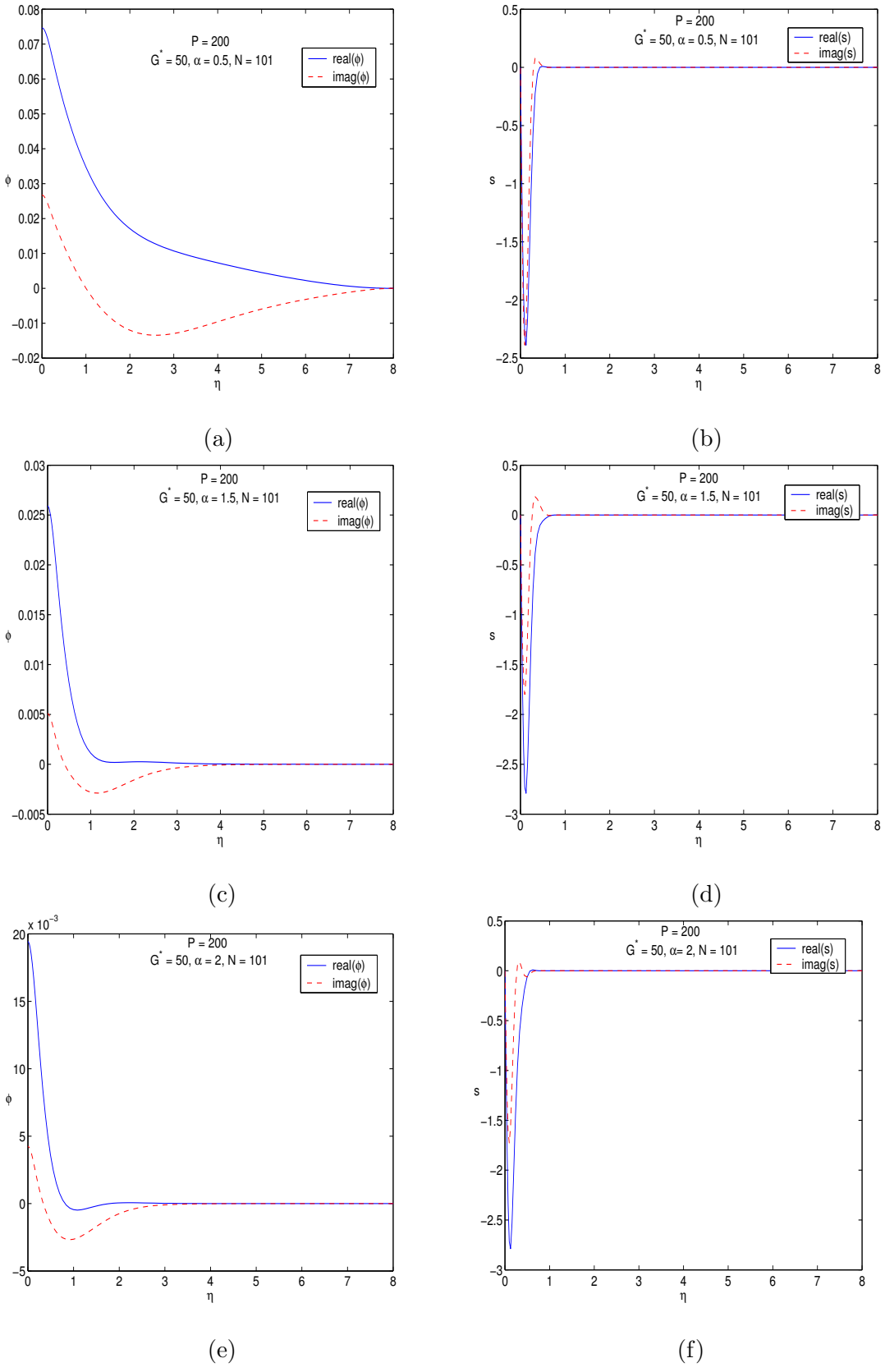

Figure 3.15: Eigenfunctions for $P = 200$, $G^* = 50$. (a), (c), (e) are stream function; (b), (d), (f) are temperature.

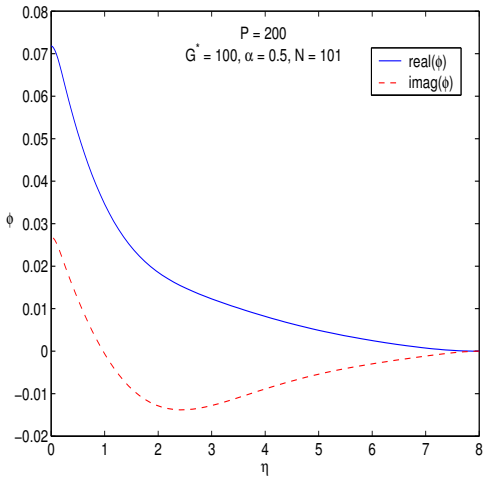

(a)

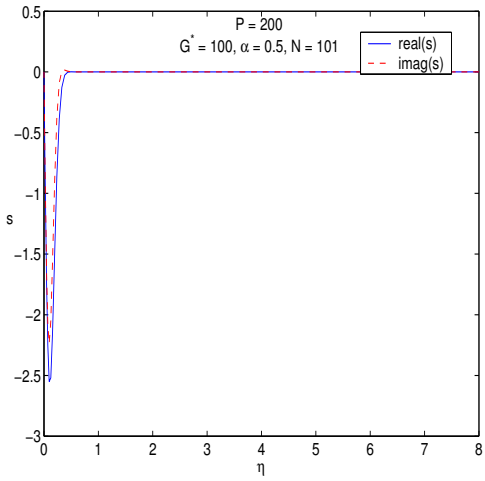

(b)

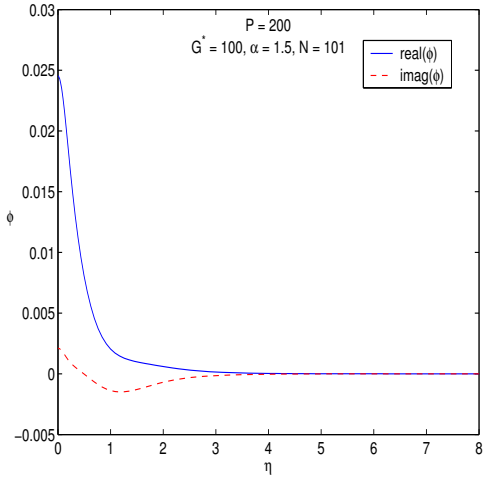

(c)

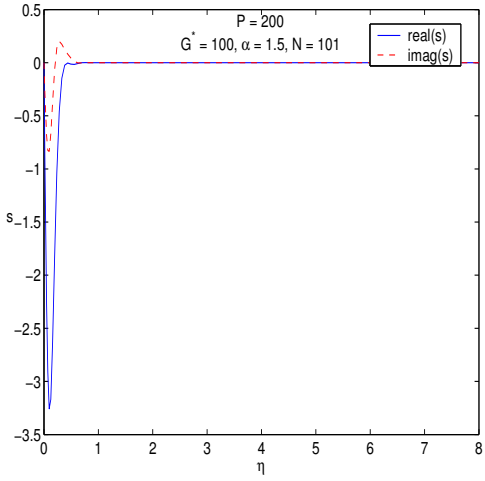

(d)

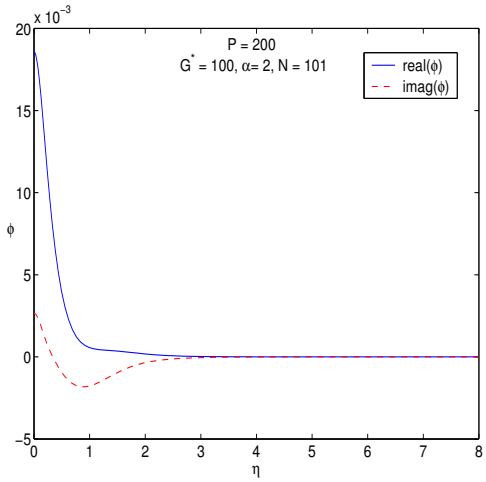

(e)

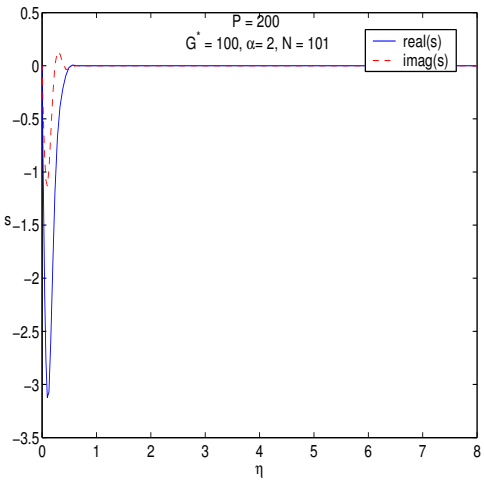

(f)

Figure 3.16: Eigenfunctions for $P = 200$, $G^* = 100$. (a), (c), (e) are stream function; (b), (d), (f) are temperature.

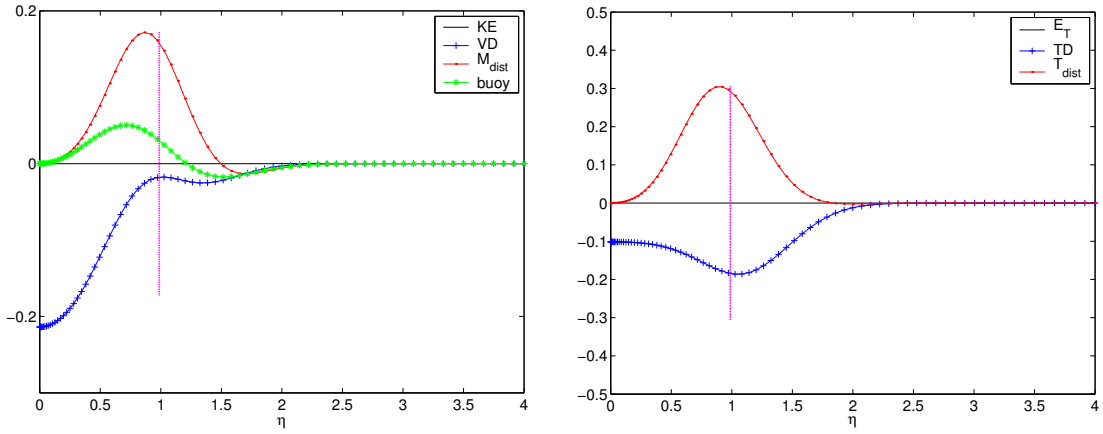

(a) (b)

Figure 3.17: Energy distribution for P=0.7 (air), $G^* = 100$, $\alpha = 1.293$; (a) kinetic energy (b) thermal energy. Vertical lines indicate the location of critical layer.

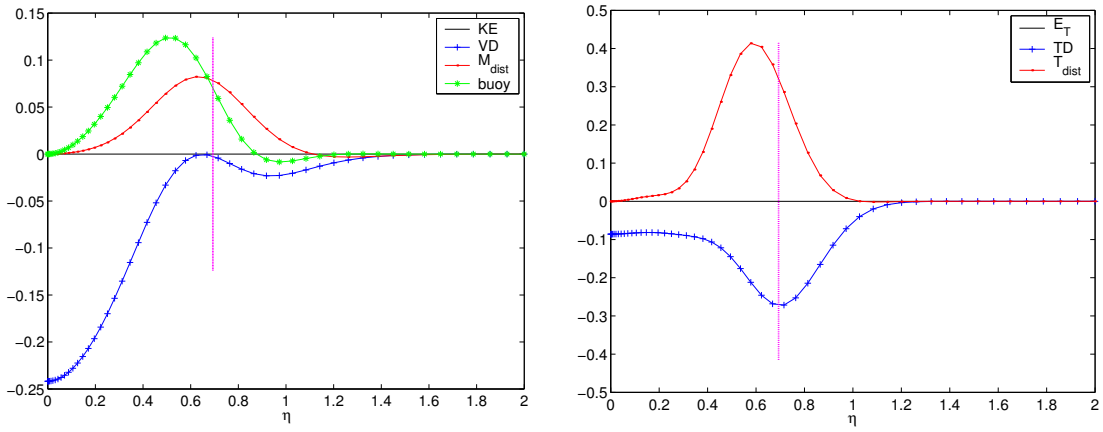

(a) (b)

Figure 3.18: Energy distribution for P=6.7 (water), $G^* = 100$, $\alpha = 1.796$; (a) kinetic energy (b) thermal energy. Vertical lines indicate the location of critical layer.

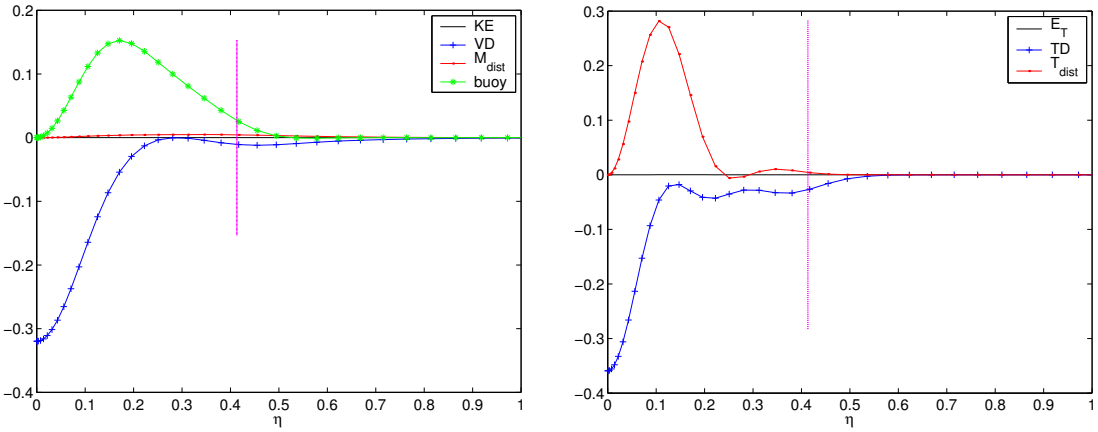

(a) (b)

Figure 3.19: Energy distribution for P=100.0, $G^* = 100$, $\alpha = 2.315$; (a) kinetic energy (b) thermal energy. Vertical lines indicate the location of critical layer.

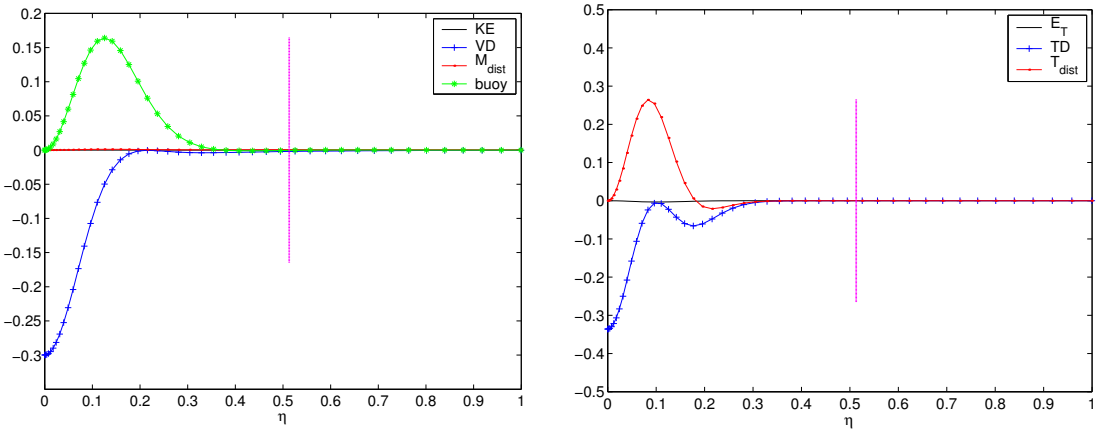

(a) (b)

Figure 3.20: Energy distribution for P=200.0 (water), $G^* = 100$, $\alpha = 1.395$; (a) kinetic energy (b) thermal energy. Vertical lines indicate the location of critical layer.

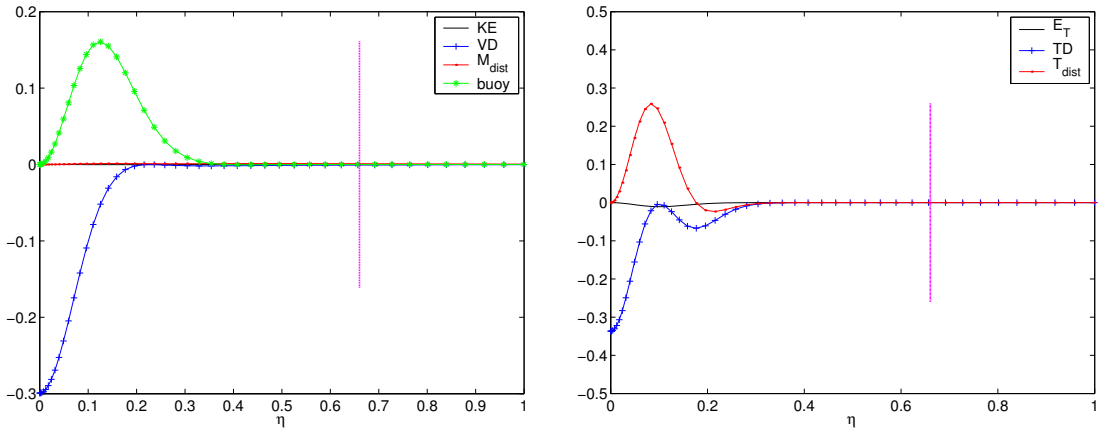

(a) (b)

Figure 3.21: Energy distribution for P=200.0, $G^* = 100$, $\alpha = 1.17$; (a) kinetic energy (b) thermal energy. Vertical lines indicate the location of critical layer.

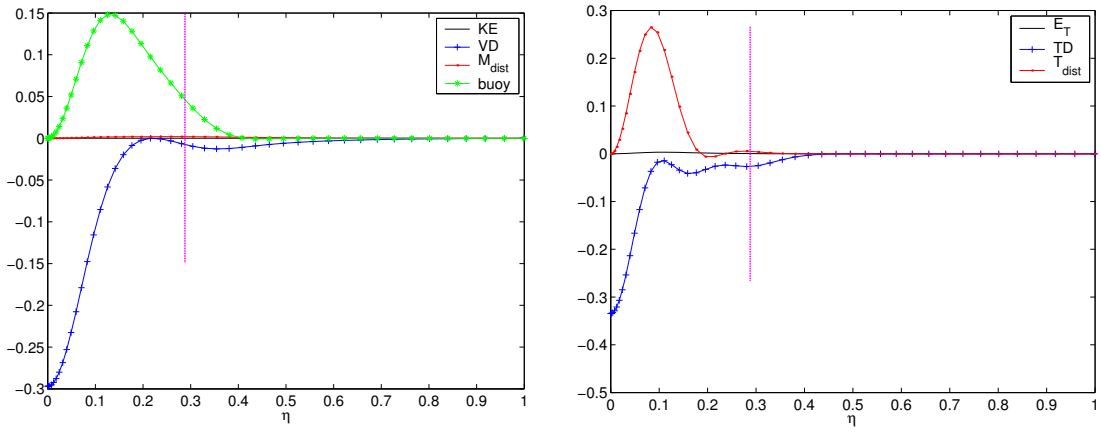

(a) (b)

Figure 3.22: Energy distribution for P=200.0, $G^* = 100$, $\alpha = 2.76$; (a) kinetic energy (b) thermal energy. Vertical lines indicate the location of critical layer.

CHAPTER 4

SPATIAL STABILITY AND NON-PARALLEL EFFECTS

4.1 Formulation of Spatial Eigenvalue Problem

For the spatial stability analysis, the disturbances are allowed to grow or decay in space:

$$\Phi(x, y, \tilde{\tau}) = \Phi(y) e^{i(\alpha x - \omega \tilde{\tau})},$$

where the wavenumber, $\alpha = \alpha_r + i\alpha_i$, is complex and the frequency, ω, is real. The disturbance grows or decays in space if $\alpha_i < 0$ or $\alpha_i > 0$, respectively.

The spatial eigenvalue problem can be written as a scalar polynomial form in $'\alpha'$,

$$\sum_{i=0}^{k} \alpha^{k-i} L_i \Phi = 0 \equiv D_k(\alpha)\Phi, \tag{4.1}$$

where L_i are linear differential operators, Φ is a complex variable and the parameter α is an eigenvalue. The solution of the above equation for $k = 1$ results in a generalized eigenvalue problem,

$$\alpha L_0 + L_1 = 0,$$

for which two matrices may be formed from the discretization of the operators L_0 and L_1. When k is greater than one, the problem is nonlinear in the parameter α, which is the case for the spatial stability problem. Since the wavenumber (α) to be computed in the linear stability equations is nonlinear, we cannot use the solution technique of temporal eigenvalue problem directly.

Most previous solution techniques for the nonlinear eigenvalue problem have used local iterations to determine an eigenvalue. A commonly used method is the

shooting method in which a first guess is made for the eigenvalue and the integration is performed over the whole domain (Gaster 1974, Garg 1981). This is repeated untill the boundary conditions at the end of the domain match the computed solution. The difficulty with such local methods is that a good first guess is needed to assure convergence. This difficulty can be resolved by using global methods.

The above nonlinear eigenvalue problem (4.1) can be made linear in wavenumber (α) by using the companion matrix method (Bridges & Morris 1984, Malik 1990). The approximate solution of this equation requires two steps. First, the operators L_k are converted to matrices. So, a discretization is required which yields the most accurate solution for the minimum order of the matrix. In the second step, the resulting nonlinear eigenvalue problem is linearized by formulating the companion matrix.

4.2 Companion Matrix Method

In linear algebra, the matrix $D_k(\alpha)$ in equation (4.1) is called a lambda matrix of degree k, which may be expressed as a scalar polynomial with matrix coefficients,

$$D_k(\alpha) = C_0\alpha^k + C_1\alpha^{k-1} + ... + C_{k-1}\alpha + C_k$$

where $C_0, C_1, ..., C_k$ are square matrices, with complex elements. The eigenvalues are the roots of the latent equation $det\,[D_k(\alpha)] = 0$, which is a scalar polynomial equation.

The companion matrix is a linearization of the lambda matrix. For a lambda matrix of degree k, the order of the companion matrix is $k \times$ order of C_k. Let us consider the following scalar polynomial of order four (Bridges & Morris 1984):

$$D_4(\alpha) = C_0\alpha^4 + C_1\alpha^3 + C_2\alpha^2 + C_3\alpha + C_4.$$

For this, the companion matrix may be formed to obtain a generalized eigenvalue

problem:

$$\left\{ \begin{bmatrix} -C_1 & -C_2 & -C_3 & -C_4 \\ I & 0 & 0 & 0 \\ 0 & I & 0 & 0 \\ 0 & 0 & I & 0 \end{bmatrix} - \alpha \begin{bmatrix} C_0 & 0 & 0 & 0 \\ 0 & I & 0 & 0 \\ 0 & 0 & I & 0 \\ 0 & 0 & 0 & I \end{bmatrix} \right\} \begin{Bmatrix} \alpha^3 \mathbf{a} \\ \alpha^2 \mathbf{a} \\ \alpha \mathbf{a} \\ \mathbf{a} \end{Bmatrix} = \begin{Bmatrix} 0 \end{Bmatrix}$$

where $\mathbf{a}$ is the right eigenvector of $D_4(\alpha)$ and I is a unit matrix.

For the plane thermal plume, the linear stability equations can be written in a scalar polynomial form in terms of wavenumber (α):

$$\begin{aligned} \alpha^4\phi + \alpha^3(iG^* f_0^{'}\phi) + \alpha^2(-iG^*\omega\phi - 2\phi^{''}) + \alpha(-iG^* f_0^{'}\phi^{''} + iG^* f_0^{'''}\phi) + (\phi^{''''} + iG^*\omega\phi^{''}) + s^{'} &= 0, \\ \alpha^2 s + \alpha(iPG^* f_0^{'} s - iPG^* h_0^{'}\phi) + (-s^{''} - iPG^*\omega s) &= 0. \end{aligned}$$

These equations can be written in the companion matrix form:

$$\mathcal{A}\mathcal{X} = \alpha\mathcal{B}\mathcal{X}, \tag{4.2}$$

where,

$$\mathcal{A} = \begin{bmatrix} -iGf_0^{'}I & iG\omega I + 2D^2 & iGf_0^{'}D^2 - iGf_0^{'''}I & -(D^4 + iG\omega D^2) & 0 & -D \\ I & 0 & 0 & 0 & 0 & 0 \\ 0 & I & 0 & 0 & 0 & 0 \\ 0 & 0 & I & 0 & 0 & 0 \\ 0 & 0 & iPGh_0^{'}I & 0 & -iPGf_0^{'}I & D^2 + iPG\omega I \\ 0 & 0 & 0 & 0 & I & 0 \end{bmatrix},$$

$$\mathcal{B} = \begin{bmatrix} I & 0 & 0 & 0 & 0 & 0 \\ 0 & I & 0 & 0 & 0 & 0 \\ 0 & 0 & I & 0 & 0 & 0 \\ 0 & 0 & 0 & I & 0 & 0 \\ 0 & 0 & 0 & 0 & I & 0 \\ 0 & 0 & 0 & 0 & 0 & I \end{bmatrix}, \qquad \mathcal{X} = \begin{Bmatrix} \alpha^3\phi \\ \alpha^2\phi \\ \alpha\phi \\ \phi \\ \alpha s \\ s \end{Bmatrix}.$$

The boundary conditions are

$$\phi^{'}(-1) = \phi^{'''}(-1) = s(-1) = 0, \qquad \phi(1) = \phi^{'}(1) = s(1) = 0. \tag{4.3}$$

In the companion matrix (4.2), each row (R) and column (L) consists of $N \times N$ sub-matrices. Here, R and L represent the position of a sub-matrix in the companion matrix. The rows of each square sub-matrix are denoted by r and columns are denoted by l. The boundary conditions are applied to the first (R=1) and the fifth rows (R=5) of the companion matrix.

The boundary conditions for this problem are applied as follows:
For the matrix $\mathcal{A}$:
1) First row-fourth column (r=1, R=1, L=1) is replaced by the first row of the matrix D_1 and the remaining columns (L) of first row are replaced by zeros.
2) second row-fourth column (r=2, R=1, L=1) is replaced by the first row of the matrix D_3 and the remaining columns (L) are replaced by zeros.
3) $N - 1^{th}$ row-fourth column (r=N-1, R=1, L=1) is replaced by the N^{th} row of the matrix D_1 and the remaining columns (L) are replaced by zeros.
4) N^{th} row-fouth column (r=N, R=1, L=1) is replaced by the N^{th} row of the matrix D_0 and the remaining columns (L) are replaced by zeros.
5) First row-sixth column (r=1, R=5, L=6) is replaced by the first row of the matrix D_0 and the remaining columns (L) are replaced by zeros.
6) N^{th} row-sixth column (r=N, R=5, L=6) is replaced by the N^{th} row of the matrix D_0 and the remaining columns (L) are replaced by zeros.
For the matrix $\mathcal{B}$:
1) First row-first column (r=1, R=1, L=1) is replaced by zeros.
2) Second row-first column (r=2, R=1, L=1) is replaced by zeros.
3) $N - 1^{th}$ row-first column (r=N-1, R=1, L=1) is replaced by zeros.
4) N^{th} row-first column (r=N, R=1, L=1) is replaced by zeros.
5) First row-fifth column (r=1, R=5, L=5) is replaced by zeros.
6) N^{th} row-fifth column (r=N, R=5, L=5)is replaced by zeros.

The above system is then solved as a generalized eigenvalue problem ($\mathcal{A}X = \lambda\mathcal{B}X$) as in the temporal stability problem. In this case, the size of the resulting eigenvalue problem has increased by a factor of six. After getting the wavenumber

(α) from the above computation, it is checked for accuracy by substituting it in the temporal stability problem such that the newly computed frequency (ω^*) agrees with the choosen frequency (ω).

4.3 Results on Spatial Stability

4.3.1 Code Validation

The QZ-algorithm of Matlab software is used to solve for the eigenvalue (α) for various Prandtl numbers. In table 4.1, the least-stable eigenvalue (α), obtained by using both the finite difference and spectral methods, is shown for a test case of $P = 0.7$, $\omega = 0.25$ and $G^* = 100$. This test case is computed with different grid points $N = 81$, 101, 121. There is no significant change in the value obtained by both methods.

	FD		Spectral		
	α_i	α_r	α_i	α_r	
$N = 81$	-0.137828	0.816537	-0.138039	0.816592	$N = 81$
$N = 101$	-0.137913	0.816540	-0.137944	0.816510	$N = 101$
$N = 121$	-0.137960	0.816542	-0.138238	0.817000	$N = 121$

Table 4.1: For $G^* = 100$, $\omega = 0.25$, $P = 0.7$, the least stable mode computed by finite difference (FD) and spectral (Spectral) methods for different grid sizes (N); $\alpha_r + \alpha_i i$ is the wavenumber.

Figure 4.1 shows the neutral curves in the (ω, G^*)- plane for $P = 0.7$ and 6.7, computed by spectral and finite difference methods with 101 points. The location of the neutral curve matches with each other for both methods. The spectra in the (c_r, c_i)-plane are shown for $P = 0.7$ and 6.7 in figures 4.2 and 4.3, respectively, along with the effect of grid size. It is observed that the first few modes, along with the least-stable mode, are predicted well by both the finite difference and spectral methods. However, the modes with large decay rates do not agree well which is expected for global eigenvalue solvers.

4.3.2 Results for various Prandtl Numbers

For a range of modified Grashoff numbers G^* and frequency ω, the least-stable eigenvalue is calculated numerically for different Prandtl numbers $P = 0.7$, 6.7, 100, 200 and 500. The corresponding neutral curves, along with different amplification contours, are shown in figures 4.4-4.8. The overall results are similar to those of the temporal stability problem. For example, at high Prandtl number ($P > 100$), we observe an additional instability loop. This new instability loop increases in size in the (ω, G^*)- plane with increasing P. Comparing the spatial growth rate curves in figures 4.4(d)-4.8(d), we find that the spatial growth rate of the least-stable mode decreases with increasing P.

Figure 4.9 shows the eigenfunctions for $P = 0.7$, $G^* = 100$, $\omega = 0.1$; figure 4.10 shows the eigenfunctions for $P = 200$, $G^* = 100$, $\omega = 0.1$ and 0.4, respectively. In these figures, the solid line represent the real part and the dashed line the imaginary part of eigenfunctions. As in the temporal stability case, the eigenfunctions for both stream function and temperature have similar variations with transverse direction.

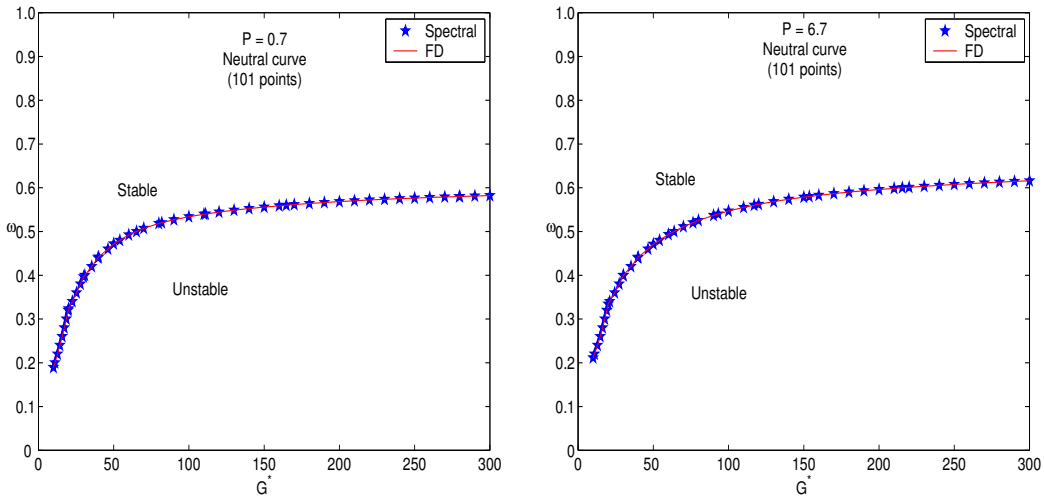

(a) (b)

Figure 4.1: Neutral curves plotted in the $(\omega - G^*)$-plane with parallel flow approximation (a) air P=0.7, (b) water P=6.7. The solid line in each panel correspond to finite difference method (FD) and the star symbols correspond to spectral method.

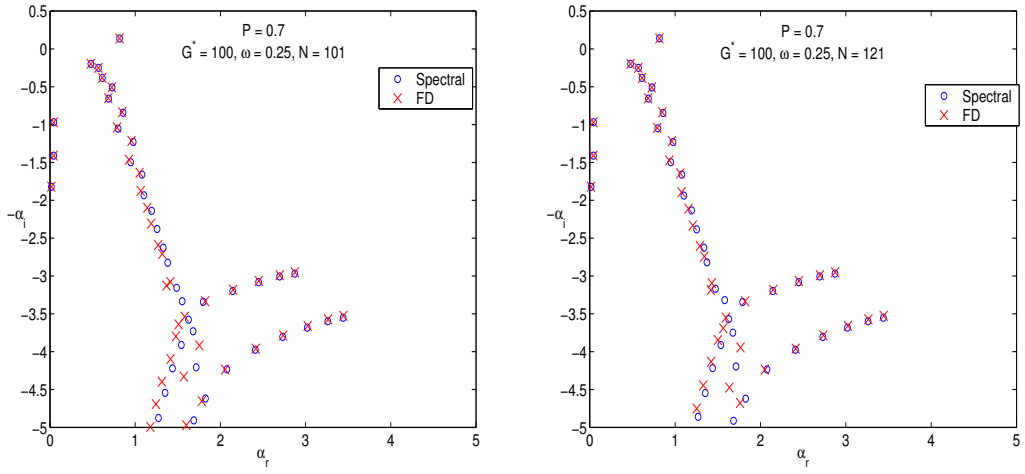

(a) (b)

Figure 4.2: Spectra for air: P=0.7, $G^* = 100$, $\omega = 0.25$; (a) $\alpha_r - \alpha_i$ with 101 grid points (b) $\alpha_r - \alpha_i$ with 121 grid points; here $\alpha_r + \alpha_i$ i is the wavenumber.

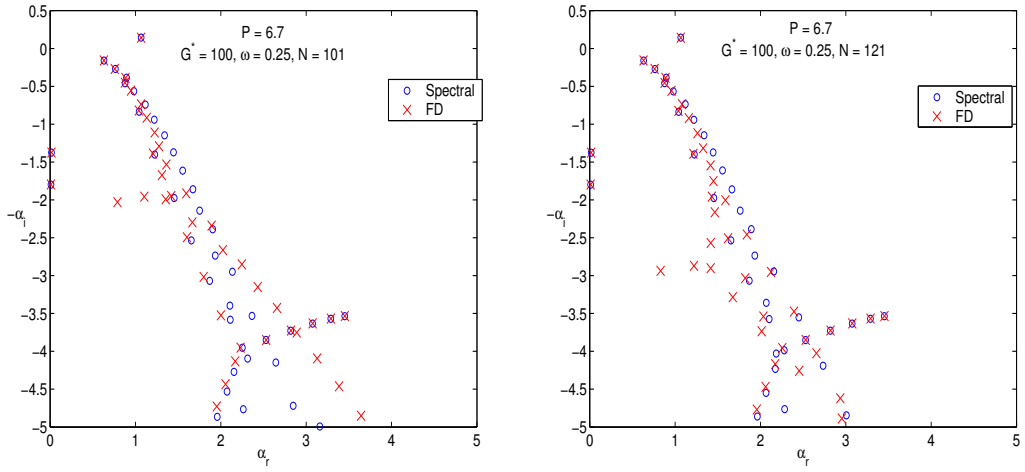

(a) (b)

Figure 4.3: Spectra for water: P=6.7, $G^* = 100$, $\omega = 0.25$; (a) $\alpha_r - \alpha_i$ with 101 grid points (b) $\alpha_r - \alpha_i$ with 121 grid points; here $\alpha_r + \alpha_i$ i is the wavenumber.

4.3.3 Critical Grashof Number

In table 4.2, the critical modified Grashof number G^*_{cr} and the critical wavenumber α_{cr} are shown for different Prandtl numbers P. The variation of G^*_{cr} with P is non-montonic which is shown in figure 4.11. At high Prandtl numbers, the critical

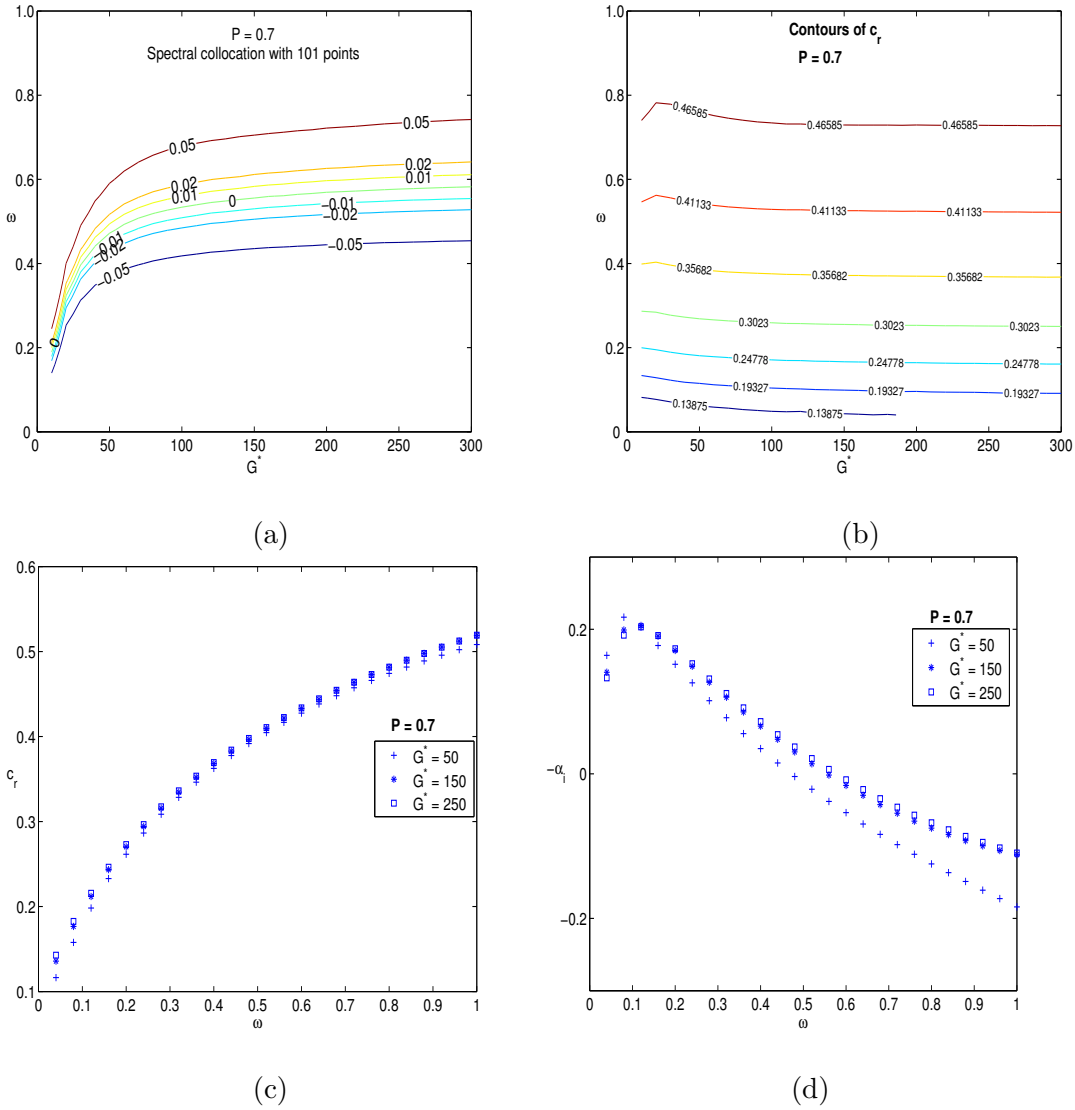

Figure 4.4: For air: P=0.7, (a) Amplification rates in the $(\omega - G^*)$-plane with parallel flow approximation; (b) Contours of phase speed, c_r; (c) Phase speed, c_r, (d) Variation of growth rate, $-\alpha_i$, with ω for three values of Grashoff number $G^* = 50, 150, 250$.

G^* follows a power-law behaviour:

$$G^*_{cr} \sim P^{-1}. \tag{4.4}$$

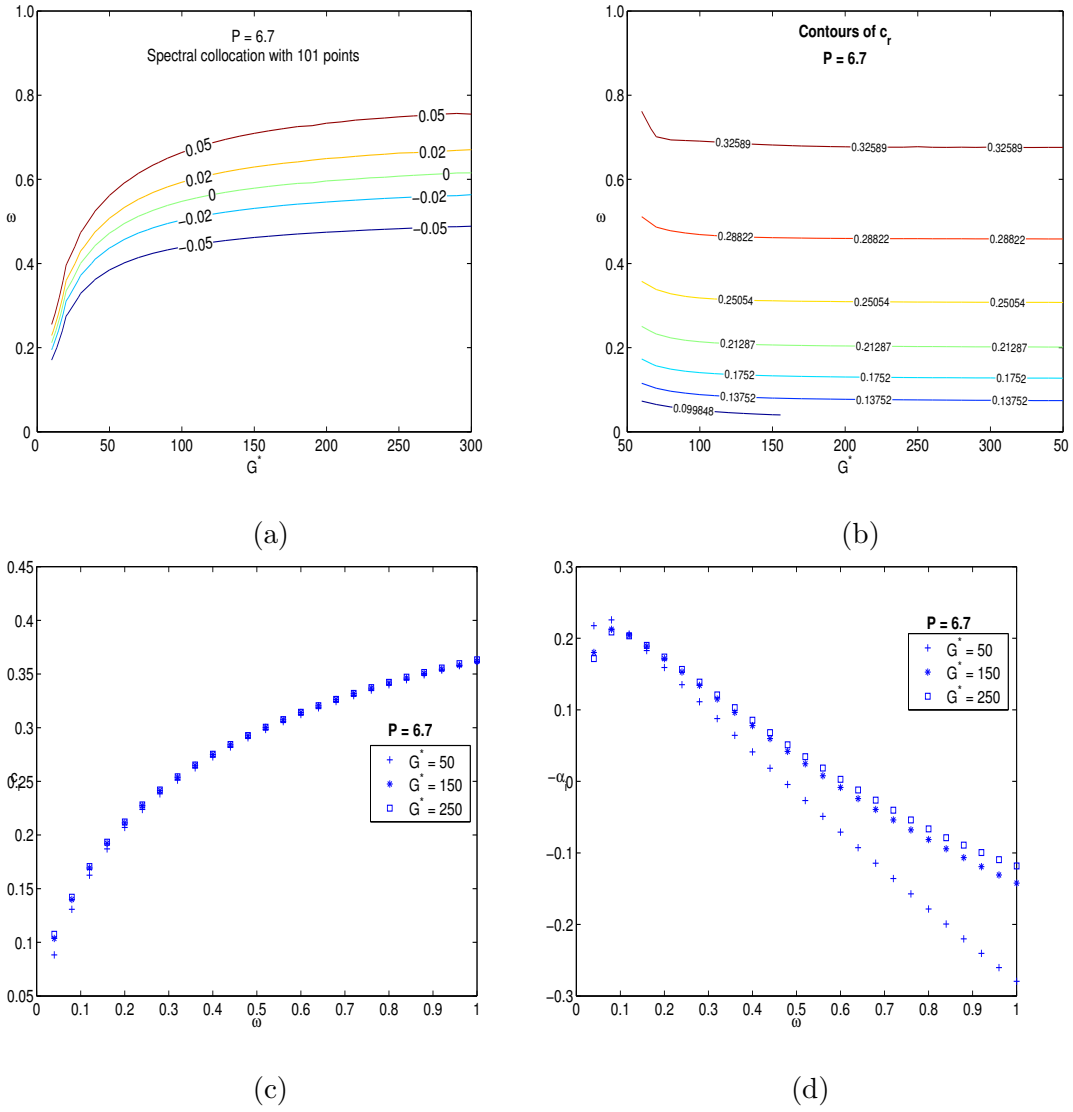

Figure 4.5: For water: P=6.7, (a) Amplification rates in the $(\omega - G^*)$-plane with parallel flow approximation; (b) Contours of phase speed, c_r; (c) Phase speed, c_r, (d) Variation of growth rate, $-\alpha_i$, with ω for three values of Grashoff number $G^* = 50, 150, 250$.

4.4 Non-Parallel Stability

With parallel flow approximation, we have found that a plane thermal plume remains unstable at low values of Grashof number G^*. At such low values of Grashof number, assuming the mean flow as parallel is not correct. The main difficulty in non-parallel flow analysis is in solving the partial differential equations which are non-separable. Several attempts have been made to incorporate nonparallel effects

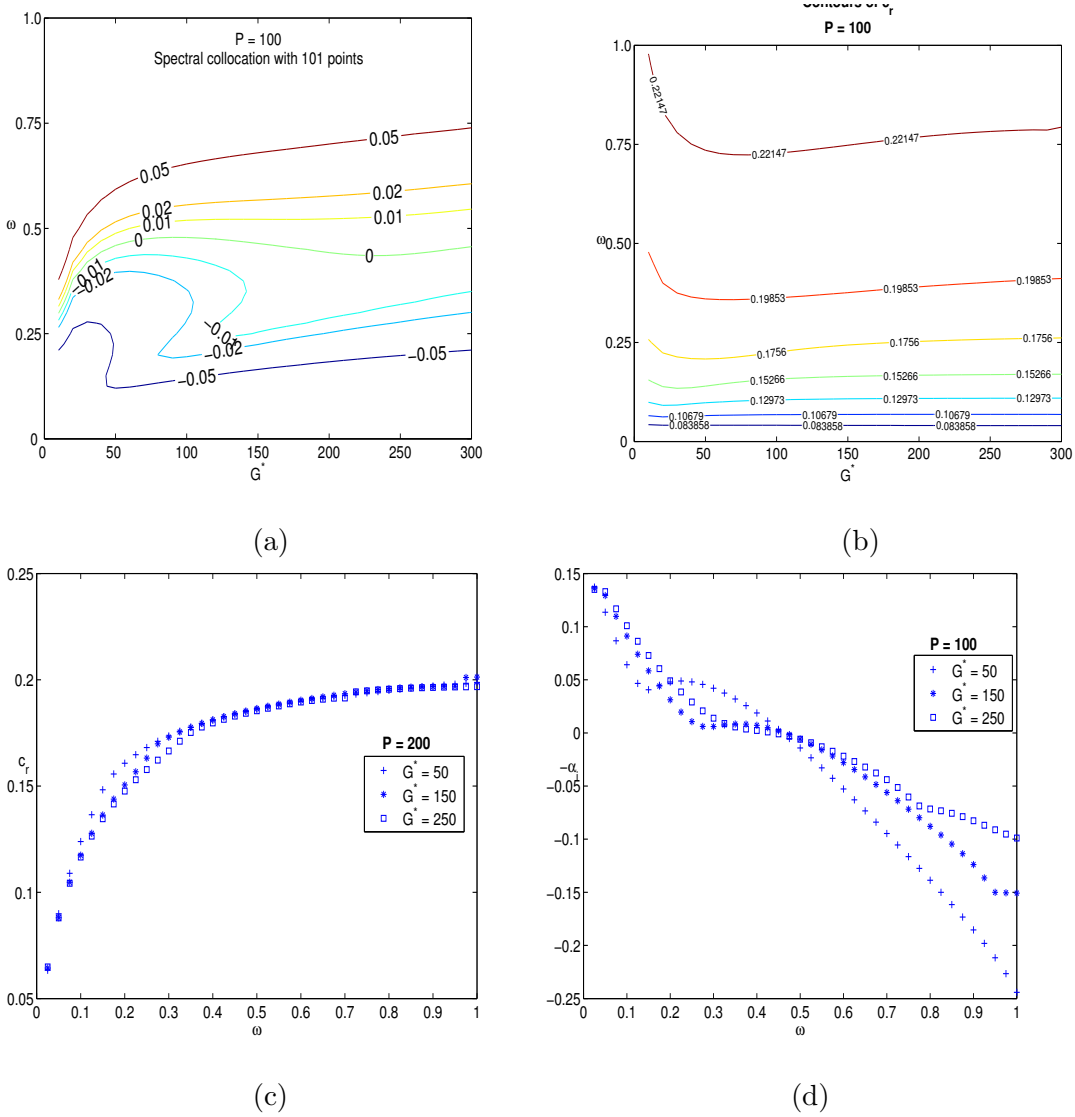

Figure 4.6: For P=100, (a) Amplification rates in the $(\omega - G^*)$-plane with parallel flow approximation; (b) Contours of phase speed, c_r; (c) Phase speed, c_r, (d) Variation of growth rate, $-\alpha_i$, with ω for three values of Grashoff number $G^* = 50$, 150, 250.

(the retention of the normal component of velocity and the streamwise derivatives of the primary flow) so that the governing equations are separable and they reduce to modified Orr-Sommerfeld equation.

Halland & Sparrow (1973) have considered some non-parallel effects on the linear stability of a plane thermal plume. They succeeded in obtaining a complete

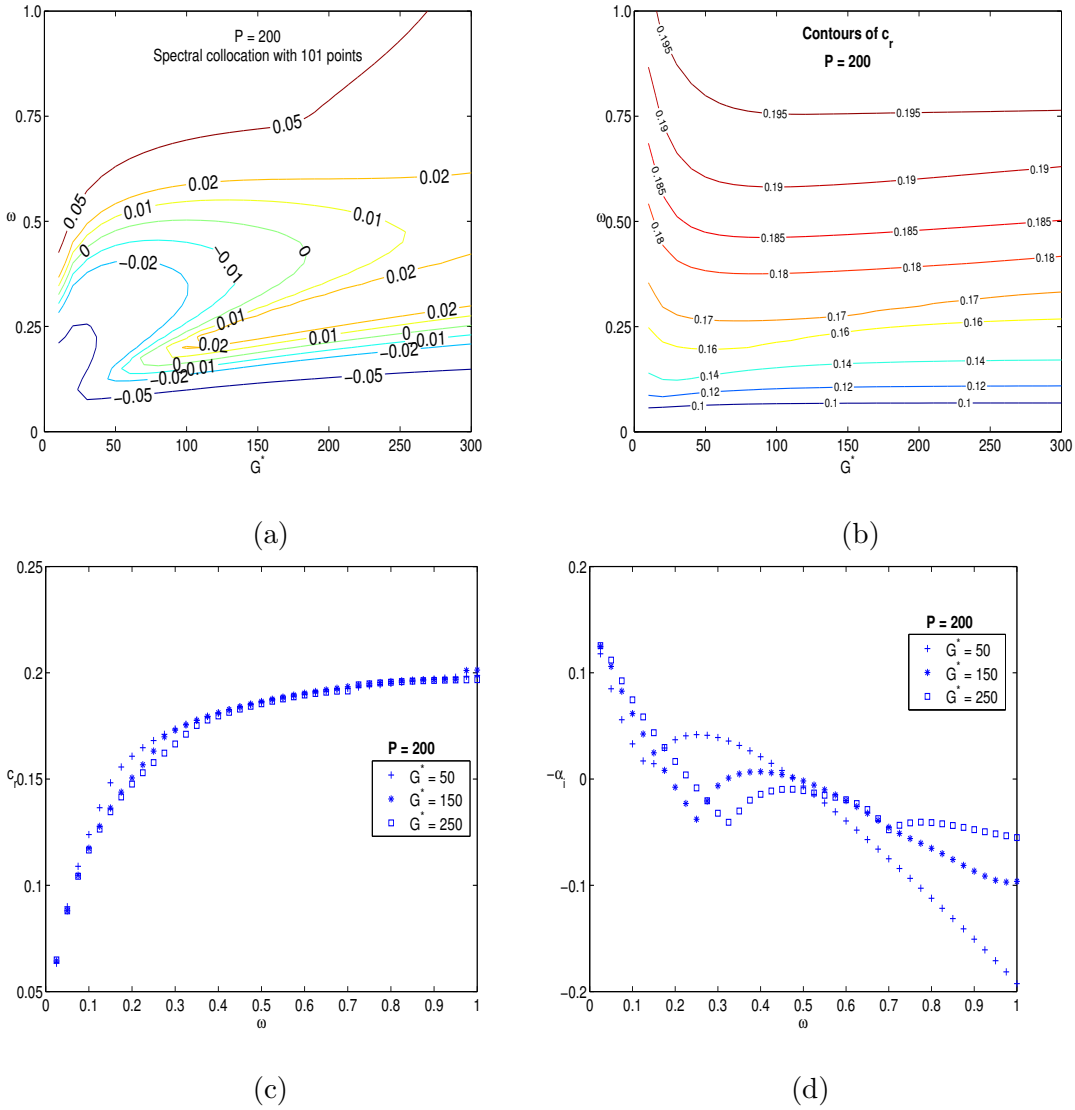

Figure 4.7: For P=200, (a) Amplification rates in the $(\omega - G^*)$-plane with parallel flow approximation; (b) Contours of phase speed, c_r; (c) Phase speed, c_r, (d) Variation of growth rate, $-\alpha_i$, with ω for three values of Grashoff number $G^* = 50$, 150, 250.

neutral curve, which exhibited both a lower branch and a critical Grashof number $G^* = G\xi^{3/5}$ of about 5.1. Their computation shows that the unstable region is smaller than that the region obtained by parallel flow approximation. However, their non-parallel analysis is not correct (Ling & Reynolds 1970). Hieber & Nash (1975) analysed the linear stability analysis of a thermal plume by means of an expansion which allows the incorporation of viscous and temperature coupling at

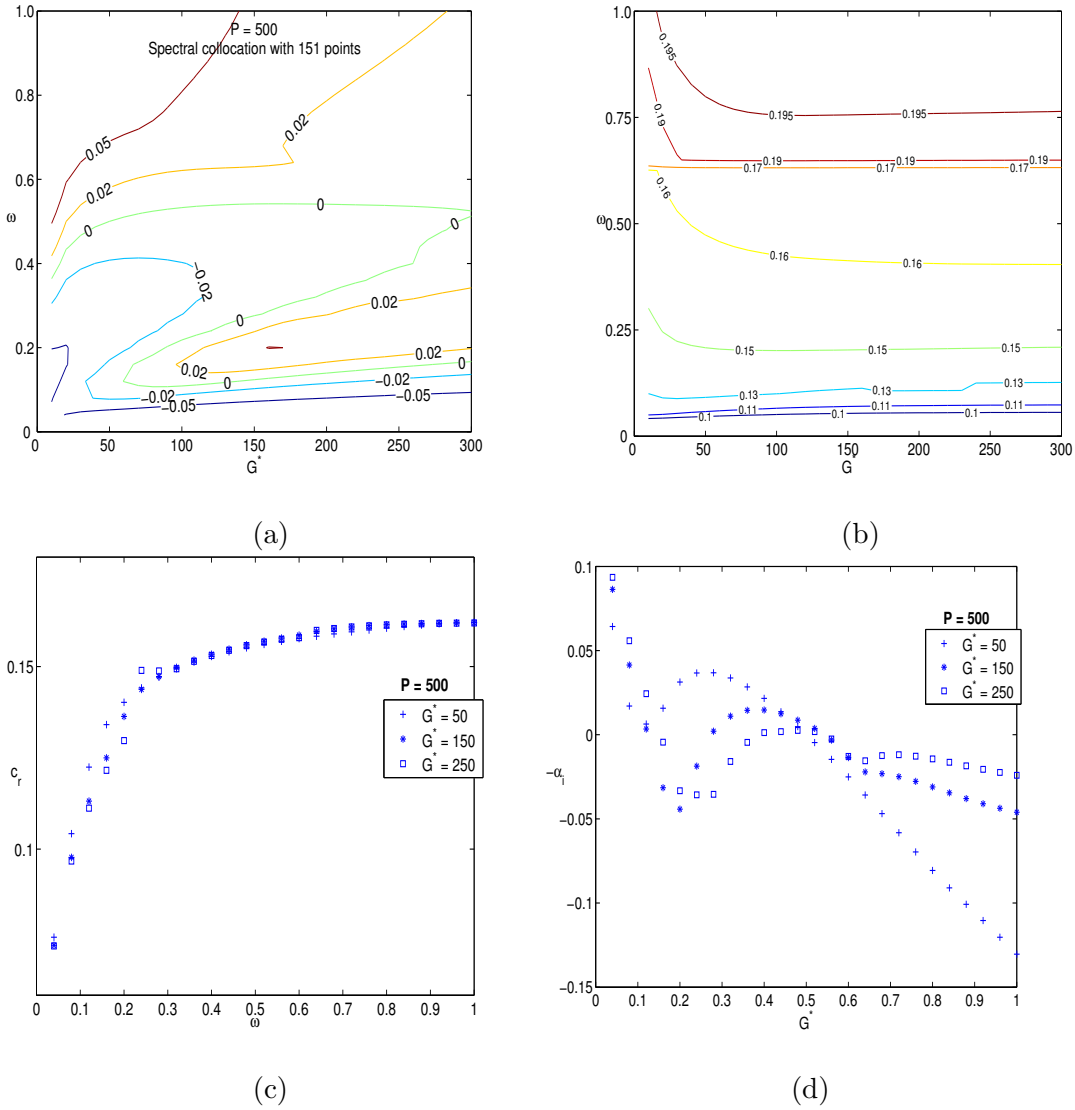

Figure 4.8: For P=500, (a) Amplification rates in the $(\omega - G^*)$-plane with parallel flow approximation; (b) Contours of phase speed, c_r; (c) Phase speed, c_r, (d) Variation of growth rate, $-\alpha_i$, with ω for three values of Grashoff number $G^* = 50$, 150, 250.

higher orders only. In their expansions the leading order terms give inviscid Orr-Sommerfeld equation. This analysis leads to a critical Grashof number G^* of 7.3. In the linear stability theory to treat nearly parallel flows, various methods, like the method of multiple scales, the WKB, and the slowly varying approximation (Gaster 1974, Saric & Nafeh 1975, Garg 1981, Wakitani 1985) are widely used. Here we follow the analysis of Wakitani (1985) to incorporate non-parallel corrections.

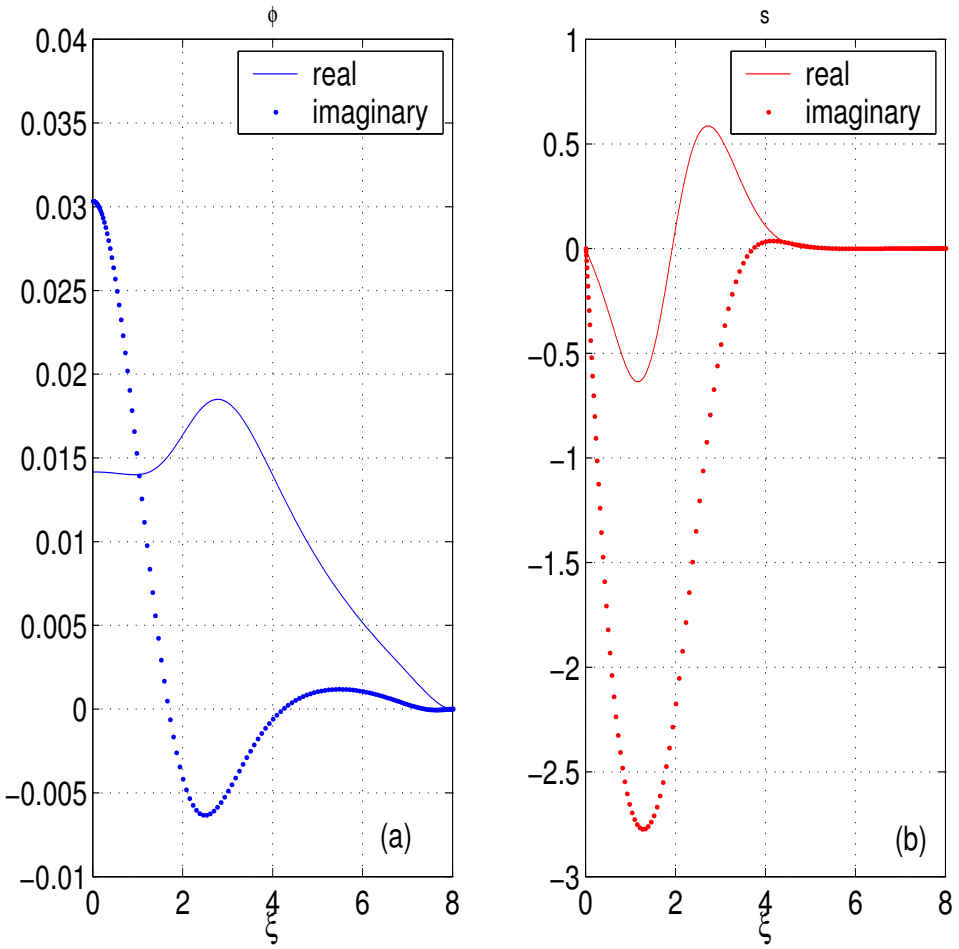

Figure 4.9: Eigenfunctions for $P = 0.7$, $G^* = 100$, $\omega = 0.1$; (a) stream function, (b) temperature.

4.4.1 Formulation of Non-parallel stability Problem

From chapter 3, the leading-order terms $O(\epsilon^0)$ in the governing equations for the disturbance quantities represent the parallel flow approximation and the higher-order terms $O(\epsilon^1)$ are the non-parallel corrections. The computation of non-parallel terms involves the inhomogeneous problem $\mathbf{L\Phi_1} = \mathbf{M}$, equation (3.20). The solution for this equation is possible if and only if the solvability condition is satisfied:

$$\int_0^\infty \mathbf{\Phi^{*T}M} \quad d\eta = 0, \tag{4.5}$$

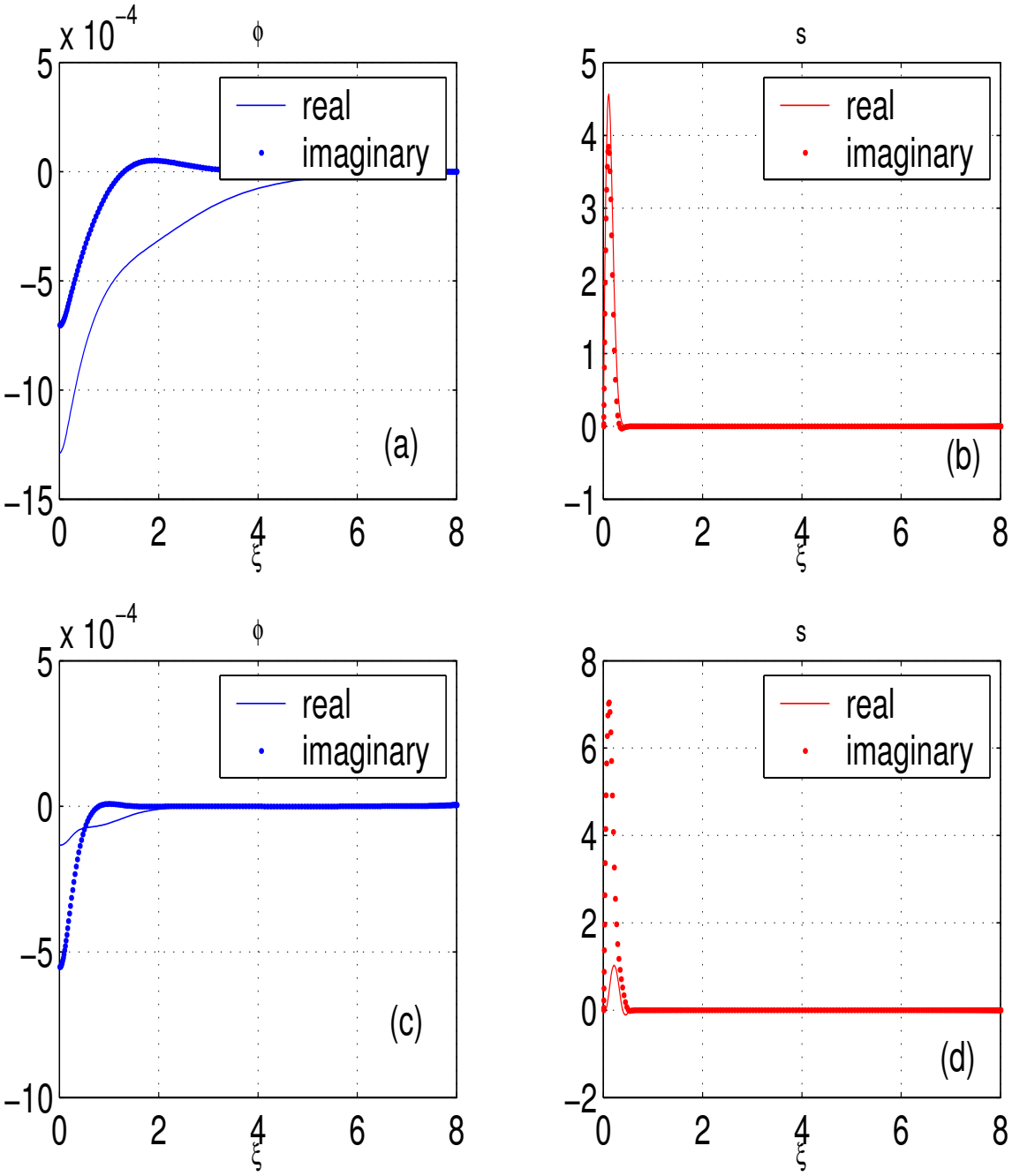

Figure 4.10: Eigenfunctions for $P = 200$, $G^* = 100$; (a), (b) are stream function and temperature for $\omega = 0.1$, (c), (d) are stream function and temperature for $\omega = 0.4$ respectively.

where $\mathbf{\Phi}^{*T} \equiv (\phi^*, s^*)$ denotes the transpose of the adjoint eigenfunction $\mathbf{\Phi}^*$ which satisfies the adjoint equation

$$\mathbf{L}^*\mathbf{\Phi}^* = \mathbf{0}, \tag{4.6}$$

P	G^*_{cr}	α^r_{cr}
0.7	3.8	0.41
2.0	3.0	0.55
6.7	2.1	0.63
10.0	1.9	0.62
50.0	1.0	0.625
100.0	0.6	0.625
200.0	0.185	0.46

Table 4.2: Critical values for Grashof number (G^*) and wavenumber (α) at different Prandtl numbers (P).

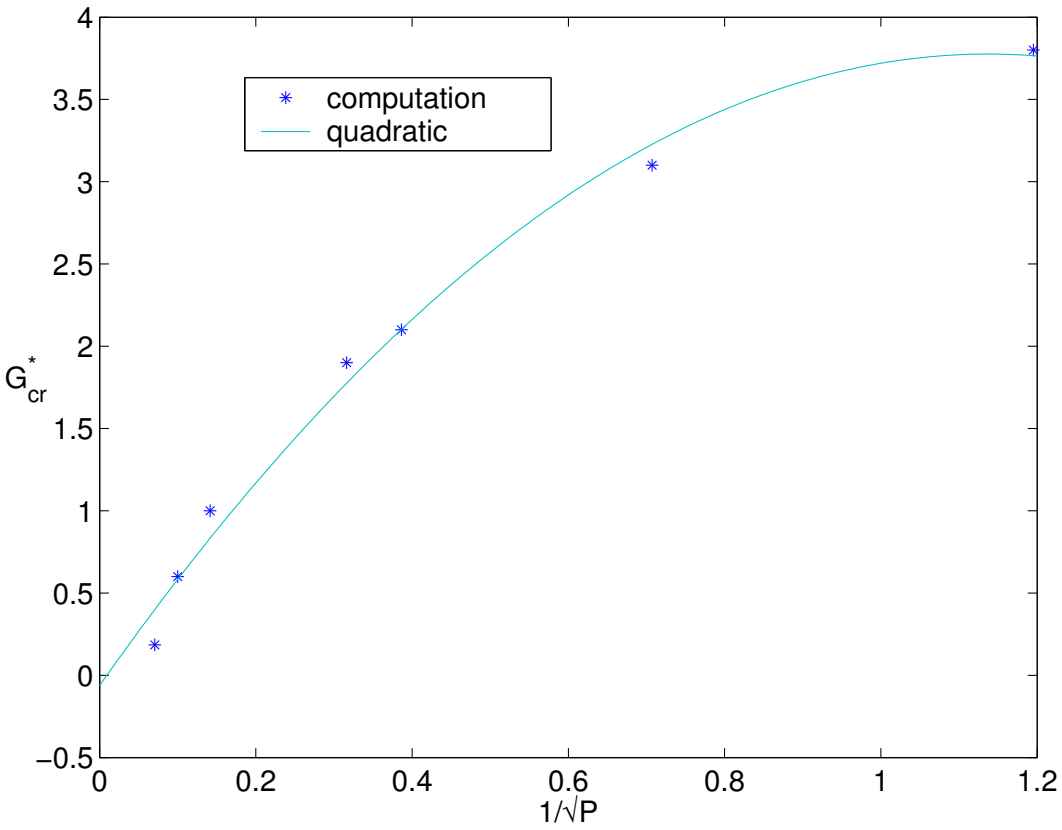

Figure 4.11: Critical Grashof number G^*_{cr} - $1/\sqrt{P}$, it shows at high Prandtl numbers $G^*_{cr} \sim P^{-1}$.

and the boundary conditions are

$$D\phi^*(0) = D^3\phi^*(0) = s^*(0) = 0, \tag{4.7}$$

$$\phi^*(\infty) \to 0, \quad D\phi^*(\infty) \to 0, \quad s^*(\infty) \to 0. \tag{4.8}$$

Here, the adjoint operator is

$$\mathbf{L}^* \equiv \begin{bmatrix} L_1^* & i\alpha h_0^{'} \\ -G^{*-1}D & L_2 \end{bmatrix} \tag{4.9}$$

with $L_1^* \equiv G^{*-1}(D^2-\alpha^2)^2 - i\alpha\left[\left(f_0^{'}-\frac{\omega}{\alpha}\right)(D^2-\alpha^2)+2f_0^{''}D\right]$.
If the solvability condition is satisfied, then the amplitude function $A(\xi)$ can be computed from,

$$\frac{\xi}{A}\frac{dA}{d\xi} = \frac{-\int_0^\infty (F_1\phi^* + F_3 s^*)\,d\eta}{\int_0^\infty (F_2\phi^* + F_4 s^*)\,d\eta}. \tag{4.10}$$

But to solve the above equation we should know $\frac{\partial \Phi_0}{\partial \xi}$ and $\xi\frac{d\alpha}{d\xi}$ in the functions F_1, F_2, F_3, F_4; see equation (3.20). To get these, we differentiate $\mathbf{L\Phi_0} \equiv \mathbf{0}$ with respect to ξ which can be written as

$$\mathbf{L}\left(\xi\frac{\partial \mathbf{\Phi_0}}{\partial \xi}\right) = \begin{pmatrix} g_1 + \xi\frac{d\alpha}{d\xi}g_2 \\ g_3 + \xi\frac{d\alpha}{d\xi}g_4 \end{pmatrix} \tag{4.11}$$

here $g's$ are known functions of ϕ_0 and s_0:

$$g_1 = \frac{3}{5}G^{*-1}\left(\frac{\partial^4\phi_0}{\partial\eta^4} - 2\alpha^2\frac{\partial^2\phi_0}{\partial\eta^2} + \alpha^4\phi_0\right) + \frac{3}{5}G^{*-1}\frac{\partial s_0}{\partial\eta}, \tag{4.12}$$

$$g_2 = -G^{*-1}\left(-4\alpha\frac{\partial^2\phi_0}{\partial\eta^2} + 4\alpha^3\phi_0\right) + if_0^{'}\frac{\partial^2\phi_0}{\partial\eta^2} - 3i\alpha^2 f_0^{'}\phi_0 + 2i\alpha\omega\phi_0 - if_0^{'''}\phi_0, \tag{4.13}$$

$$g_3 = \frac{3}{5}(PG^*)^{-1}\left(\frac{\partial^2 s_0}{\partial\eta^2} - \alpha^2 s_0\right), \tag{4.14}$$

$$g_4 = -ih_0^{'}\phi_0 + (PG^*)^{-1}(2\alpha s_0) + if_0^{'}s_0. \tag{4.15}$$

The boundary conditions are

$$D\left(\xi\frac{\partial\phi_0}{\partial\xi}\right) = D^3\left(\xi\frac{\partial\phi_0}{\partial\xi}\right) = \xi\frac{\partial s_0}{\partial\xi} = 0 \quad \text{at} \quad \eta = 0, \tag{4.16}$$

$$\xi\frac{\partial\phi_0}{\partial\xi} \to 0, \quad D\left(\xi\frac{\partial\phi_0}{\partial\xi}\right) \to 0, \quad \xi\frac{\partial s_0}{\partial\xi} \to 0 \quad \text{at} \quad \eta \to \infty. \tag{4.17}$$

This inhomogeneous equation (4.11) is again solved by applying the solvability condition that gives

$$\xi \frac{d\alpha}{d\xi} = \frac{-\int_0^\infty (g_1\phi^* + g_3 s^*)\, d\eta}{\int_0^\infty (g_2\phi^* + g_4 s^*)\, d\eta}. \tag{4.18}$$

4.4.2 Algorithm to Compute Non-parallel Corrections

1) For given P, G^* and ω, the non-linear eigenvalue α is computed as in section 4.3.
2) Eigenfunctions (ϕ_0, s_0) and it's derivatives are computed.
3) From the adjoint equation (4.6), the adjoint eigenfunctions (ϕ^*, s^*) are computed.
4) $\xi \frac{d\alpha}{d\xi}$ is computed from equation (4.18) by using trapezoidal rule.
5) Inhomogenious equation (4.11) is solved for $\xi \frac{\partial \Phi_0}{\partial \xi}$.
6) Finally, equation (4.10) is solved for $\frac{\xi}{A}\frac{dA}{d\xi}$.

4.4.3 Amplification Rates with Non-parallel Corrections

In the case of parallel flows, the eigenfunctions are independent of the streamwise location ξ, and the exponential part of the stream function or temperature gives the amplification rate and the wavenumber. In the case of non-parallel flows, the eigenfunctions vary with the streamwise location, and the wavenumber and the amplification rate depend on the disturbance quantities considered. So the neutral curves are affected by choosing different quantities such as velocity, kinetic-energy, thermal-energy, etc. We define the disturbance kinetic-energy and the thermal-energy integrals as

$$E = \int_0^\infty \left(u^2 + v^2\right) dy, \tag{4.19}$$

$$H = \int_0^\infty \theta^2 dy. \tag{4.20}$$

The amplification rates based on these quantities are (Wakitani 1985):

$$K(E) \equiv 2\frac{\xi^{\frac{2}{5}}}{G}\frac{1}{E}\frac{dE}{d\xi} = -\alpha_i + \left(\frac{4}{G^*}\right)^{-1}\left[\left(\frac{\xi}{A}\frac{dA}{d\xi}\right)_r + \frac{\xi}{2e}\frac{de}{d\xi} + \frac{2}{5}\right], \quad (4.21)$$

$$K(H) \equiv 2\frac{\xi^{\frac{6}{5}}}{G}\frac{1}{H}\frac{dH}{d\xi} = -\alpha_i + \left(\frac{4}{G^*}\right)^{-1}\left[\left(\frac{\xi}{A}\frac{dA}{d\xi}\right)_r + \frac{\xi}{2h}\frac{dh}{d\xi} - \frac{2}{5}\right]. \quad (4.22)$$

where

$$e = \int_0^\infty \left(\mid D\phi_0 \mid^2 + \mid \alpha \mid^2 \mid \phi_0 \mid^2\right) d\eta, \quad \text{and} \quad h = \int_0^\infty \mid s_0 \mid^2 d\eta. \quad (4.23)$$

4.5 Results on Non-parallel Stability

4.5.1 Code Validation

After computing the amplification rates from parallel flow approximation, the non-parallel correction terms specified in the equations (4.21) and (4.22) are computed for various Prandtl numbers. In table 4.3, the amplification rates obtained by using the parallel flow approximation and the non-parallel approximation are shown for a test case $P = 0.7$, $G^* = 100$, $\omega = 0.25$. Figure 4.12 shows the neutral curve

	α (parallel)	$K_f(E)$	$K_f(H)$	$K_s(E)$	$K_s(H)$
$N = 81$	0.816574-0.137874 i	0.147284	0.116586	0.147750	0.117217
$N = 101$	0.816577-0.137959 i	0.147367	0.116673	0.147729	0.117199
$N = 121$	0.816579-0.138238 i	0.147413	0.116721	0.147703	0.117176

Table 4.3: For Air ($P = 0.7$), $G^* = 100$, $\omega = 0.25$, amplification rates are $-\alpha_i$, $K_i(E)$, $K_i(H)$, where the suffix $i = f, s$ denote the finite difference and spectral methods respectively.

for $P = 0.7$, computed with 101 grid points. In these plots, the neutral cuves represented by *parallel*, $K(E)$, $K(H)$ are parallel flow approximation, non-parallel corrections for kinetic-energy and thermal-energy integrals, respectively. It is clear that the neutral stability curve depends on the choice of the disturbance quantity which is used to define the corrected amplification rates (equations (4.21-4.22). From figure 4.12(b), it is observed that the critical Grashof number is smaller for

the kinetic energy K(E) than that for the thermal energy K(H). For both K(E) and K(H), there is a lower branch of the neutral stability curve. It may be recalled that the lower branch coincides with $\omega = 0$ line for the parallel flow analysis.

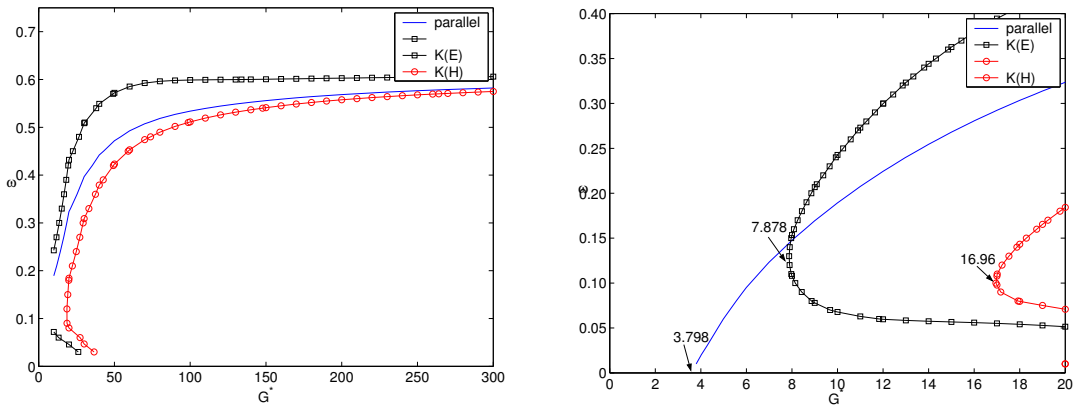

(a) (b)

Figure 4.12: Neutral curves plotted in the $(\omega - G^*)$-plane with parallel flow approximation (parallel), non-parallel corrections using kinetic-energy integral K(E) and thermal-energy integral K(H) repectively with N=101 points, air ($P = 0.7$). (a) With out zooming (b) with zoomed region, critical Grashof numbers are indicated in this plot.

4.5.2 Results for various Prandtl numbers

For a range of Grashoff numbers G^* and frequency ω, different amplification rates are calculated numerically for different Prandtl numbers $P = 0.7$ and 6.7. The corresponding amplification rates are shown in figures 4.13. It is observed that the amplification rates are the largest for K(E) at high-frequencies ($\omega > 0.2$), but the amplification rates based on parallel flow approximation dominate at low frequencies ($\omega < 0.2$).

The stability diagrams with non-parallel approximations are shown in figures 4.14 and 4.15 for a range of P. It is observed that the region of instability is larger for K(E), compared to the region of instability obtained by K(H) or the parallel flow assumptions. The neutral curves obtained by the parallel flow assumption, the kinetic-energy integral and the thermal-energy integral are asymptotically reaching a limit (ω) at large G^* and this limit is increasing with the Prandtl number (figure

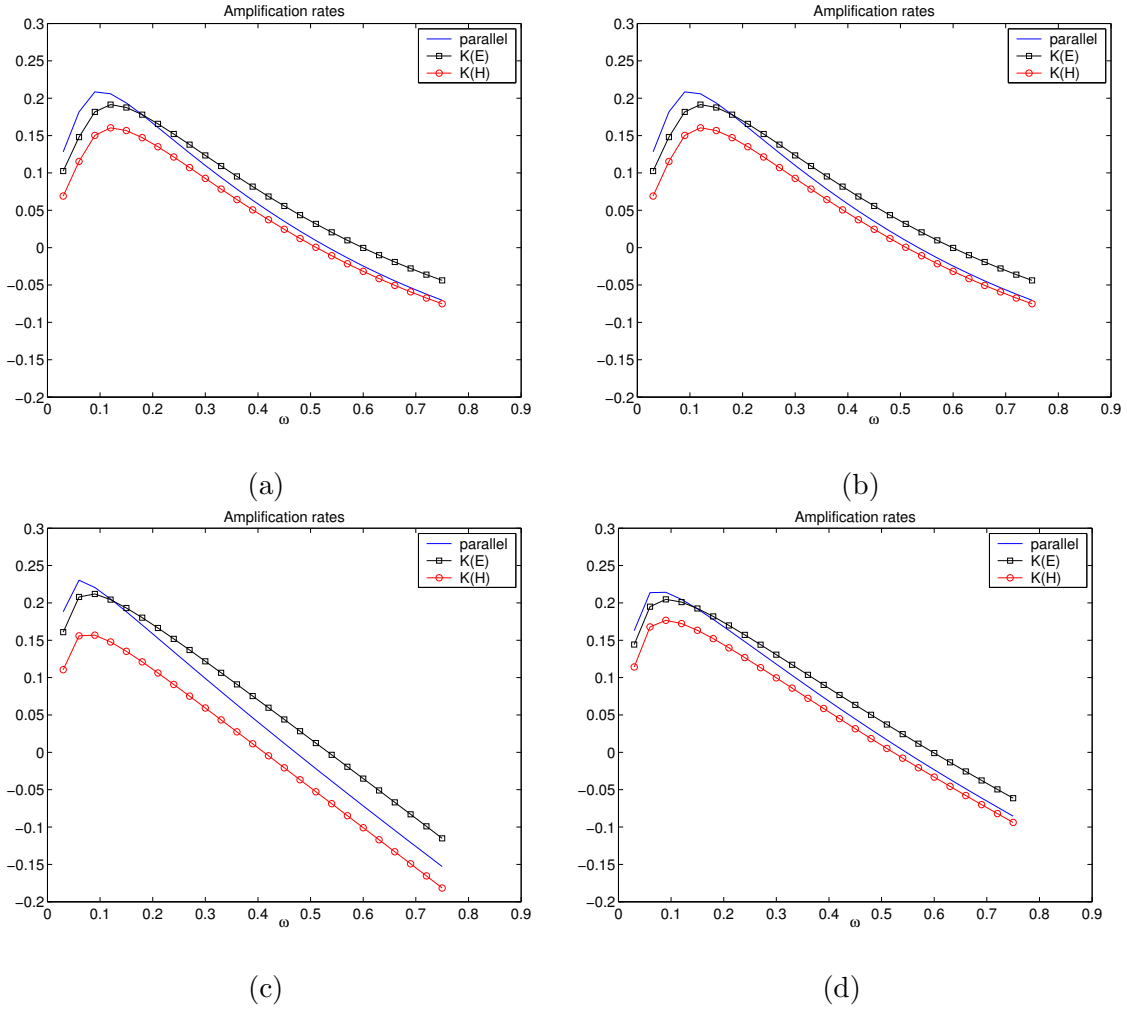

Figure 4.13: Amplification rates (a) $P = 0.7$, $G^* = 50$ (b) $P = 0.7$, $G^* = 100$; (c) $P = 6.7$, $G^* = 50$; (d) $P = 6.7$, $G^* = 100$;

4.14 and 4.15).

Overall, the new instability loop at high Prandtl number (see figure 4.15) remains relatively unaffected with the inclusion of non-parallel effects. We should mention that the non-parallel results at high Prandtl numbers (figures 4.15 and 4.16) need to be verified by some other numerical method (e.g. Runge-Kutta method) since we had difficulty in solving the inhomogeneous problem (equation 4.11) due to the large condition number of the related matrix. This added work will be taken up in the future.

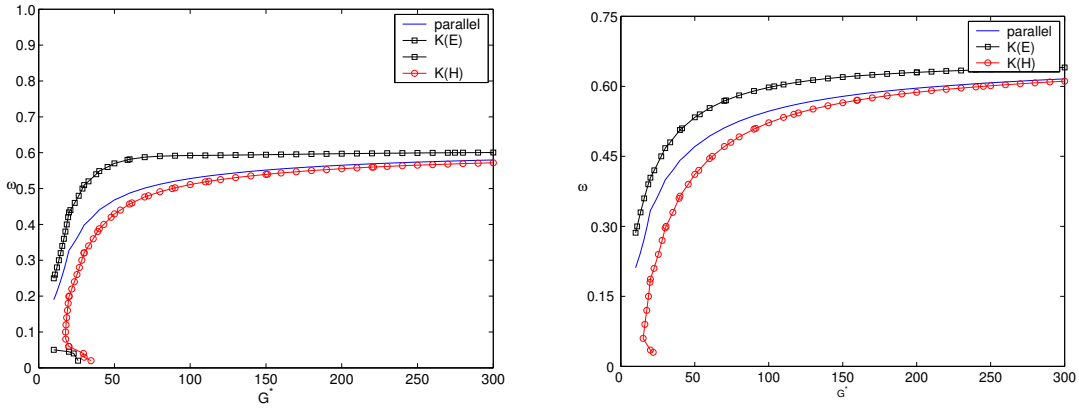

(a) (b)

Figure 4.14: Neutral curves plotted in the $(\omega - G^*)$-plane with parallel flow approximation (parallel), non-parallel corrections using kinetic-energy integral K(E) and thermal-energy integral K(H) repectively with N=101 points. (a) $P = 2.0$; (b) $P = 6.7$.

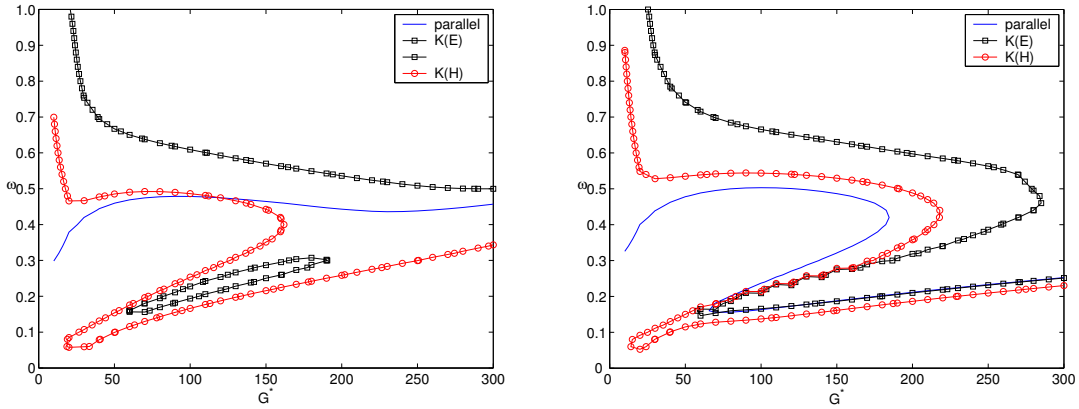

(a) (b)

Figure 4.15: Neutral curves plotted in the $(\omega - G^*)$-plane with parallel flow approximation (parallel), non-parallel corrections using kinetic-energy integral K(E) and thermal-energy integral K(H) repectively with N=101 points. (a) $P = 100.0$; (b) $P = 200.0$.

The critical values for Grashof number and frequency are shown in table 4.4 and 4.5 for $P = 0.7, 1.0, 2.0$.

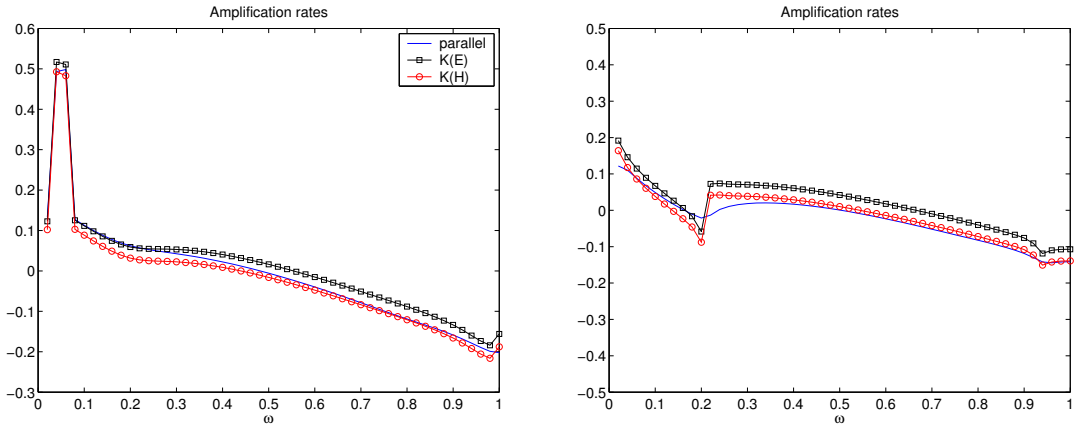

(a) (b)

Figure 4.16: Amplification rates are plotted for parallel flow approximation (parallel), non-parallel corrections using kinetic-energy integral K(E) and thermal-energy integral K(H) repectively with N=101 points. (a) $P = 50.0, G^* = 100$; (b) $P = 200.0, G^* = 100$.

	parallel	K(E)	K(H)
$P = 0.7$	3.8	7.9	17.0
$P = 1.0$	3.6	6.5	15.5
$P = 2.0$	3.0	5.0	14.9

Table 4.4: Critical Grashof number at different Prandtl numbers.

	parallel	K(E)	K(H)
$P = 0.7$	0.0	0.13	0.11
$P = 1.0$	0.0	0.10	0.088
$P = 2.0$	0.0	0.52	0.24

Table 4.5: Critical frequency at different Prandtl numbers.

CHAPTER 5

SUMMARY AND OUTLOOK

A plane thermal plume over a line heat source is analysed for the mean flow and the stability to the infinitesimal disturbances at different Prandtl numbers. The boundary-layer approximations are considered and the governing mean flow equations are solved by using Runge-Kutta method with different grid sizes. The linear stability equations are computed by using the finite difference and the spectral methods.

For the mean flow, both the leading-order and first-order boundary-layer equations are transformed into a set of nonlinear ODE's in terms of similarity variables. The nonlinear ODE's for the mean flow are solved by using the Runge-Kutta method with 4^{th}-order accuracy. By using Newton-Raphson correction, the solution is accelarated with good accuracy. Results have been checked with different grid sizes. The numerical solutions for the mean flow quantities are well matched with the analytical solution at Prandtl number $P = 2$. With increasing Prandtl number, the thermal boundary layer becomes thinner and the velocity levels are decreased in the plume. Since the viscous diffusion is more for high Prandtl number fluids, the velocity profile becomes flatter with increasing P. For a given Prandtl number, the maximum temperature in the plume decreases as minus three-fifth power of the height. Higher-order correction terms for the mean flow are also solved by Runge-Kutta method with the Newton-Raphson correction. The mean flow results after adding higher-order correction terms suggests that the center-line temperature decreases and the flow velocity increases near edge of the boundary layer. These incremental changes in velocity and temperature are relatively smaller for high Prandtl number fluids which suggests that the mean flow quantities of a thermal plume can be well predicted by the leading-order boundary-layer equations at high Prandtl numbers.

The linear stability equations are solved with parallel flow approximations as well as with non-parallel correction terms. The temporal stability analysis is car-

ried with parallel flow approximations with the finite difference and the spectral methods. For computing eigenvalues, the Arnoldi algorithm is used which takes less time compared to the the standard QZ algorithm. At high Prandtl numbers ($P > 100$), the neutral curve shows an additional unstable loop, and the size of this unstable loop increases with increasing Prandtl number. This additional mode appears because of the interaction of the hydrodynamic and thermal disturbances. At high Prandtl numbers, the contribution from the Reynold's stress terms is very small compared to the gain in energy by buoyancy forces. Disturbances gaining thermal energy from the mean flow are dissipated and do not contribute to the potential energy.

For spatial stability, the companion matrix method is used to obtain nonlinear eigenvalues. At high Prandtl numbers, the critical modified Grashof number follows a power-law relation with Prandtl number: $G^*_{cr} \sim \frac{1}{P}$. It is shown that considering uncoupled disturbance equations does not lead to correct results at higher Prandtl numbers for which $G^*_{cr} \sim P^{0.2375}$. Limited results are shown for different Prandtl numbers for the non-parallel analysis for which the property of adjoint functions are used to obtain amplification rate correction terms. The non-parallel results at high Prandtl numbers need to be verified using some other numerical method (e.g. Runge-Kutta method).

The present work uncovered a new instability mode in a plane thermal plume. The origin of this "buoyancy-driven" instability mode suggests that the hydrodynamic and thermal disturbances cannot be decoupled for a high Prandtl number thermal plume.

Apart from the mean flow and stability results on thermal plumes, another contribution of the present Thesis is the development of a linear stability code for flows related to convection phenomena. The present stability code can be used to compute eigenvalues for mixed convection problems, like the flow over a vertical flat plate, the heated thermal jet and the free shear mixing layers (one fluid is hot and the other is cold). These studies are more involved compared to the purely buoyancy-driven thermal plume, but are likely to yield more interesting results at higher Prandtl numbers.

APPENDIX I

EFFECT OF VISCOUS DISSIPATION TERMS IN THE DISTURBANCE ENERGY EQUATION

In this thesis, we considered the energy equation without the viscous dissipation ($\mathbf{\Phi^*_{VD}}$) term. Gebhart (1962) showed that the dissipation terms are neglizible, but the computations in the present work show a significant effect on the neutral stability curves at high Prandtl numbers. Let us consider the energy equation in non-dimensional form (with dissipation terms from chapter 2),

$$\frac{\partial\theta^*}{\partial\tilde{\tau}^*} + u^*\frac{\partial\theta^*}{\partial x^*} + v^*\frac{\partial\theta^*}{\partial y^*} = \frac{1}{P\sqrt{Gr}}\nabla^2\theta^* + D_p P\sqrt{G}r\mathbf{\Phi^*_{VD}}, \tag{I.1}$$

where

$$\mathbf{\Phi^*_{VD}} = \frac{2}{3}\left[2\left(\frac{\partial u^*}{\partial x^*}\right)^2 + 2\left(\frac{\partial v^*}{\partial y^*}\right)^2 - 2\frac{\partial u^*}{\partial x^*}\frac{\partial v^*}{\partial y^*} + \left(\frac{\partial u^*}{\partial y^*} + \frac{\partial v^*}{\partial x^*}\right)^2\right].$$

After adding perturbations and subtracting the mean energy equation gives the energy equation for the perturbation terms

$$s'' - \alpha^2 s = i\alpha PG^*\left[\left(f_0' - \frac{\omega}{\alpha}\right)s - h_0'\phi\right] - \frac{4}{3}\{D_p PG^*\}f_0''\left(\phi'' - \alpha^2\phi\right). \tag{I.2}$$

The last term in the above equation represents viscous dissipation with the dissipation parameter 'D_p' being a constant. The temporal stability characteristics for $P = 500$ and 1000 for dissipation parameters $D_p = 1.0e-5$ and 1.0 are shown in figure I.1. The neutral curves for $P = 500$ (figure I.1(c)) and $P = 1000$ (figure I.1(d)) clearly show that the role of the dissipation parameter is to stabilize the flow. The disturbance energy is taken away by viscous dissipation and hence the flow is more stable. Note that the upper unstable loop is affected by the viscous dissipation, but the lower unstable loop remains largely unaffected.

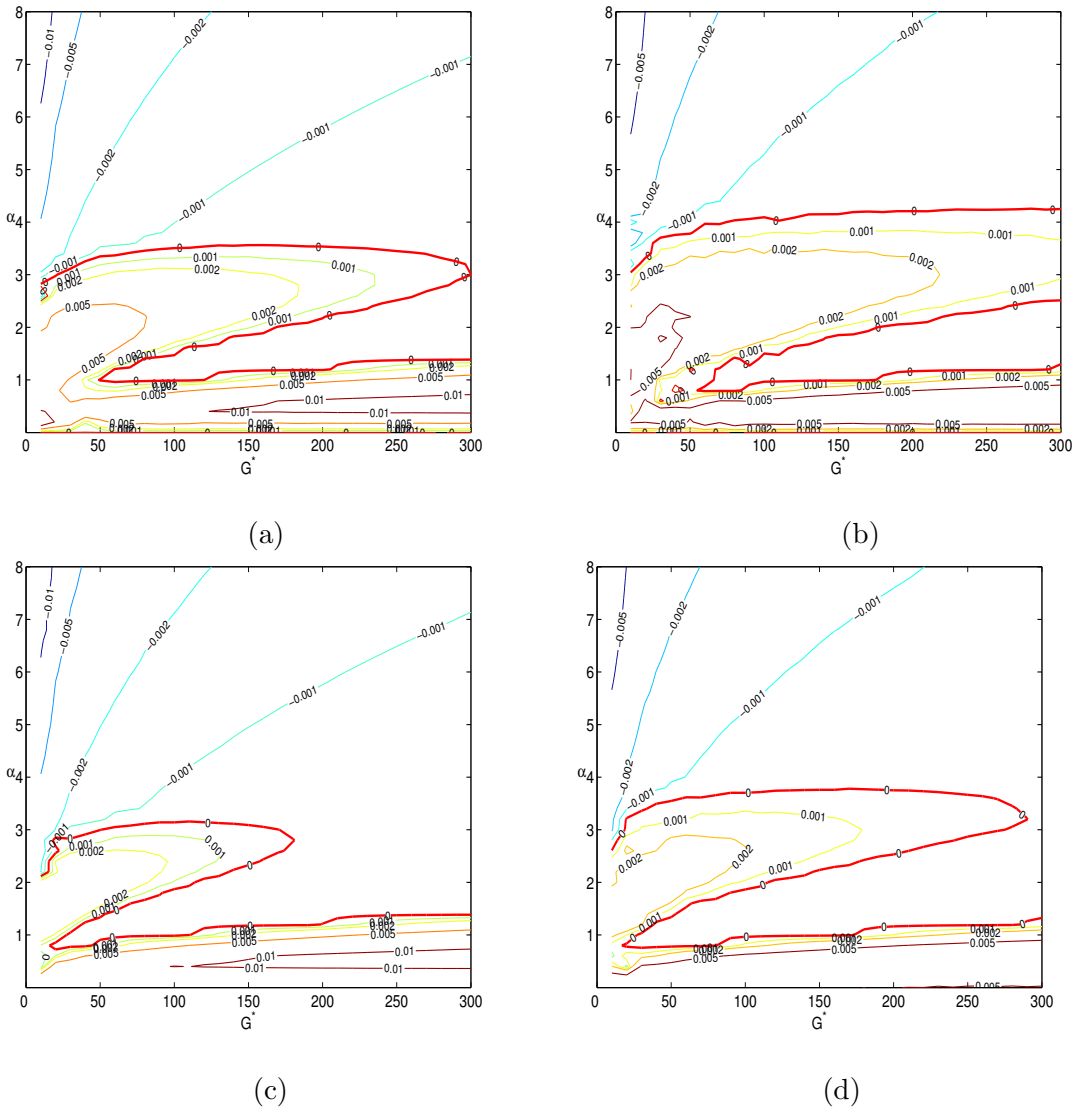

Figure I.1: Effect of viscous dissipation on the stability diagram: (a) $P = 500$, (b) $P = 1000$, with dissipation parameter D_p=1.0e-5; (c) $P = 500$, (d) $P = 1000$, with dissipation parameter D_p=1.0.

References

Afzal, N. 1980 Convective wall plume: Higher order analysis. *Int. J. Heat Mass Transfer.* **23**, 505–513.

Alam, M. & Arakeri, V. H. 1993 Observations on transition in plane bubble plumes. *J. Fluid Mech.* **254**, 363–374.

Batchelor, G. K. 1954 Heat convection and buoyancy effects in fluids. *Q. J. R. Met. Soc.* **80**, 339–359.

Brand, R. & Lahey, F. 1967 The heated laminar vertical jet. *J. Fluid Mech.* **29**, 305–315.

Bridges, T. J. & Morris, P. J. 1984 Differential eigenvalue problems in which the parameter appears nonlinearly. *J. Comp. Phys.* **55**, 437–460.

Brodowicz, K. & Kierkus, W. T. 1966 Experimental investigation of laminar free convection flow in air above horizontal wire with constant heat flux. *Int. J. Heat Mass Transfer.* **9**, 81–94.

Caballina, O., Climent, E. & Dusek, J. 2003 Two-way coupling simulations of instabilities in a plane bubble plume. *Phys. Fluids.* **15**, 1535–1544.

Canuto, C., Hussani, M. Y., Quarteroni, A. & Zang, T. A. 1988 *Spectral Methods in Fluid Dynamics*. New York: Springer-Verlag Inc.

Fujii, T. 1963 Theory of the steady laminar natural convection above a horizontal line heat source and a point heat source. *Int. J. Heat Mass Transfer.* **6**, 597–606.

Fujii, T., Morioka, I. & Uehara, H. 1973 Buoyant plume above a horizontal line heat source. *Int. J. Heat Mass Transfer.* **16**, 755–768.

Garg, V. K. 1981 Spatial stability of the non-parallel bickley jet. *J. Fluid Mech.* **102**, 127–140.

Gaster, M. 1974 On the effects of boundary-layer growth on flow stability. *J. Fluid Mech.* **66**, 465–480.

Gebhart, B. 1962 Effects of viscous dissipation in natural convection. *J. Fluid Mech.* **14**, 225–232.

Gebhart, B., Jaluria, Y., Mahajan, R. L. & Sammakia, B. 1988 *Buoyancy Induced Flows and Transport*. Washington: Hemisphere Publishing.

Gebhart, B. & Mahajan, R. L. 1982 *Instability, Transition, and Turbulence*. Newyork: Academic Press.

Gebhart, B., Pera, L. & Schorr, A. 1970 Steady laminar natural convection plumes above a horizontal line heat source. *Int. J. Heat Mass Transfer.* **13**, 161–171.

Gill, A. E. & Davey, A. 1969 Instabilities of a buoyancy-driven system. *J. Fluid Mech.* **35**, 775–798.

Grossmann, S. & Lohse, D. 2003 Scaling in thermal convection: a unifying theory. *J. Fluid Mech.* **407**, 27–56.

Halland, S. E. & Sparrow, E. M. 1973 Stability of buoyant boundary layers and plumes, taking account of non-parallelisim of the basic flows. *J. Heat Transfer.* **95C**, 295–301.

Hieber, C. A. 1974 Natural convection around a semi infinite vertical plate: Higher order effects. *Int. J. Heat Mass Transfer.* **17**, 785–791.

Hieber, C. A. & Nash, E. J. 1975 Natural convection above a line heat source: Higher order effects and stability. *Int. J. Heat Mass Transfer.* **18**, 1473–1479.

Kaminski, E. & Jaupart, C. 2003 Laminar starting plumes in high prandtl number fluids. *J. Fluid Mech.* **478**, 287–298.

Knowles, C. P. & Gebhart, B. 1971 The stability of the laminar natural convection boundary layers. *J. Fluid Mech.* **34**, 657–686.

Kuiken, H. K. & Rotem, Z. 1971 Asymptotic solution for plume at very large and small prandtl numbers. *J. Fluid Mech.* **45**, 585–600.

Kurdyumov, V. N. 2005 Natural convection near an isothermal wall far downstream from a source. *Phys. Fluids.* **17**, 087106.

Ling, C. H. & Reynolds, W. C. 1973 Non-parallel flow corrections for the stability of shear flows. *J. Fluid Mech.* **59**, 571–591.

Malik, M. R. 1990 Numerical methods for hypersonic boundary layer stability. *J. Comp. Phys.* **86**, 376–413.

Mollendorf, J. & Gebhart, B. 1969 Viscous dissipation in external natural convection flows. *J. Fluid Mech.* **38**, 97–107.

Natchtsheim, P. R. 1963 Stability of free convection boundary layer flows. *Tech. Rep.*. National Aeronautics and Space Administration (NASA).

Nayar, N. & Ortega, J. M. 1993 Computation of selected eigenvalues of generalized eigenvalue problems. *J. Comp. Phys.* **86**, 8–14.

Niemela, J. J. & Sreenivasan, K. R. 2006 Turbulent convection at high rayleigh numbers and aspect ratio 4. *J. Fluid Mech.* **557**, 411–422.

Pera, L. & Gebhart, B. 1971 On the stability of laminar plumes: Some numerical solutions and experiments. *Int. J. Heat Mass Transfer.* **14**, 975–984.

Puthenveettil, B. A. & Arakeri, J. H. 2005 Plume structure in high-rayleigh-number convection. *J. Fluid Mech.* **542**, 217–249.

Riley, N. 1974 Free convection from a horizontal line source of heat. *ZAMP.* **25**, 817–828.

Saad, Y. 2000 *Iterative methods for sparse linear systems*, 2nd edn. PA: SIAM.

Saric, W. S. & Nayfeh, A. H. 1975 Nonparallel stability of boundary-layer flows. *Phys. Fluids.* **18**, 945–950.

Spalding, D. B. & Cruddace, R. 1961 Theory of the steady laminar buoyant flow above a line heat source in a fluid of large prandtl number and temperature dependent viscosity. *Int. J. Heat Mass Transfer.* **3**, 55–59.

Szewczyk, A. A. 1962 Stability and transition of the free convection layer along a vertical flat plate. *Int. J. Heat Mass Transfer.* **5**, 903–914.

Wakitani, S. 1985 Non-parallel flow instability of a two dimensional buoyant plume. *J. Fluid Mech.* **159**, 241–258.

Afzal (1980) Puthenveettil & Arakeri (2005) Alam & Arakeri (1993) Batchelor (1954) Brand & Lahey (1967) Bridges & Morris (1984) Brodowicz & Kierkus (1966) Caballina *et al.* (2003) Canuto *et al.* (1988) Fujii (1963) Fujii *et al.* (1973) Gill & Davey (1969) Garg (1981) Gaster (1974) Gebhart (1962) Grossmann & Lohse (2003) Mollendorf & Gebhart (1969) Gebhart *et al.* (1970) Gebhart & Mahajan (1982) Gebhart *et al.* (1988) Halland & Sparrow (1973) Hieber (1974) Hieber & Nash (1975) Kaminski & Jaupart (2003) Kuiken & Rotem (1971) Knowles & Gebhart (1971) Kurdyumov (2005) Ling & Reynolds (1973) Malik (1990) Nayar & Ortega (1993) Natchtsheim (1963) Pera & Gebhart (1971) Riley (1974) Saad (2000) Saric & Nayfeh (1975) Spalding & Cruddace (1961) Niemela & Sreenivasan (2006) Szewczyk (1962) Wakitani (1985)